Abstract

Title of Dissertation:	Accretion onto Black Holes from Large Scales Regulated by Radiative Feedback
	KwangHo Park, Doctor of Philosophy, 2012
Dissertation directed by:	Professor Massimo Ricotti
	Department of Astronomy

This thesis focuses on radiation-regulated gas accretion onto black holes (BHs) from galactic scales emphasizing the role of thermal and radiation pressure in limiting gas supply to the BH. Assuming quasi-spherical symmetry, we explore how the gas accretion depends on free parameters such as radiative efficiency, BH mass, ambient gas density/temperature, and the spectral index of the radiation. Our numerical simulations show an oscillatory behavior of the accretion rate, and thus the luminosity from the BH. We present a model for the feedback loop and provide analytical relationships for the average/maximum accretion rate and the period of the accretion bursts. The thermal structure inside the Strömgren sphere is a key factor for the regulation process, while with increasing ambient gas density and mass of BHs eventually the accretion rate becomes limited by radiation pressure. The period of the luminosity bursts is proportional to the average size of the ionized hot bubble, but we discover that there are two distinct modes of oscillations with very different duty cycles that are governed by different depletion processes of the gas inside the ionized bubble. We also study how angular momentum of the gas affects the accretion process.

In the second part of the thesis, we study the growth rate and luminosity of BHs in motion with respect to their surrounding medium. Contrary to the case

without radiation feedback, we find that the accretion rate increases with increasing BH velocity, v, reaching a maximum value at $v \simeq 20$–30 km s^{-1}, before decreasing as v^{-3}. The increase of the accretion rate with v is produced by the formation of a D-type (density) ionization front (I-front) preceded by a standing bow-shock that reduces the downstream gas velocity to nearly sub-sonic values. Interestingly, there is a range of densities and velocities in which the dense shell downstream of the bow-shock is unstable; its central part is destroyed and reformed intermittingly, producing a periodic accretion rate with peak values about 10 times the mean. This effect can significantly increase the detectability of accreting intermediate mass BHs from the interstellar medium (ISM) in nearby galaxies. We find that the maximum accretion rate for a moving BH is larger than that of a stationary BH of the same mass, accreting from the same medium, if the medium temperature is $T < 10^4$ K. This result could have an important impact on our understanding of the growth of seed BHs in the multi-phase medium of the first galaxies and for building and early X-ray background that may affect the formation of the first galaxies and the reionization process.

Accretion onto Black Holes from Large Scales Regulated by Radiative Feedback

by

KwangHo Park

Dissertation submitted to the Faculty of the Graduate School of the
University of Maryland at College Park in partial fulfillment
of the requirements for the degree of
Doctor of Philosophy
2012

Advisory Committee:

      Professor Massimo Ricotti, Chair
      Professor Christopher Reynolds
      Professor Eve Ostriker
      Professor Richard Mushotzky
      Professor Tiziana Di Matteo (External)
      Professor James Drake (Dean's Representative)

Preface

The content of this thesis is drawn from three papers in a series published or to be soon published in the *Astrophysical Journal*. The main results of Park and Ricotti (2011) and Park & Ricotti (2012a) were presented as an oral dissertation presentation titled *Radiation-regulated Accretion onto Intermediate-Mass Black Holes* at the 219th Winter Meeting of American Astronomical Society in Austin, Texas (2012). Below is the list of the papers, where the first two have been published while the third paper is waiting to be submitted (as of May 30th, 2012) to the same journal.

- Park, K. and Ricotti, M., 2011, *Accretion onto Intermediate-Mass Black Holes Regulated by Radiative Feedback. I. Parametric Study for Spherically Symmetric Accretion*, ApJ, 739, 2.

- Park, K. and Ricotti, M., 2012a, *Accretion onto Black Holes from Large Scales Regulated by Radiative Feedback. II. Growth Rate and Duty Cycle*, ApJ, 747, 9.

- Park, K. and Ricotti, M., 2012b, *Radiation-Regulated Accretion onto Black Holes in Motion. III. Bondi-Hoyle-Lyttleton Accretion with Radiative Feedback*, in preparation.

Chapter 1 and 2 of this thesis are an introduction and numerical methods, respectively relevant for all three papers. Chapter 3 and 4 present the results in Park

and Ricotti (2011) and Park and Ricotti (2012) on accretion onto stationary BHs, while Chapter 5 presents the results for moving BHs in Park and Ricotti (2012b), in preparation. Summary and discussion of the results for all three papers are given in Chapter 6.

To my wife Sue Jean and our mothers

Acknowledgements

I thank God for opening my eyes to the beautiful universe and for guiding me through all these challenging steps.

I can not thank Massimo Ricotti enough for being my academic parent, advisor, friend, and boss for the last six years. I am truly grateful to him for teaching me how to stand, walk, and run as a scholar. I also admit that I benefited from the wonderful members of my thesis committee members. I thank Richard Mushotzky for giving advice and supporting me for the last year of my graduate program and look forward to working on a project which will benefit from this dissertation. I thank Chris Reynolds for his encouraging advice and scientific insight. I feel lucky to have Eve Ostriker in my committee before she leaves for Princeton and I thank her for constructive advice. I thank Tiziana Di Matteo at Carnegie Mellon University for being an external committee member and I look forward to working with her. Special thanks to James Drake from Department of Physics for being willing to serve as Dean's representative for my dissertation.

Contents

List of Figures

Chapter 1

Introduction

The occurrence of gas accretion onto compact gravitating sources is ubiquitous in the universe. The Bondi accretion formula (Bondi 1952), despite the simplifying assumption of spherical symmetry, provides a fundamental tool for understanding the basic physics of the accretion process. Angular momentum of accreted gas, in nearly all realistic cases, leads to the formation of an accretion disk on scales comparable to or possibly much greater than the gravitational radius of the BH, $r_g \sim GM/c^2$, thus breaking the assumption of spherical symmetry in the Bondi solution. However, the fueling of the disk from scales larger than the circularization radius $r_c \sim j^2/GM$, where j is the gas specific angular momentum, can be approximated by a quasi-radial inflow. Thus, assuming that numerical simulations resolve the sonic radius, r_s, the resolved gas flow is quasi-spherical if $r_c \ll r_s$. The Bondi formula, which links the accretion rate to the properties of the environment, such as the gas density and temperature, or Eddington-limited rate are often used in cosmological simulations to model the supply of gas to the accretion disk from galactic scales (Volonteri and Rees 2005; Pelupessy et al. 2007; Di Matteo et al. 2008; Greif et al. 2008; Alvarez et al. 2009; Kim et al. 2011).

However, the Bondi formula is a crude estimation of the rate of gas supply to

the accretion disk because it does not take into account the effect of accretion feedback loops on the surrounding environment. Radiation emitted by BHs originates from gravitational potential energy of inflowing gas (Shapiro 1973) and a substantial amount of work has been performed to understand the simplest case of spherical accretion onto compact X-ray sources or quasars. Several authors have used hydrodynamical simulations to explore how feedback loops operates and whether they produce time-dependent or a steady accretion flows. A variety of feedback processes have been considered: X-ray preheating, gas cooling, photo-heating and radiation pressure (Ostriker et al. 1976; Cowie et al. 1978; Bisnovatyi-Kogan and Blinnikov 1980; Krolik and London 1983; Vitello 1984; Wandel et al. 1984; Milosavljević et al. 2009a; Ostriker et al. 2010; Novak et al. 2011). Typically, the dominance of one process over the others depends on the BH mass and the properties of the gas accreted by the BH. The qualitative description of the problem is simple: gravitational potential energy is converted into other forms of energy such as UV and X-ray photons or jets, which act to reduce and reverse the gas inflow, either by heating the gas or by producing momentum driven outflows (Ciotti and Ostriker 2007; Ciotti et al. 2009; Proga 2007; Proga et al. 2008). In general, these feedback processes reduce the accretion rate and thus the luminosity of the accreting BH (Ostriker et al. 1976; Begelman 1985; Ricotti et al. 2008). Consequently, the time averaged accretion rate differs from Bondi's solution. There have been works on self-regulated accretion of supermassive black holes (SMBHs) at the center of elliptical galaxies (Sazonov et al. 2005; Ciotti and Ostriker 2007; Ciotti et al. 2009; Lusso and Ciotti 2011) and radiation-driven axisymmetric outflow in active galactic nuclei (AGNs; Proga 2007; Proga et al. 2008; Kurosawa et al. 2009; Kurosawa and Proga 2009a,b).

The rate of gravitational inflow onto moving point masses such as BHs or neutron stars has been described analytically in the 40s by Bondi-Hoyle-Lyttleton (Hoyle and

Lyttleton 1939; Bondi and Hoyle 1944). The generalized formula for the accretion onto a point mass moving with velocity v is obtained from the Bondi formula by replacing the gas sound speed with an effective speed $v_{\mathrm{eff}} = (c_{s,\infty}^2 + v^2)^{1/2}$. The accretion rate $\dot{M} \propto \rho v_{\mathrm{eff}} \sigma_{\mathrm{eff}}$ is then calculated as the gas flux through an effective cross section $\sigma_{\mathrm{eff}} = \pi r_{\mathrm{eff}}^2$, where $r_{\mathrm{eff}} = GM/v_{\mathrm{eff}}^2$ is the size of the impact parameter where the effective velocity equals the escape velocity. The formula reduces to the Bondi case for subsonic motions and to the Lyttleton formula for supersonic motions. Despite the similarities between the Bondi and Lyttleton formulae, in the second case the accretion onto the BH is not spherical: the gas streams past the BH and is gravitationally focused on the axis of symmetry of the problem. The component of the gas kinetic energy perpendicular to the BH velocity is converted into thermal energy and dissipated, thus the gas becomes gravitationally bound to the BH and is accreted from the downstream direction. Hence, the generalized Bondi-Hoyle-Lyttleton formula is

$$\dot{M}_{\mathrm{BHL}} = \frac{\dot{M}_{\mathrm{B}}}{(1 + v_\infty^2/c_{s,\infty}^2)^{3/2}}, \tag{1.1}$$

where $\dot{M}_B$ is the Bondi accretion rate for spherically symmetric accretion onto non-moving BHs. The term in the denominator of Equation (1.1) is the only term that accounts for the motion of the point mass.

Two mechanisms summarized above are the main factors which make the accretion deviate from Bondi accretion and both of the processes are expected to reduce the accretion rate far lower than the Bondi accretion rate. However, interesting questions arise when we consider the effect of the two processes together since the modified accretion rate creates a loop of self-regulation. It is well known that Bondi formula fails to describe realistic accretion rates when the effect of radiation emitted by the BH is included. Indeed, the maximum accretion rate that can be achieved under most realistic cases is the Eddington rate. In this limit the outward acceler-

ation on the gas due to Compton scattering of radiation with free electrons equal the gravitational acceleration. The effect of radiation feedback on non-moving BHs has been studied extensively, but to the best of our knowledge the present study is the first to consider radiation feedback effects on moving BHs. This is the main motivation of Chapter 5.

The results of this thesis will help to better understand the accretion luminosities of IMBHs at high z and in the present-day universe (Ricotti 2009). Cosmological simulations show that massive BHs may have formed in metal-free minihalos as Population III star remnants in the early universe (Abel et al. 1998; Bromm et al. 1999; Abel et al. 2000; Madau and Rees 2001; Schneider et al. 2002; Oh and Haiman 2002) or from direct collapse of primordial gas (Carr et al. 1984; Haehnelt et al. 1998; Fryer et al. 2001; Begelman et al. 2006; Volonteri et al. 2008; Omukai et al. 2008; Regan and Haehnelt 2009; Mayer et al. 2010; Johnson et al. 2011). Estimating the accretion luminosity of IMBHs (for a review, see Miller and Colbert 2004; van der Marel 2004) is important to understand their cosmological importance at high z and in the local universe (Mack et al. 2007; Ricotti 2009). Since the luminosity of IMBHs is directly related to their accretion rate, these studies are also relevant for better understanding the mass growth of primordial massive BHs in the early universe (Madau and Rees 2001; Volonteri et al. 2003; Yoo and Miralda-Escudé 2004; Volonteri and Rees 2005; Johnson and Bromm 2007; Pelupessy et al. 2007; Alvarez et al. 2009). For example, different scenarios have been proposed for the formation of quasars at $z \sim 6$ (Fan et al. 2003): growth by mergers, accretion onto IMBHs, or direct formation of larger seed BHs from collapse of quasi-stars (Carr et al. 1984; Haehnelt et al. 1998; Fryer et al. 2001; Begelman et al. 2006; Volonteri et al. 2008; Omukai et al. 2008; Regan and Haehnelt 2009; Mayer et al. 2010) that may form from metal free gas at the center of rare dark matter halos (Oh and

Haiman 2002). Understanding the properties which determine the efficiency of self-regulated accretion onto IMBHs is important to estimate whether primordial BHs produced by Population III stars can accrete fast enough to become SMBHs by redshift $z \sim 6$ (Madau and Rees 2001; Volonteri et al. 2003; Yoo and Miralda-Escudé 2004; Volonteri and Rees 2005; Johnson and Bromm 2007; Pelupessy et al. 2007; Alvarez et al. 2009). Applications of this work also include studies on the origin of ultra-luminous X-ray sources (ULXs) (Krolik et al. 1981; Krolik and Kallman 1984; Ricotti 2007; Mack et al. 2007; Ricotti et al. 2008; Strohmayer and Mushotzky 2009) and the build up of an early X-ray background (Venkatesan et al. 2001; Ricotti and Ostriker 2004; Madau et al. 2004; Ricotti et al. 2005). Recent theoretical (Milosavljević et al. 2009a, hereafter MBCO09) and numerical (Milosavljević et al. 2009b, hereafter MCB09) works explore accretion of protogalactic gas onto IMBHs in the first galaxies. MCB09 describes the accretion onto a 100 M$_\odot$ BH from protogalactic gas of density $n_{\mathrm{H},\infty} = 10^7$ cm^{-3} and temperature $T_\infty = 10^4$ K. Our study, which complements this recent numerical work, is a broader investigation of accretion onto IMBHs for a set of several simulations with a wide range of radiative efficiencies, BH masses, densities and sound speeds of the ambient gas. Our aim is to use simulations to provide a physically motivated description of how radiation modifies the Bondi solution and provide an analytical formulation of the problem (see MBCO09).

This thesis is organized as follows. In Section 1.1 we introduce basic concepts and definitions in the problem. Numerical procedures and physical processes included in the simulations are discussed in Chapter 2. In Chapter 3 ,we focus on simulating accretion onto IMBH regulated by photo-heating feedback in 1D and 2D hydrodynamic simulations, assuming spherically symmetric initial conditions. We provide fitting formulas for the mean and peak accretion rates, and the period between accretion rate bursts as a function of the parameters we explore, including radiative

efficiency, BH mass, gas density, temperature and spectrum of radiation. We lay out a physically motivated model that describes the results of the simulations. In Chapter 4, we relax most of the simplifying assumptions in Chapter 3 and discuss the effects of helium heating/cooling, radiation pressure, and gas angular momentum on the accretion rate. It has been noted that not only electron scattering but also radiation pressure on H I may be important (MBCO09). We explore how the radiation pressure regulates the gas accretion by transferring momentum to the inflowing gas, and whether these physical processes become important compared to the pressure gradients inside the Strömgren sphere. In Chapter 5, we discuss how the motion of BHs relative to surrounding medium affects accretion when regulated by radiative feedback showing the results from axis-symmetric 2D simulations. Finally, summary and discussion are given in Chapter 6.

1.1   Basic Definitions

1.1.1   Bondi Accretion

Accretion of gas from the ISM onto a massive object occurs throughout astrophysics ranging from protostars to BHs. Although the simplifying assumption of spherically symmetric flow is not valid near the compact objects such as close binary systems or AGN it is still a good approximation far from the massive object, and it makes it possible to treat this accretion problem in a fairly exact analytic manner. The spherically symmetric and stationary solution is known as the *Bondi* solution. What can we learn from this classical treatment of spherical accretion? First, we can calculate the steady accretion rate onto BHs, given the ambient conditions (the density ρ_∞ and the temperature T_∞ far from the BH). Second, we can estimate the size of the region of gravitational influence of the object.

In treating the problem mathematically, it is convenient to use a spherical coordinate (r,θ,ϕ) system with origin at the center of the massive object. Physical quantities are independent of angles θ and ϕ by definition of spherical symmetry. For steady flow, the continuity equation is

$$\frac{1}{r^2}\frac{d}{dr}(r^2\rho v) = 0. \tag{1.2}$$

The accretion rate is $\dot{M} = 4\pi r^2\rho(-v) = const(r)$. In the Euler equations, the only external force is gravity, that has only a radial component:

$$\rho\frac{\partial v}{\partial t} + \rho v\nabla v = -\nabla P + f, \tag{1.3}$$

$$\frac{1}{2}v^2 + \frac{\gamma}{\gamma-1}K\rho^{\gamma-1} - \frac{GM}{r} = constant. \tag{1.4}$$

We have assumed a polytropic equation of state $P = K\rho^\gamma$. We have $\gamma = 5/3$ for an adiabatic mono-atomic gas and $\gamma = 1$ for isothermal gas. Since the gas sound speed is $c_s^2 = K\gamma\rho^{\gamma-1} = \gamma P/\rho$ and $v^2 \to 0$ as $r \to \infty$, we obtain the Bernoulli integral:

$$\frac{1}{2}v^2 + \frac{c_s^2}{\gamma-1} - \frac{GM}{r} = \frac{c_{s,\infty}^2}{\gamma-1}, \tag{1.5}$$

where $c_{s,\infty}$ is the sound speed of the gas far away from the BH. The sonic condition relates $c_{s,\infty}$ to $c_s(r_s)$, where r_s is the sonic radius defined as $v^2(r_s) = c_s^2(r_s)$, $GM/r_s = 2c_s^2(r_s)$, and the Bernoulli integral gives

$$c_s^2(r_s)\left[\frac{1}{2} + \frac{1}{\gamma-1} - 2\right] = \frac{c_{s,\infty}^2}{\gamma-1}, \tag{1.6}$$

$$c_s(r_s) = c_{s,\infty}\left(\frac{2}{5-3\gamma}\right)^{\frac{1}{2}}. \tag{1.7}$$

Now the accretion rate $\dot{M}$ can be written as:

$$\dot{M} = 4\pi r^2\rho(-v) = 4\pi r_s^2\rho(r_s)c_s(r_s). \tag{1.8}$$

7

Using $c_s^2 \propto \rho^{\gamma-1}$ we find

$$\rho(r_s) = \rho_\infty \left[\frac{c_s(r_s)}{c_{s,\infty}} \right]^{\frac{2}{\gamma-1}}, \tag{1.9}$$

$$
\begin{aligned}
\dot{M}_B &= \pi G^2 M^2 \frac{\rho_\infty}{c_{s,\infty}^3} \left[\frac{2}{5-3\gamma} \right]^{\frac{5-3\gamma}{2(\gamma-1)}} \\
&= 4\pi \lambda_B \rho_\infty \frac{G^2 M_{bh}^2}{c_{s,\infty}^3} \\
&= 4\pi \lambda_B r_b^2 \rho_\infty c_{s,\infty}, \tag{1.10}
\end{aligned}
$$

where we have introduced the Bondi radius $r_b = GM/c_{s,\infty}^2$ and the dimensionless mass accretion rate λ_B, which depends on the polytropic index, γ, of the gas equation of state $P = K\rho^\gamma$ such as

$$
\begin{aligned}
\lambda_B &= \frac{1}{4} \left[\frac{2}{5-3\gamma} \right]^{\frac{5-3\gamma}{2(\gamma-1)}} \\
&= \frac{\dot{M}_B}{4\pi r_b^2 \rho_\infty c_{s,\infty}}. \tag{1.11}
\end{aligned}
$$

The solution (Bondi 1952) provides the typical length scale r_b at which gravity affects gas dynamics and the typical accretion rate as a function of the BH mass M_{bh}, ambient gas density ρ_∞ and sound speed $c_{s,\infty}$.

1.1.2 Luminosity and Radiative efficiency

A fraction of the gravitational potential energy of the inflowing gas is necessarily converted into radiation or mechanical energy when it approaches the BH, significantly affecting the accretion process. Photons emitted near the BH heat and ionize nearby gas, creating a hot bubble which exerts pressure on the inflowing gas. Radiation pressure may also be important in reducing the rate of gas inflow (see MBCO09). These processes may act as self-regulating mechanisms limiting gas supply to the disk from larger scales and, thus, controlling the luminosity of the BH.

We quantify the reduction of the accretion rate with respect to the case without radiative feedback by defining the dimensionless accretion rate

$$\lambda_{\rm rad} \equiv \frac{\dot{M}}{\dot{M}_B}, \tag{1.12}$$

where $\dot{M}_B$ is the Bondi accretion rate for isothermal gas ($\dot{M}_B = e^{3/2}\pi G^2 M_{\rm bh}^2 \rho_\infty c_{s,\infty}^{-3}$).

The Eddington luminosity sets an upper limit on the luminosity of a BH. In this limit the inward gravitational force on the gas $GM_{\rm bh}m_p r^{-2}$ equals the radiation pressure from photons interacting with electrons via Compton scattering $L\sigma_T(4\pi cr^2)^{-1}$ where σ_T is the Compton scattering cross section. Although this limit can be evaded in some special cases, observations suggest that BH and SMBH luminosity is sub-Eddington. The Eddington luminosity is thus,

$$L_{\rm Edd} = \frac{4\pi GM_{\rm bh}m_p c}{\sigma_T} \simeq 3.3 \times 10^6 L_\odot \left(\frac{M_{\rm bh}}{100~M_\odot}\right). \tag{1.13}$$

The luminosity of an accreting BH is related to the accretion rate via the radiative efficiency η: $L = \eta\dot{M}c^2$. From the Eddington luminosity, we define the Eddington gas accretion rate $\dot{M}_{\rm Edd} \equiv L_{\rm Edd}c^{-2}$, and the dimensionless accretion rate and luminosity as

$$\dot{m} \equiv \frac{\dot{M}}{\dot{M}_{\rm Edd}} \quad \text{and} \quad l \equiv \frac{L}{L_{\rm Edd}}. \tag{1.14}$$

Hence, in dimensionless units, the bolometric luminosity of the BH is $l = \eta\dot{m}$, where $\dot{m}$ is the accretion rate onto the BH. Note, that our definition of $\dot{M}_{\rm Edd}$ is independent of the radiative efficiency η. Therefore, if we impose sub-Eddington luminosity of the BH, the dimensionless accretion rate ranges between $0 < \dot{m} \le \frac{1}{\eta}$. The radiative efficiency, η, depends on the geometry of the accretion disk and on $\dot{m}$. For a thin disk, roughly $\eta \simeq 0.1$, whereas $\eta \propto \dot{m}$ for an advection dominated thick disk or for spherical accretion (Shapiro 1973; Park and Ostriker 2001). In this study we consider two idealized cases for the radiative efficiency. The case of

constant radiative efficiency $\eta = const$; and the case in which the radiative efficiency has a dependence on the dimensionless accretion rate and luminosity: $\eta = const$ for $l \geq 0.1$ and $\eta \propto \dot{m}$ for $l < 0.1$. The second case we explored accounts for the lower radiative efficiency expected when the accreted gas does not settle into a thin disk. In both formulations the the radiative efficiency is one of the free parameter we allow to vary and we do not find important differences between the two cases. Observations of Sgr A*, the best studied case of low accretion rate onto a SMBH, suggest that the radiative efficiency is indeed low but not as low as implied by the scaling $\eta \propto \dot{m}$. Recent theoretical work by (Sharma et al. 2007) demonstrates that there is indeed a floor on the radiative efficiency.

Because the Bondi rate, $\dot{M}_B$ does not include radiation feedback effects, it provides an upper limit on the accretion rate from large scales to radii near the BH. The Eddington rate provides the maximum accretion rate onto the BH, limited by radiation feedback at small radii. Thus, numerical simulations are necessary to obtain realistic estimates of the accretion rates. If the accretion rate onto the BH is lower than the gas accretion from large scales, the accreted material accumulates near the BH, creating a disk whose mass grows with time. We cannot simulate such a scenario because it is too computationally challenging to resolve a range of scales from the Bondi radius to the accretion disk in the same simulations. Here we assume that accretion onto the BH is not limited by physical processes taking place on radial distances much smaller than the sonic radius. For instance, even if angular momentum of accreted gas is small and the circularization radius $r_c \ll r_s$, further inflow will be slowed down with respect to the free-fall rate. The rate of inflow will be controlled by angular momentum loss (e.g. torques due to MHD turbulence) and there will be a delay between the accretion rate at the inner boundary of our simulation ($r_{\min}$) and the accretion luminosity associated with it. The effect of the

aforementioned time delay on the feedback loop is considered in Chapter 4. We also assume that the effect of self-gravity is negligible (see Li 2011) in our simulations since we have estimate that the mass within the H $\textsc{ii}$ region around the BH is smaller than the BH mass for $M_{\mathrm{bh}} < 1000 \ \mathrm{M}_{\odot}$.

If the rate of gas supply to the disk is given by the Bondi rate, accretion onto the BH is sub-Eddington for BH masses

$$M_{\mathrm{bh}} < \frac{c_{s,\infty}^3}{G n_{\mathrm{H},\infty} \sigma_T c \eta} \sim 40 M_{\odot} \ T_{\infty,4}^{1.5} n_{\mathrm{H},5}^{-1} \eta_{-1}^{-1}, \tag{1.15}$$

where we use the notations of $T_{\infty,4} \equiv T_{\infty}/(10^4 \ \mathrm{K})$, $n_{\mathrm{H},5} \equiv n_{\mathrm{H},\infty}/(10^5 \ \mathrm{cm}^{-3})$ and $\eta_{-1} \equiv \eta/10^{-1}$. Thus, in this regime we may assume that the accretion is quasi-steady in the sense that the mean accretion rate onto the BH equals the gas supply from large scales when the accretion rate is averaged over a sufficiently long time scale.

Chapter 2

Numerical Simulations

2.1 ZEUS-MP and Radiative Transfer Module

We perform a set of hydrodynamic simulations to understand accretion onto IMBHs regulated by radiation feedback. Numerical simulations of radiative feedback by BHs are challenging because they involve resolving a large dynamical range in length scales. In this study we use ZEUS-MP (Hayes et al. 2006), a modified parallel version of the non-relativistic hydrodynamics code ZEUS (Stone and Norman 1992). For the present work we add a radiative transfer module (Ricotti et al. 2001) to ZEUS-MP to simulate radiative transfer of UV and X-ray ionizing photons emitted near the BH. A detailed description of the numerical methods used to solve radiative transfer and tests of the code are presented in the Appendix B.

As X-ray and UV photons ionize the surrounding medium, different reactions take place depending on the density and composition of the gas. Photo-ionization changes the ionization fraction of H and He. The detailed evolution of the Strömgren sphere depends on the cooling function $\Lambda(T, Z)$ of the gas and thus on the metallicity, Z, and the fraction of gas in the molecular phase. For a gas of primordial composition, the cooling rate depends on the formation rates of H^- and H_2, which

depend on both the redshift and the intensity of the local dissociating background in the H_2 Lyman-Werner bands (e.g. Shapiro and Kang 1987; Abel et al. 1998; Ricotti et al. 2002a,b). In addition, the cooling function may depend on redshift due to Compton cooling of the electrons by CMB photons. In Chapter 3 we adopt atomic hydrogen cooling for temperatures $T > 10^4$ K, and use a simple parametric function to model complicated cooling physics of gas at $T < 10^4$ K. Thus, the temperature structure inside the ionized bubble is appropriate only for a low metallicity gas. In Chapter 4 we also include the effect of helium photo-heating and cooling. We assume that gas cooling at temperatures below T_∞ is negligible in order to achieve thermal equilibrium in the initial conditions far from the BH. For the parameter space in which we can neglect the effect of radiation pressure we find (see Chapter 3) that the accretion rate is a function of the temperature both outside and inside the H II region. The temperature outside the H II region depends on the cooling function of gas at $T < 10^4$ K and on the heating sources. The temperature inside the H II region depends on the spectrum of radiation and cooling mechanism of gas at $T > 10^4$ K. Thus, it depends on the gas metallicity and the redshift at which Compton cooling might become important. However, for the parameter space we have explored we find that Compton cooling has a minor effect on the temperature inside and outside the Strömgren sphere.

The gas heating rate depends on flux and spectral energy distribution (SED) of the radiation emitted near the BH. We assume a luminosity of the BH $l = \eta \dot{m}$, where $\dot{m}$ is calculated at the inner boundary in our simulation (typically $r_{\min} \sim 10^{-5}$ pc). We adopt a single power law $\nu^{-\alpha}$ for the SED, where the spectral index α is one of the parameters we vary in our set of simulations.

We use an operator-split method to calculate the hydrodynamic step and the radiative transfer and chemistry steps. The hydrodynamic calculation is done using

ZEUS-MP, then for the radiative transfer calculation we use a ray tracing module (Ricotti et al. 2001). The radiative transfer module calculates chemistry, cooling and heating processes along rays outgoing from the central BH, and thus is easily parallelized in the polar angle direction.

We perform 1D and 2D simulations in spherical coordinates. In both cases we use a logarithmically spaced grid in the radial direction typically with 256 to 512 cells to achieve high resolution near the BH. The size ratio between consecutive grids is chosen according to the free parameters of the simulation to resolve the ionization front and resolve the region where the gas is in free fall. In the 2D simulations we use evenly spaced grids in the polar angle direction and compute radiative transfer solutions in each direction. Flow-out inner boundary conditions and flow-in outer boundary conditions are used in the radial direction (r), whereas in polar angle directions (θ), reflective boundary conditions are used.

To determine the optimal box size of the simulations we make sure that we resolve important length scales in the problem: the inner Bondi radius, $r_{b,in}$, the outer Bondi radius, r_b, the sonic radius, r_s and the ionization front, R_s. We find that the average size of the Strömgren sphere $\langle R_s \rangle$ is larger than the outer Bondi radius r_b in our simulations. The opposite case when $\langle R_s \rangle$ is located within r_b might be astrophysically important, however it is beyond the range of the current study. We select the value of the inner boundary (typically $\sim 10^{-5}$ pc for $M_{bh} = 100$ M$_\odot$) to be smaller than the sonic point or the inner Bondi radius (both still far larger than the Schwarzschild radius of the BHs). We find that once the sonic radius is resolved, reducing the inner boundary box size does not create significant differences in the results. In most cases the ionization front is located outside of the outer Bondi radius and the box size is selected to be large enough to cover both length scales. We select a box size that achieves the highest possible resolution with a given number of grids,

making sure that the physical quantities around boundaries remain constant during the simulations. The box is sufficiently large to minimize the effect of spurious wave reflections at the outer boundary.

In Chapter 3 and 4, we adopt idealized initial conditions of uniform density and temperature, zero velocity and zero angular momentum of the gas relative to the BH. We also consider the effect of a time-delay between the accretion rate at the inner boundary of our simulations and the accretion luminosity in Chapter 4. In Chapter 5, we relax some of these assumptions by considering the effect of BH motion with respect to the ambient medium. We assume monatomic, non-relativistic ideal gas with $\gamma = 5/3$ which is initially neutral (electron fraction $x_e \sim 10^{-5}$).

In Chapter 3, we also neglect the effect of radiation pressure. Our goal is to add to the simulations one physical process at a time to understand which feedback loop is dominant in a given subset of the parameter space. We take this approach to attempt an interpretation of the simulation results in the context of a physically motivated analytical description of the accretion cycle. We explore the effect of radiation pressure due to H I ionization and Lyman-alpha scattering in Chapter 4. However, a simple inspection of the relevant equations suggests that radiation pressure is increasingly important for large values of the ambient gas density ($n_{\mathrm{H},\infty} \sim 10^7 \ \mathrm{cm}^{-3}$, see MBCO09) since accretion rate approaches Eddington limit.

2.2   Radiation Pressure and Time Delay

In Chapter 4, we include the effects of helium heating/cooling in addition to hydrogen. Therefore, we simulate photo-ionization, photo-heating and cooling for six species H I, H II, He I, He II, He III, and e^-.

We also calculate the radiation pressures both on e^- and H I to interpret the effect

of momentum transfer to the inflowing gas by the ionizing photons. The magnitude of acceleration at a given radius due to radiation pressure depends on the luminosity, the ionization fraction of hydrogen and helium, and the cross section of the species to photon-ionization. The specific flux $F_\nu \propto e^{-\tau}/r^2$ at a given radius (r), assuming a power-law spectrum with a spectral index α, depends on the optical depth τ_ν, and the cross section σ_ν. Thus, the accelerations due to momentum transfer to H I and e^- can be written as

$$a_{\rm rad,H\ I} = \frac{x_{\rm H\ I}}{m_p c} \int \sigma_{\rm H\ I,\nu} F_\nu d\nu, \tag{2.1}$$

$$a_{\rm rad,e^-} = \frac{x_{e^-}}{m_p c} \int \sigma_T F_\nu d\nu, \tag{2.2}$$

where $x_{\rm H\ I}$ and x_{e^-} are H I and e^- fractions, respectively, σ_T is the Thomson cross section, and m_p is the proton mass. The radial component of the acceleration at a given radius is updated as $\mathbf{a} = \mathbf{a}_{\rm grav} + \mathbf{a}_{\rm rad}$, where $\mathbf{a}_{\rm rad} = \mathbf{a}_{\rm rad,H\ I} + \mathbf{a}_{\rm rad,e^-}$.

In Section 4.3, we study the effect of non-zero angular momentum of gas which leads to a time delay between the accretion rate at the sonic radius and the luminosity output, due to the formation of an accretion disk. In order to estimate realistic values of the time delay we assume that the gas conserves angular momentum and settles into an accretion disk of radius $R_{\rm disk}$. We then assume an alpha model for the thin disk to estimate the timescale for the gas to lose angular momentum and fall into the BH.

Numerically, it is convenient to express the time delay in units of the free-fall timescale $t_{\rm ff}$ calculated at the simulation's inner boundary. The free-fall timescale we have defined can be very large compared to $t_{\rm ff}$ calculated at the radius of the accretion disk near the BH (at tens of gravitational radii $R_{\rm Sch} \equiv 2GM_{\rm bh}/c^2$). Approximately, the gas is accreted at the viscous timescale $t_{\rm visc}$, that compared to $t_{\rm ff}$

is

$$t_{\text{visc}}(R_{\text{disk}})/t_{\text{ff}}(R_{\text{disk}}) \sim \alpha_{\text{disk}}^{-1}\mathcal{M}^2 \sim \alpha_{\text{disk}}^{-1}c_{\text{s,disk}}^{-2}GM_{\text{bh}}R_{\text{disk}}^{-1} \sim 0.5 \; \alpha_{\text{disk}}^{-1}(c/c_{\text{s,disk}})^2\mathcal{R}_{\text{disk}}^{-1},$$

(2.3)

where α_{disk} is the dimensionless viscosity parameter for a thin disk (Shakura and Sunyaev 1973), $c_{\text{s,disk}}$ is the sound speed of the gas in the disk, and we define $\mathcal{R}_{\text{disk}} \equiv R_{\text{disk}}/R_{\text{Sch}}$. The dependence of the free-fall time on radius is $t_{\text{ff}} \propto R^{1.5}$, while the viscous timescales as $t_{\text{visc}} \propto R^{-1}t_{\text{ff}} \propto R^{0.5}$ assuming constant sound speed due to effective cooling (note that since we are considering a gas of zero or very low metallicity, the gas in the disk will not easily cool to temperature below 10^4 K if the gas is atomic). Thus, the infall time at the disk radius R_{disk} is

$$\frac{t_{\text{visc}}(R_{\text{disk}})}{t_{\text{ff}}(r_{\text{min}})} \sim \frac{0.5}{\alpha_{\text{disk}}}\frac{v_{\text{min}}^3}{c\,c_{\text{s,disk}}^2}\mathcal{R}_{\text{disk}}^{1/2} \sim \frac{0.3}{\alpha_{\text{disk}}}\left(\frac{T_{\text{disk}}}{10^4 \text{ K}}\right)^{-1}\mathcal{R}_{\text{disk}}^{1/2}.$$

(2.4)

To estimate the parameters in Equation (2.4) we have defined $v_{\text{min}} \equiv (GM_{\text{bh}}/r_{\text{min}})^{1/2} \simeq 260$ km s^{-1}. Assuming $\alpha_{\text{disk}} \sim 0.01$–$0.1$, $T_{\text{disk}} \sim 10^4$ K, and $\mathcal{R}_{\text{disk}} \lesssim 10^2$–$10^4$, we find time delays of $\lesssim 300$ free-fall times at r_{min}, that is the parameter space we explore in Section 4.3.

In our code, the accretion rates calculated at the inner boundary of the simulations are stored in an assigned array about 1000 steps for each t_{ff}. Stored accretion rates with a given time delay are then read from the array and used to estimate the luminosity at the current moment.

2.3 Axis-symmetric Accretion

In Chapter 5, axis-symmetric geometry with respect to the azimuthatal angle (ϕ) is applied to all simulations. We use logarithmically spaced grid in the radial direction (r) and evenly spaced grid in the polar angle direction ($0 \leq \theta \leq \pi$) with BHs

centered at the origin $r = 0$. Axis-symmetric configuration is necessary to simulate BHs in motion relative to ambient gas which is assumed to be moving parallel to the polar axes. We apply flow-in boundary conditions of the boundary in the outer radial direction for the first half of the polar angle $(0 \le \theta \le 0.5\pi)$ and flow-out boundary conditions for the second half $(0.5\pi < \theta \le \pi)$. At the inner boundary in the radial direction we apply flow-out boundary condition for the entire polar angle. Reflective boundary conditions are applied along the the polar axis $\theta = 0$ and $\theta = \pi$ to satisfy the axis-symmetric configuration.

We assume uniform density and constant velocity for the initial conditions. For the supersonic cases $(\mathcal{M} > 1)$, we start the simulations with an assumption of fixed accretion rate $(\langle \lambda_{\rm rad} \rangle = 0.001)$ to reduce the effect of oscillation observed at early phases of the simulations. For our reference simulations we select typical parameters of radiative efficiency $\eta = 0.1$ from thin disk model (Shakura and Sunyaev 1973), BH mass $M_{\rm bh} = 100\ M_\odot$, and the temperature of the ambient gas $T_\infty = 10^4$ K. We explore a range of Mach numbers up to $\mathcal{M} = 10$, and gas densities $n_{\rm H,\infty} = 10^2$–10^6 cm^{-3}.

Chapter 3

Spherically Symmetric Accretion

Abstract: This chapter focuses on the effect of radiative feedback on accretion onto IMBHs using the hydrodynamical code ZEUS-MP with a radiative transfer algorithm. In this chapter, we assume accretion from a uniformly dense gas with zero angular momentum and extremely low metallicity. Our 1D and 2D simulations explore how X-ray and UV radiation emitted near the BH regulates the gas supply from large scales. Both 1D and 2D simulations show similar accretion rate and period between peaks in accretion, meaning that the hydro-instabilities that develop in 2D simulations do not affect the mean flow properties. We present a suite of simulations exploring accretion across a large parameter space, including different radiative efficiencies and radiation spectra, BH masses, density and temperature, T_∞, of the neighboring gas. In agreement with previous studies we find regular oscillatory behavior of the accretion rate, with duty cycle $\sim 6\%$, mean accretion rate 3% $(T_\infty/10^4 \text{ K})^{5/2}$ of the Bondi rate and peak accretion ~ 10 times the mean for T_∞ ranging between 3000 K and 15000 K. We derive parametric formulas for the period between bursts, the mean accretion rate and the peak luminosity of the bursts and thus provide a formulation of how feedback regulated accretion operates. The temperature profile of the hot ionized gas is crucial in determining the accretion

rate, while the period of the bursts is proportional to the mean size of the Strömgren sphere and we find qualitatively different modes of accretion in the high vs. low density regimes. We also find that softer spectrum of radiation produces higher mean accretion rate. However, it is still unclear what is the effect of a significant time delay between the accretion rate at our inner boundary and the output luminosity. Such a delay is expected in realistic cases with non-zero angular momentum and may affect the time-dependent phenomenology presented here. This study is a first step to model the growth of seed BHs in the early universe and to make a prediction of the number and the luminosity of ultra-luminous X-ray sources in galaxies produced by IMBHs accreting from the interstellar medium.

3.1 Qualitative description of accretion regulated by radiative feedback

Our simulations show that UV and X-ray photons modify the thermal and dynamical structure of the gas in the vicinity of the Bondi radius. A hot bubble of gas is formed due to photo-heating by high energy photons and sharp changes of physical properties such as density, temperature, and ionization fraction occur at the ionization front. Figure 3.1 shows 8 snapshots from one of our 2D simulations. Top half of each snapshot shows the gas density and the bottom half shows the hydrogen ionization fraction. We show the periodic oscillation of the density and the ionization fraction from a 2D simulation in Figure 3.1. The time evolution of the radial profiles of density, temperature, ionization fraction and accretion rate for the 1D simulation are shown in Figure 3.2. We can identify 3 evolutionary phases that repeat cyclically:

1. Once the Strömgren sphere is formed, it expands and the gas density inside
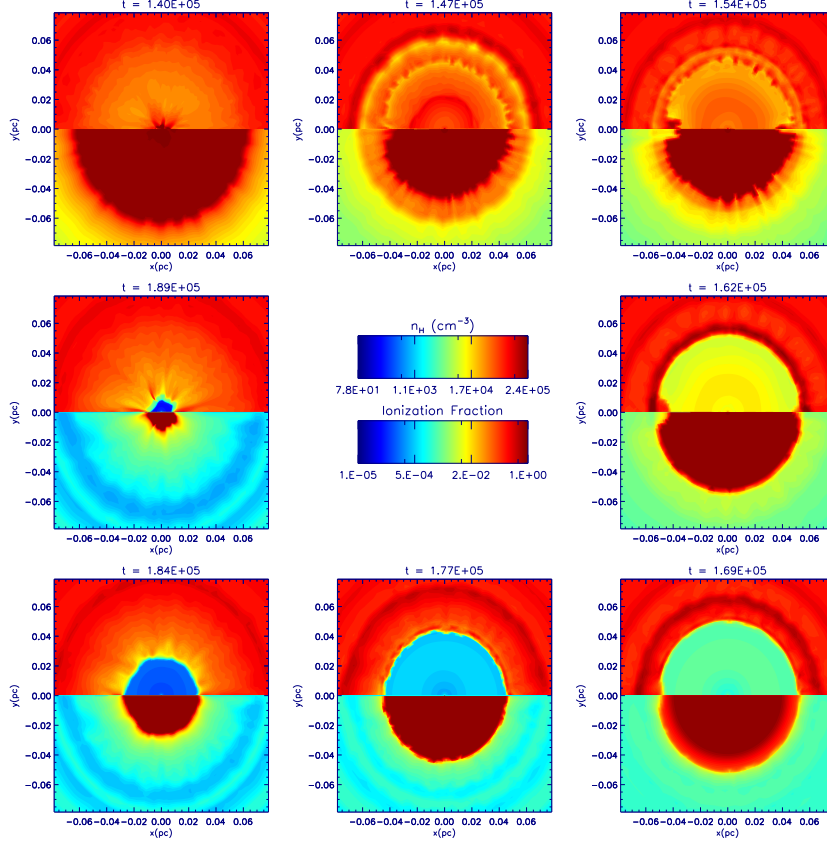
Figure 3.1: Evolution of the gas density and ionization fraction in a simulation of an accreting BH of mass $M_{\rm bh} = 100$ M$_\odot$, gas density $n_{\rm H,\infty} = 10^5$ cm^{-3}, and temperature $T_\infty = 10^4$ K. In each panel the top halves show the density (number of hydrogen atoms per cm^3) and the bottom halves show the ionization fraction, $x_e = n_e/n_H$, of the gas. The evolutionary sequences are shown in a clockwise direction. *Top panels from left to right*: A Strömgren sphere forms fueled by ionizing photons as the BH accretes gas. The higher pressure inside the Strömgren sphere stops the gas inflow while the BH at the center consumes the hot gas inside the ionization front. Inflowing gas accumulates in a dense shell outside the hot bubble while exponential decay of the accretion rate occurs due to decreasing density inside the hot bubble as gas depletion continues. Although the number of emitted ionizing photons decreases, the ionized sphere maintains its size because of the decrease in density inside the hot bubble. *Bottom panels from right to left*: The density of hot gas inside the Strömgren sphere keeps decreasing until pressure equilibrium across the front can no longer be maintained. *Middle left*: The dense shell in front of the Strömgren sphere collapses onto the BH and this leads to a burst of accretion luminosity. *Top left*: The Strömgren sphere reaches its maximum size and the simulation cycle repeats.

that hot bubble decreases maintaining roughly pressure equilibrium across the ionization front. At the front, gas inflow is stopped by the hot gas and the average gas density inside the bubble decreases due to the following two physical processes. First, the BH continues accreting hot gas within an accretion radius, r_{acc}, defined as the radius where the gravitational force of the BH dominates the thermal energy of the hot gas. The accretion radius is similar to the Bondi radius defined by the temperature inside Strömgren sphere, but there exists a difference between them since the kinematic and thermal structure of gas is modified significantly by the photo-heating and cooling. Second, the gas between r_{acc} and the ionization front moves towards the ionization front due to pressure gradients. Figure 3.3 shows inflowing gas within r_{acc} and outflowing gas outside r_{acc}. A dense shell forms just outside the ionization front. Thus, the mass of the shell grows because gravity pulls distant gas into the system at the same time that gas within the the hot bubble is pushed outwards.

2. As the average density inside the hot bubble decreases, the accretion rate diminishes. During this process the radius of the Strömgren sphere remains approximately constant since the reduced number of ionizing UV and X-ray photons is still sufficient to ionize the rarefied hot bubble. Figure 3.6 illustrates this. Thus, the average gas temperature, ionization fraction and the size of the H II region remain constant. As the accretion rate increases during the burst, it produces a rapid expansion of the Strömgren sphere radius. During one cycle of oscillation, there are small peaks in the Strömgren sphere radius which are associated with minor increases in the accretion rate. Rayleigh-Taylor (RT) instabilities develop quickly when the accretion rate increases. In these phases, the acceleration of the dense shell is directed toward the BH, so the dense shell, supported by more rarefied gas, becomes RT unstable.
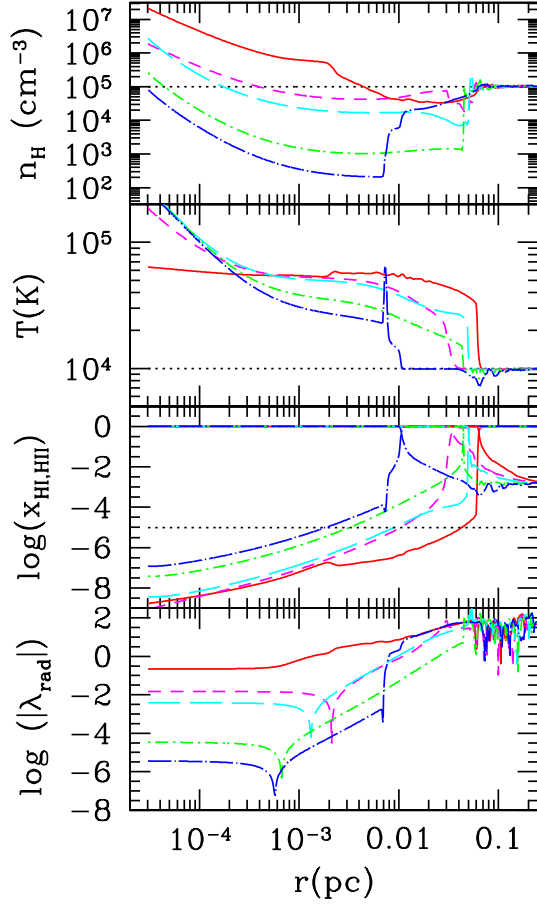
Figure 3.2: *Top to bottom* : Radial profiles of density, temperature, neutral/ionization fractions and accretion rate in 1D simulation for η=0.1, $M_{\rm bh}$=100 M$_\odot$, $n_{\rm H,\infty} = 10^5$ cm^{-3} and T_∞=10^4 K. Different lines indicates profiles at different times: t=0.0 (dotted), t=1.13×10^4 (solid), t=1.28×10^4 (short dashed), t=1.43×10^4 (long dashed), t=1.58×10^4 (dot-short dashed), t=1.71×10^4 yr (dot-long dashed). *Solid lines* : at the maximum expansion of the Strömgren sphere. *Dot-long dashed lines* : at the collapsing phase of dense shell. Physical properties inside the Strömgren sphere change as a function of time. The number density and temperature of hydrogen decrease with time after the burst. The neutral fraction increases as a function of time from the burst. The accretion rate as a function of radius is constant within accretion radius $r_{\rm acc}$ (see Section 3.5). Accretion rate in the outer parts is larger than the Bondi rate since our simulations start from contant density and zero velocity which make the gas fall to the BH freely until the accretion rate in the outer parts reach a steady state. The excess of gas supply is regulated outside the I-front making velocity positive and negative in this range of radii.
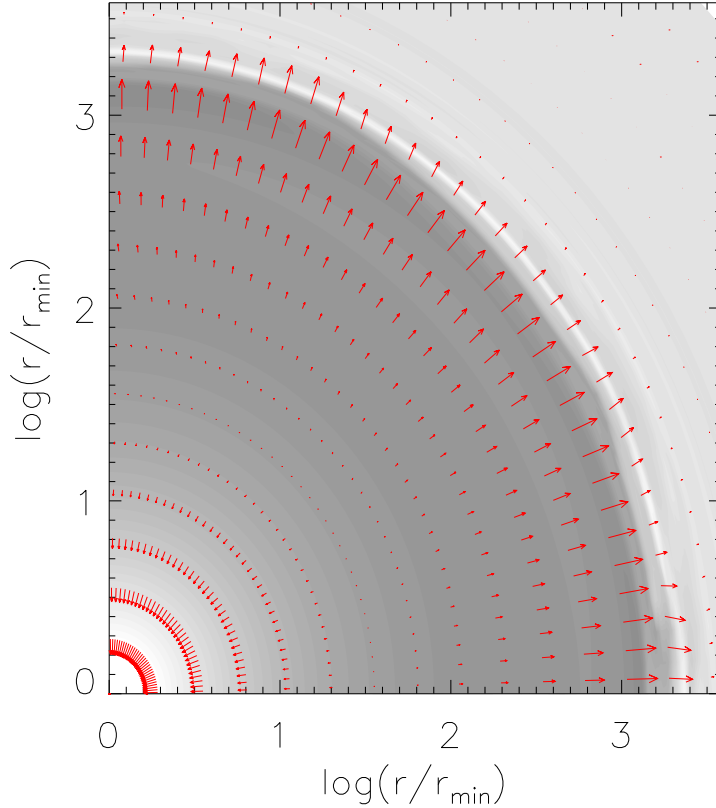
Figure 3.3: Gas density and velocity field for the simulation with $\eta = 0.1$, $M_{\rm bh} = 100\,{\rm M}_\odot$, $n_{\rm H,\infty} = 10^5\,{\rm cm}^{-3}$, and $T_\infty = 10^4\,{\rm K}$. When a Strömgren sphere is formed, gas inside the hot bubble is depleted by accretion onto the BH and the outflow toward the dense shell due to pressure gradient.

3. As gas depletion continues, the pressure inside the hot bubble decreases to the point where equilibrium at the ionization front breaks down. The outward pressure exerted by the hot bubble becomes too weak to support the gravitational force exerted on the dense shell. The dense shell of gas collapses toward the BH (see Figure 3.4), increasing dramatically the accretion rate and creating a burst of ionizing photons. The ionization front propagates outward in a spherically symmetric manner, creating a large Strömgren sphere and returning to the state where the high pressure inside the Strömgren sphere suppresses gas inflow from outside.
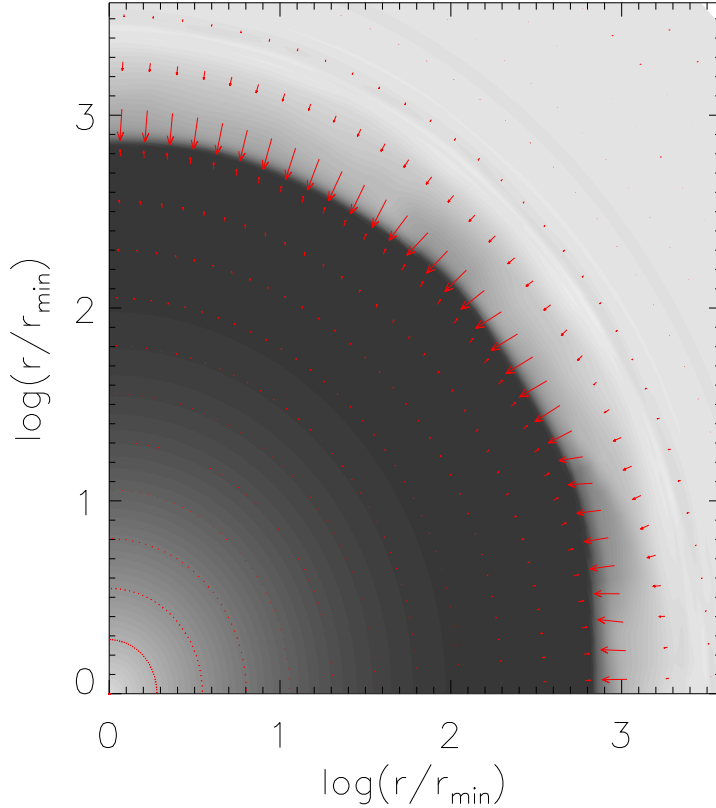
Figure 3.4: Gas density and velocity field for the simulation with $\eta = 0.1$, $M_{\rm bh} = 100~{\rm M}_\odot$, $n_{\rm H,\infty} = 10^5~{\rm cm}^{-3}$, and $T_\infty = 10^4~{\rm K}$. Gas depletion inside the Strömgren sphere leads to the collapse of the dense shell, creating a burst of accretion.

3.2   Comparison of 1D and 2D simulations

In agreement with previous studies, our simulations show that radiation feedback induces regular oscillations of the accretion rate onto IMBH. This result is in good agreement with numerical work by MCB09 for accretion onto a 100 ${\rm M}_\odot$ BH from a high density ($n_{\rm H,\infty} = 10^7~{\rm cm}^{-3}$) and high temperature ($T_\infty = 10^4~{\rm K}$) gas. Periodic oscillatory behavior is found in all our simulations for different combinations of parameters, when assuming spherically symmetric initial conditions and a stationary BH. This oscillation pattern is quite regular and no sign of damping is observed for

at least ~ 10 cycles.

For the same parameters, our 1D and 2D simulations are nearly identical in terms of oscillatory behavior in accretion rate and Strömgren sphere size. Figure 3.5 shows accretion rate in 1D and 2D simulations for $M_{\rm bh}$=100 M$_\odot$, $T_\infty = 10^4$ K and $n_{\rm H,\infty} = 10^5$ cm^{-3}. Note the similar pattern in accretion rate and period between bursts. This indicates that the 1D result adequately represents 2D cases when the accretion flow does not have significant angular momentum.

Moreover, this result demonstrates that RT instabilities which we observe in the 2D simulations do not affect the mean accretion rate or the period of oscillations. The RT instability develops during the phase when the dense shell in front of the ionization front is supported against gravitational accretion by the low density medium inside the hot bubble (Whalen and Norman 2008b,a). The top panels in Figure 3.1 show small instabilities when ionization fronts move outward, which largely decay over time. The pressure gradient inside the Strömgren sphere creates an outward force which helps suppress the development of the instability.

In summary, we argue that 1D simulations can be used in place of higher dimension simulations to determine the cycle and magnitude of the periodic burst of gas accretion onto IMBH. This allows us to reduce the computational time required to explore a large range of parameter space.

3.3 Parameter space exploration

In this section we present the results of a set of 1D simulations aimed at exploring the dependence of the accretion rate and the period of oscillations of the BH luminosity as a function of the BH mass, $M_{\rm bh}$, the ambient gas density, $n_{\rm H,\infty}$, temperature, T_∞, and the radiative efficiency η. In § 5 we present results in which we allow the
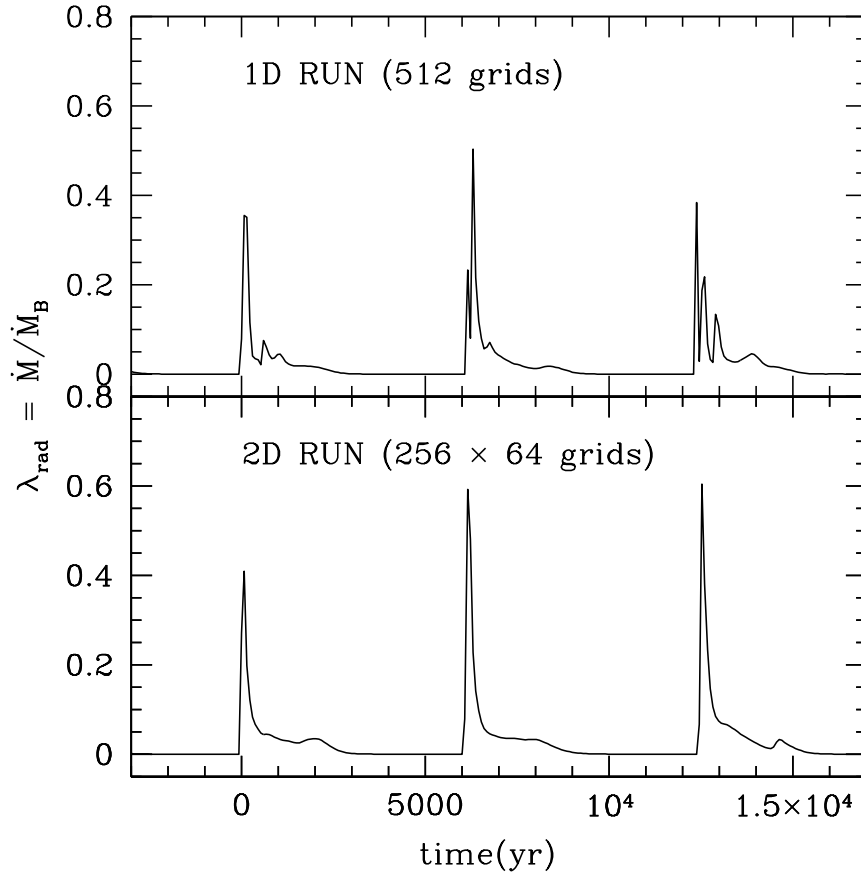
Figure 3.5: Accretion rates as a function of time in 1D and 2D simulations with $\eta = 0.1$, $M_{\rm bh} = 100$ M$_\odot$, $n_{\rm H,\infty} = 10^5$ cm^{-3} and $T_\infty = 10^4$ K. Both results show similar oscillation patterns with the same period and average accretion rate.

spectrum of ionizing radiation to vary as well. The accretion can be described by three main parameters: $\tau_{\rm cycle}$, the mean period between bursts, $\lambda_{\rm rad,max}$, the maximum value of the dimensionless accretion rate (at the peak of the burst), and $\langle \lambda_{\rm rad} \rangle$, the time-averaged dimensionless accretion rate. These parameters are typically calculated as the mean over ~ 5 oscillation cycles and the error bars represent the standard deviation of the measurements.

After reaching the peak, the luminosity decreases nearly exponentially on a time scale $\tau_{\rm on}$, that we identify as the duration of the burst. Both $\tau_{\rm on}$ and the duty cycle, $f_{\rm duty}$, of the black hole activity (*i.e.*, the fraction of time the BH is active), can be

27
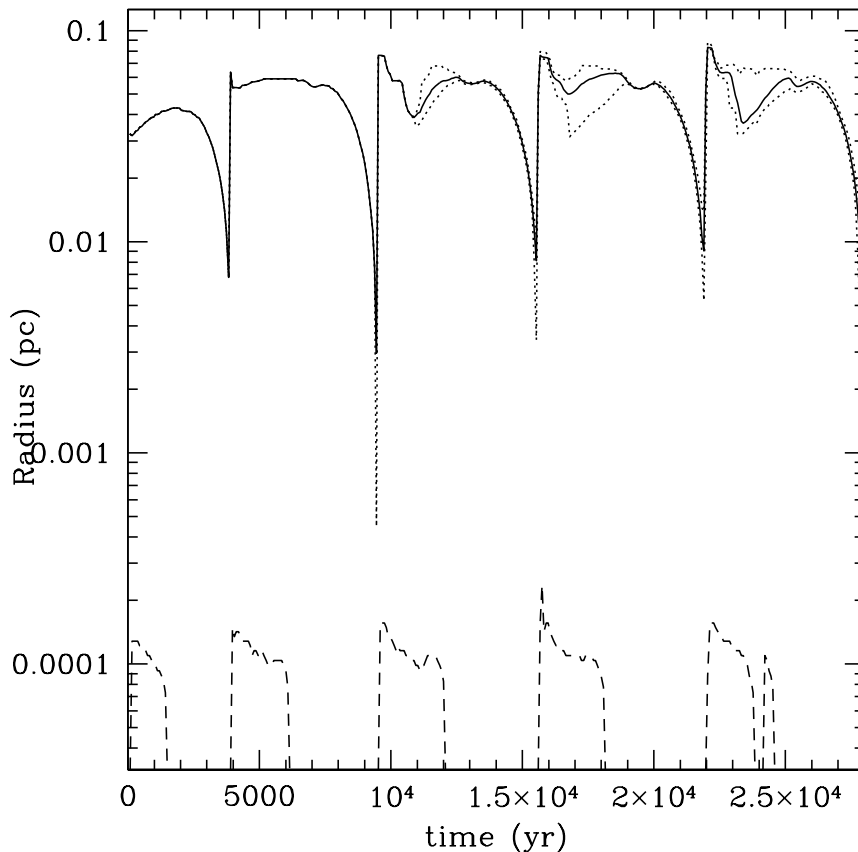
Figure 3.6: Evolution of Strömgren radius and sonic point with time for 2D simulation with $\eta = 0.1$, $M_{\rm bh} = 100$ $M_{\odot}$, $n_{\rm H,\infty} = 10^5$ cm^{-3} and $T_\infty = 10^4$ K. The solid line shows the mean size of the Strömgren radius and dotted lines show the minimum and maximum Strömgren radii. It shows the same period of oscillation seen in accretion rate as a function of time. In general, the Strömgren radius is proportional to the accretion rate which determines the number of ionizing photons. When the accretion rate is maximum, the size of the Strömgren sphere also has its maximum size. The dashed line shows the evolution of the sonic radius.

expressed as a function of $\tau_{\rm cycle}$, $\lambda_{\rm rad,max}$ and $\langle \lambda_{\rm rad} \rangle$:

$$\tau_{\rm on} \equiv \frac{\langle \lambda_{\rm rad} \rangle}{\lambda_{\rm rad,max}} \tau_{\rm cycle}, \tag{3.1}$$

$$f_{\rm duty} \equiv \frac{\tau_{\rm on}}{\tau_{\rm cycle}} = \frac{\langle \lambda_{\rm rad} \rangle}{\lambda_{\rm rad,max}}. \tag{3.2}$$

The values of $\lambda_{\rm rad,max}$ and $f_{\rm duty}$ as a function of the BH mass, the density and the

temperature of the ambient medium are important for estimating the possibility of

detection of IMBHs in the local universe because these values provide an estimate of the maximum luminosity and the number of active sources in the local universe at any time. On the other hand, the mean accretion rate, $\langle\lambda_{\mathrm{rad}}\rangle$ is of critical importance for estimating IMBH growth rate in the early universe.

The four panels in Figure 3.8 summarize the results of a set of simulations in which we vary the free parameters one at a time. We find that, in most of the parameter space that we have explored, the period of the oscillations and the accretion rates are described by a single or a split power law with slope β. In the following paragraphs we report the values of β derived from weighted least squares fitting of the simulation results. The weight is $1/\sigma$ where σ is the standard deviation of $\langle\lambda_{\mathrm{rad}}\rangle$ or $\lambda_{\mathrm{rad,max}}$ over several oscillations.

a) Dependence on the radiative efficiency

First, we explore how the accretion depends on the radiative efficiency η. This parameter describes the fraction, η, of the accreting rest mass energy converted into radiation while the remaining fraction, $1 - \eta$, is added to the BH mass. We have explored both constant values of the radiative efficiency and the case $\eta \propto \dot{m}$ for $l < 0.1$ (see Section 1.1.2). The simulation results shown in this section are obtained assuming η is constant. We find similar results for $\langle\lambda_{\mathrm{rad}}\rangle$, $\lambda_{\mathrm{rad,max}}$ and τ_{cycle} when we assume $\eta \propto \dot{m}$. The radiative efficiency for a thin disk is about 10%. Here, we vary η in the range: 0.2% to 10%. The other free parameters are kept constant with values $n_{\mathrm{H},\infty} = 10^5$ cm^{-3}, $M_{\mathrm{bh}} = 100$ M$_\odot$ and $T_\infty = 10^4$ K. Figure 3.7 shows the accretion rate as a function of time for different values of the radiative efficiency: $\eta = 0.1, 0.03, 0.01$ and 0.003. Panel (a) in Figure 3.8 shows the dependence on η of the three parameters that characterize the accretion cycle. The maximum accretion rate increases mildly with increasing η (log slope $\beta = 0.13 \pm 0.06$). The
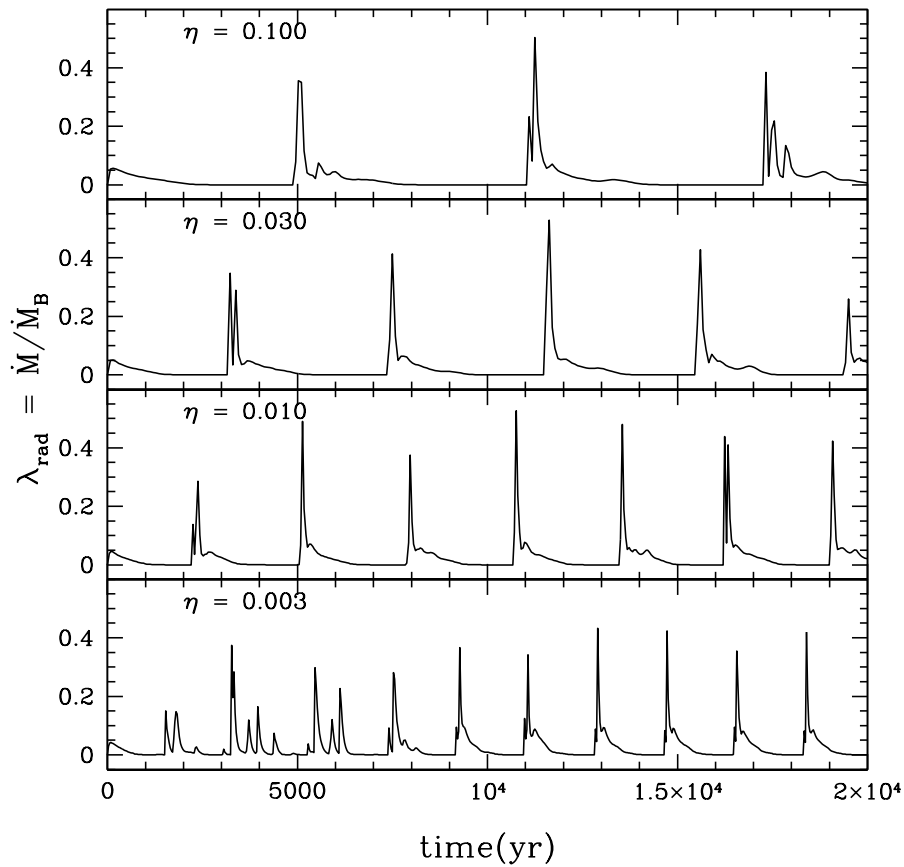
Figure 3.7: Dependence of accretion rate and period of oscillations on the radiative efficiency η. From top to bottom the evolution of accretion rate is shown for $\eta = 0.1, 0.03, 0.01$ and 0.003. The peak accretion rate does not change much with η, but intervals between oscillations decrease with decreasing η.

average accretion rate is $\langle \lambda_{\rm rad} \rangle \sim 2.9\% \pm 0.2\%$, is nearly independent of η ($\beta = -0.04 \pm 0.01$). The period of the oscillations increases with η as $\tau_{\rm cycle} \propto \eta^{1/3}$. We also show the simulation results including helium photo-heating and cooling, shown as open symbols in the same panel of Figure 3.8. We find that including helium does not change the qualitative description of the results, but does offset the mean accretion rate, that is $\sim 41\%$ lower and the period of the accretion bursts, that is $\sim 42\%$ shorter. This offset of the accretion rate and period with respect to the case without helium is due to the higher temperature of the gas inside the H II region surrounding the BH.
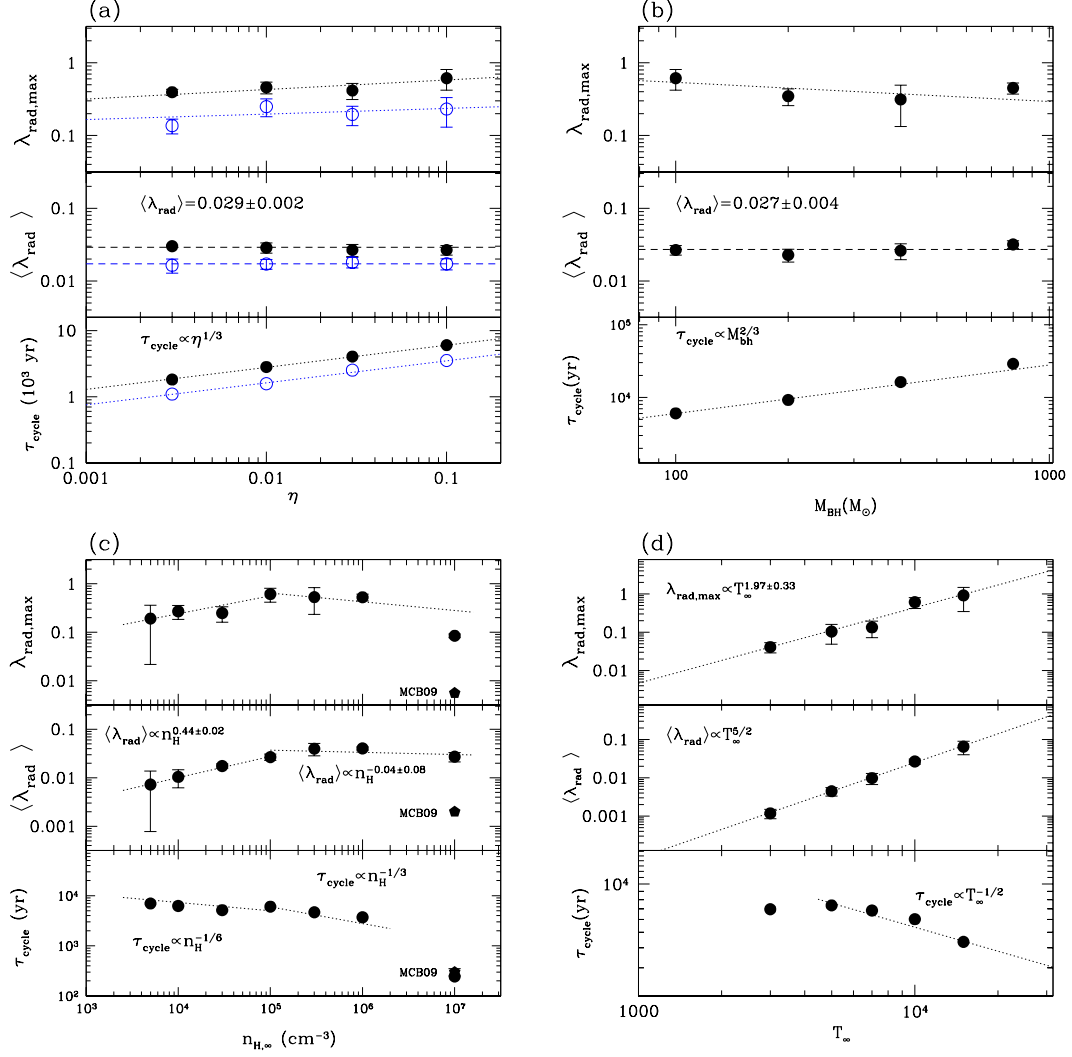
Figure 3.8: For each panel, peak accretion rate, average accretion rate and period between bursts are shown from top to bottom as a function of a given parameter. Error bars represent the standard deviation around the mean values over ~ 5 accretion cycles. *(a)* Dependence on η. $\langle\lambda_{\rm rad}\rangle \sim const$ while $\tau_{\rm cycle} \propto \eta^{1/3}$. Open symbols indicate the simulations including helium photo-heating and cooling, which show $\sim 41\%$ lower accretion rate and $\sim 42\%$ shorter period. *(b)* Same plots as a function of $M_{\rm bh}$. $\langle\lambda_{\rm rad}\rangle \sim const$ while $\tau_{\rm cycle} \propto M_{\rm bh}^{2/3}$. *(c)* Same plots as a function of $n_{\rm H,\infty}$ of gas. At low densities, $\tau_{\rm cycle} \propto n_{\rm H,\infty}^{-1/6}$, whereas at higher density, $\tau_{\rm cycle} \propto n_{\rm H,\infty}^{-1/3}$. *(d)* Same plots as a function of T_∞. Average accretion rate $\langle\lambda_{\rm rad}\rangle \propto T_\infty^{5/2}$. With an exception at lowest temperature $\tau_{\rm cycle} \propto T_\infty^{-1/2}$.

b) Dependence on BH mass

We explore a range in BH mass from 100 $M_\odot$ to 800 $M_\odot$, while keeping the other

parameters constant ($\eta = 0.1$, $n_{\mathrm{H},\infty} = 10^5$ cm^{-3} and $T_\infty = 10^4$ K). The results are shown in panel (b) of Figure 3.8. The mean accretion rate is $\langle \lambda_{\mathrm{rad}} \rangle \sim 2.7\% \pm 0.4\%$ and the maximum accretion rate is $\lambda_{\mathrm{rad,max}} \sim 42\% \pm 12\%$ ($\beta = -0.26 \pm 0.20$). They are both independent of M_{bh} within the error of the fit. The period of the bursts is well described by a power-law relation $\tau_{\mathrm{cycle}} \propto M_{\mathrm{bh}}^{2/3}$.

c) Dependence on gas density of the ambient medium

Panel (c) in Figure 3.8 shows the dependence of accretion rate and burst period on the ambient gas density, $n_{\mathrm{H},\infty}$. We explore a range of $n_{\mathrm{H},\infty}$ from 5×10^3 cm^{-3} to 10^7 cm^{-3}, while keeping the other parameters constant at $\eta = 0.1$, $M_{\mathrm{bh}} = 100$ M$_\odot$ and $T_\infty = 10^4$ K. For densities $n_{\mathrm{H},\infty} \geq 10^5$ cm^{-3}, $\langle \lambda_{\mathrm{rad}} \rangle$ and $\lambda_{\mathrm{rad,max}}$ are insensitive to $n_{\mathrm{H},\infty}$ ($\beta = -0.04 \pm 0.08$ and $\beta = -0.18 \pm 0.13$, respectively). However, for $n_{\mathrm{H},\infty} \leq 10^5$ cm^{-3}, $\langle \lambda_{\mathrm{rad}} \rangle$ and $\lambda_{\mathrm{rad,max}}$ are proportional to $n_{\mathrm{H},\infty}^{1/2}$ ($\beta = 0.44 \pm 0.02$ and $\beta = 0.37 \pm 0.09$, respectively).

The bottom of Figure 3.8(c) shows the effect of density in determining the oscillation period. For densities $n_{\mathrm{H},\infty} \geq 10^5$ cm^{-3}, τ_{cycle} is fitted well by a power law with $\tau_{\mathrm{cycle}} \propto n_{\mathrm{H},\infty}^{-1/3}$ and for the densities $n_{\mathrm{H},\infty} \leq 10^5$ cm^{-3} it is fitted well by a power law $\tau_{\mathrm{cycle}} \propto n_{\mathrm{H},\infty}^{-1/6}$. However, τ_{cycle} at $n_{\mathrm{H},\infty} = 10^7$ cm^{-3} is lower than predicted by the power law fit for $n_{\mathrm{H},\infty} \geq 10^5$ cm^{-3}. Although Figure 3.5, 3.7 do not show clearly the magnitude of accretion rate during the inactive phase, it is evident in a log-log plot that accretion rate at minima is 4 orders of magnitude lower than during the peak of the burst. This is the case for all simulations but the ones with $n_{\mathrm{H},\infty} = 10^7$ cm^{-3} in which the accretion rate at minima is 2 orders of magnitude higher than in all other simulations. The simulations show that the ambient gas density is an important parameter in determining the accretion luminosity and period between bursts of the IMBH. One of the reasons is that the gas temperature inside the hot ionized

bubble and the thickness and density of the dense shell in front of it depend on the density via the cooling function. The drop in the accretion rate we observe at low densities can be linked to an increase of the temperature within the sonic radius with respect to simulations with higher ambient density. This results in an increase in the pressure gradient within the ionized bubble that reduces the accretion rate significantly.

d) Dependence on the temperature of the ambient medium

Panel (d) in Figure 3.8 shows the dependence of accretion rate and period of the bursts on the temperature of the ambient medium, T_∞. We vary T_∞ from 3000 K to 15000 K while keeping the other parameters constant at $\eta = 0.1$, $M_{\rm bh} = 100$ M$_\odot$ and $n_{\rm H,\infty} = 10^5$ cm^{-3}. We find $\langle \lambda_{\rm rad} \rangle$ and $\lambda_{\rm rad,max}$ depend steeply on T_∞ as $T_\infty^{5/2}$ ($\beta = 2.44 \pm 0.06$). Except for the simulation with $T_\infty = 3000$ K, the period of the accretion cycle is fitted well by a single power law $\tau_{\rm cycle} \propto T_\infty^{-1/2}$.

3.4 Analytical Formulation of Bondi Accretion with Radiative Feedback

In this section we use the fitting formulas for $\langle \lambda_{\rm rad} \rangle$, $\lambda_{\rm rad,max}$ and $\tau_{\rm cycle}$ obtained from the simulations, to formulate an analytic description of the accretion process. For ambient densities $n_{\rm H,\infty} \geq 10^5$ cm^{-3}, we have found that the dimensionless mean accretion rate $\langle \lambda_{\rm rad} \rangle$ depends only on the temperature of the ambient medium. It is insensitive to η, $M_{\rm bh}$ and $n_{\rm H,\infty}$. Thus, for $n_{\rm H,\infty} \geq 10^5$ cm^{-3} we find

$$\langle \lambda_{\rm rad} \rangle \sim 3.3\% \ T_{\infty,4}^{2.5} \ n_{\rm H,5}^{-0.04} \sim 3.3\% \ T_{\infty,4}^{5/2}, \tag{3.3}$$

while for $n_{\rm H,\infty} \leq 10^5$ cm^{-3} we find

$$\langle \lambda_{\rm rad} \rangle \sim 3.3\% \ T_{\infty,4}^{5/2} \ n_{\rm H,5}^{1/2}. \tag{3.4}$$

As mentioned above, the dependence of $\langle \lambda_{\mathrm{rad}} \rangle$ on the density is due to the increasing temperature inside the ionized bubble at low densities. The period of the accretion cycle depends on all the parameters we have investigated in our simulation. In the range of densities $n_{\mathrm{H},\infty} \geq 10^5$ cm^{-3} we find

$$\tau_{\mathrm{cycle}} = (6 \times 10^3 \text{ yr}) \; \eta_{-1}^{\frac{1}{3}} \; M_{\mathrm{bh},2}^{\frac{2}{3}} \; n_{\mathrm{H},5}^{-\frac{1}{3}} \; T_{\infty,4}^{-\frac{1}{2}} \tag{3.5}$$

where we use the notation of $M_{\mathrm{bh},2} \equiv M_{\mathrm{bh}}/(10^2 \text{ M}_\odot)$. However, at lower densities $n_{\mathrm{H},\infty} \leq 10^5$ cm^{-3}, we find

$$\tau_{\mathrm{cycle}} = (6 \times 10^3 \text{ yr}) \; \eta_{-1}^{\frac{1}{3}} \; M_{\mathrm{bh},2}^{\frac{2}{3}} \; n_{\mathrm{H},5}^{-\frac{1}{6}} \; T_{\infty,4}^{-\frac{1}{2}} \tag{3.6}$$

in which only the dependence on $n_{\mathrm{H},5}$ changes. The different dependence of τ_{cycle} on $n_{\mathrm{H},\infty}$ is associated with a change of the mean accretion rate $\langle \lambda_{\mathrm{rad}} \rangle$ for each density regime. The deviation of τ_{cycle} from the power law fit at $n_{\mathrm{H},\infty} = 10^7$ cm^{-3} is not associated with any variation of the mean accretion rate. Our value of τ_{cycle} for $n_{\mathrm{H},\infty} = 10^7$ cm^{-3} is in good agreement with the value found by MCB09.

3.5   Dimensionless accretion rate : $\langle \lambda_{\mathrm{rad}} \rangle$

In this section we seek a physical explanation for the relationship between the mean accretion rate $\langle \lambda_{\mathrm{rad}} \rangle$ and the temperature of the ambient medium found in the simulations. The model is valid in all the parameter space we have explored with a caveat in the low density regime ($n_{\mathrm{H},\infty} < 3 \times 10^5$ cm^{-3}) and at low ambient temperatures ($T_\infty < 3000$ K).

Figure 3.9 shows the time-averaged temperature profiles for simulations in which we vary η, M_{bh}, $n_{\mathrm{H},\infty}$ and T_∞. In the case of different M_{bh} the radii are rescaled so that direct comparisons can be made with the case of 100 M$_\odot$. Vertical lines indicate the accretion radius r_{acc}, inside of which gas is accreted and outside of which gas

is pushed out to the ionization front. We find that the value of $r_{\rm acc}$ is generally insensitive to the parameters of the simulation as is the gas temperature at $r_{\rm acc}$.

Accretion onto the BH of gas inside the hot ionized sphere is limited by the thermal pressure of the hot gas and by the outflow velocity of the gas that is produced by the pressure gradient inside the Strömgren sphere. Thus, the accretion radius, $r_{\rm acc}$, is analogous to the inner Bondi radius, $r_{\rm b,in}$, modified to take into account temperature and pressure gradient inside the hot bubble.

Let us assume that the average accretion rate onto the BH is

$$\langle \dot{M} \rangle = 4\pi \lambda_B r_{\rm acc}^2 \rho_{\rm in} c_{\rm s,in}, \tag{3.7}$$

where $\rho_{\rm in}$ and $c_{\rm s,in}$ (and the corresponding temperature $T_{\rm in}$) are the density and the sound speed at $r_{\rm acc}$. Based on the results illustrated in Figure 3.9, we expect the accretion rate to depend only on $\rho_{\rm in}$, since $r_{\rm acc}$ and $c_{\rm s,in}$ can be taken to be constants.

When a Strömgren sphere is formed, the gas inside the hot bubble expands and its density decreases. Inside the ionization front the temperature is about $10^4 - 10^5$K. Thus, assuming pressure equilibrium across the ionization front we find the dependence of $\rho_{\rm in}$ on T_∞:

$$\rho_{\rm in} \approx \rho_\infty \frac{T_\infty}{T_{\rm in}} = \rho_\infty \left(\frac{c_{\rm s,\infty}}{c_{\rm s,in}} \right)^2. \tag{3.8}$$

We find $f = r_{\rm acc}/r_{\rm b,in} \sim 1.8$ and the temperature at $r_{\rm acc}$ is $T_{\rm in} \sim 4 \times 10^4$ K independent of η, $M_{\rm bh}$, $n_{\rm H,\infty}$ and T_∞ for a fixed spectral index of radiation $\alpha = 1.5$. The dimensionless accretion rate inside of the Strömgren sphere normalized by the Bondi accretion rate in the ambient medium is then :

$$
\begin{aligned}
\langle \lambda_{\rm rad} \rangle &\simeq \lambda_B \frac{r_{\rm acc}^2 \rho_{\rm in} c_{\rm s,in}}{r_{\rm b,\infty}^2 \rho_\infty c_{\rm s,\infty}} \\
&\simeq \frac{1}{4}(1.8)^2 \left(\frac{\rho_{\rm in}}{\rho_\infty} \right) \left(\frac{c_{\rm s,in}}{c_{\rm s,\infty}} \right)^{-3} \\
&\simeq 3\% \, T_{\infty,4}^{5/2}
\end{aligned}
\tag{3.9}
$$
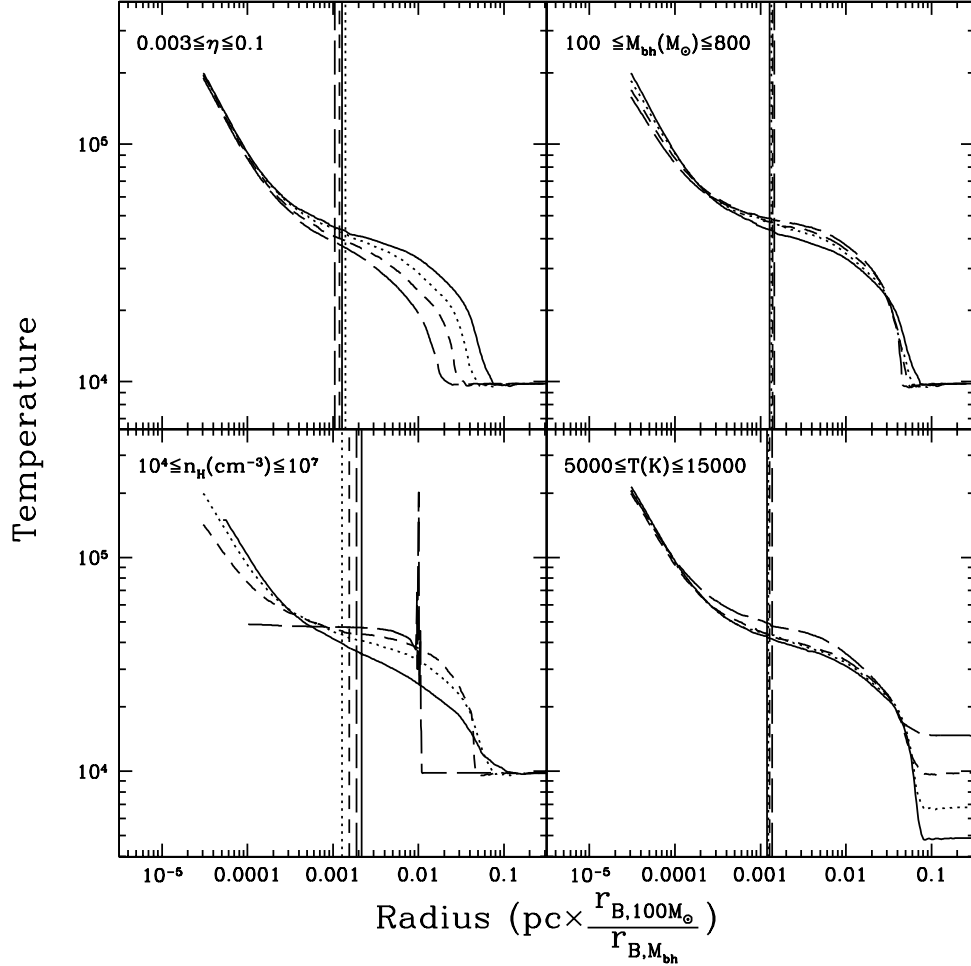
Figure 3.9: Time-averaged temperature profiles as a function of simulation parameters. Different vertical lines indicate accretion radii, $r_{\rm acc}$, for each parameter. *Top left* : η ranges from 0.1 (*solid line*) to 0.003 (*long dashed line*). *Top right* : $M_{\rm bh}$ ranges from 100 $M_\odot$ (*solid*) to 800 $M_\odot$ (*long dashed*). *Bottom left* : Density ranges from 10^4 cm^{-3} (*solid*) to 10^7 cm^{-3} (*long dashed*). *Bottom right* : T_∞ ranges from 5000K (*solid*) to 15000K (*long dashed*).

where we have used $\lambda_B = 1/4$ appropriate for an adiabatic gas. Thus, $\langle \lambda_{\rm rad} \rangle \propto T_\infty^{5/2}$ which is in agreement with the simulation result, given that $r_{\rm acc}$ and $T_{\rm in}$ remain constant when we change the simulation parameters. However, $r_{\rm acc}$ and $T_{\rm in}$ may not stay constant if we modify the cooling or heating function, for instance by increasing the gas metallicity or by changing the spectrum of radiation; this result suggests that the accretion rate is very sensitive to the details of the temperature structure

inside the Strömgren sphere which shows a dependence on $n_{H,\infty}$. The temperature profile changes significantly for $n_{H,\infty} < 3 \times 10^4$ cm^{-3} and this is probably the reason why our model does not fit perfectly $\langle \lambda_{rad} \rangle$ from the simulations in the lower density regime. In the next section we test whether Equation (3.7) is still a good description of our results when we change the thermal structure inside the H II region.

3.6 Dependence on temperature at accretion radius

In this section we study the dependence of the accretion rate on the time-averaged temperature T_{in} at r_{acc}. We change the temperature T_{in} by varying the spectral index α of the radiation spectrum and by including Compton cooling of the ionized gas by CMB photons. Here we explore the spectral index of the radiation spectrum in the range $\alpha = 0.5, 1.0, 1.5, 2.0, 2.5$ with the energy of photons from 10 eV 100 keV. The other parameters are kept constant at $\eta = 0.1$, $M_{bh} = 100$ M$_\odot$, $n_{H,\infty} = 10^5$ cm^{-3} and $T_\infty = 10^4$ K.

Figure 3.10 shows the different time-averaged temperature profiles for different values of α. Spectra with lower values of the spectral index α produce more energetic photons for a given bolometric luminosity, increasing the temperature inside the ionized bubble. Simulations show that the averaged accretion rate $\langle \lambda_{rad} \rangle$ increases for softer spectrum of radiation. Different slopes ($0.5 \leq \alpha \leq 2.5$) of the power-law spectrum lead to different T_{in} (59000 K to 36000 K) and $\langle \lambda_{rad} \rangle$ (0.0076 to 0.0509). Adopting a harder spectrum (with $\alpha = 0.5$) instead of the softer ($\alpha = 2.5$) increases T_{in} by a factor of 1.6 and $\langle \lambda_{rad} \rangle$ decreases by a factor 6.7. The fit to the simulation results in Figure 3.11 show that $\langle \lambda_{rad} \rangle$ depends on temperature at r_{acc} as

$$\langle \lambda_{rad} \rangle \propto T_{in}^{-4} \propto c_{s,in}^{-8}. \tag{3.10}$$
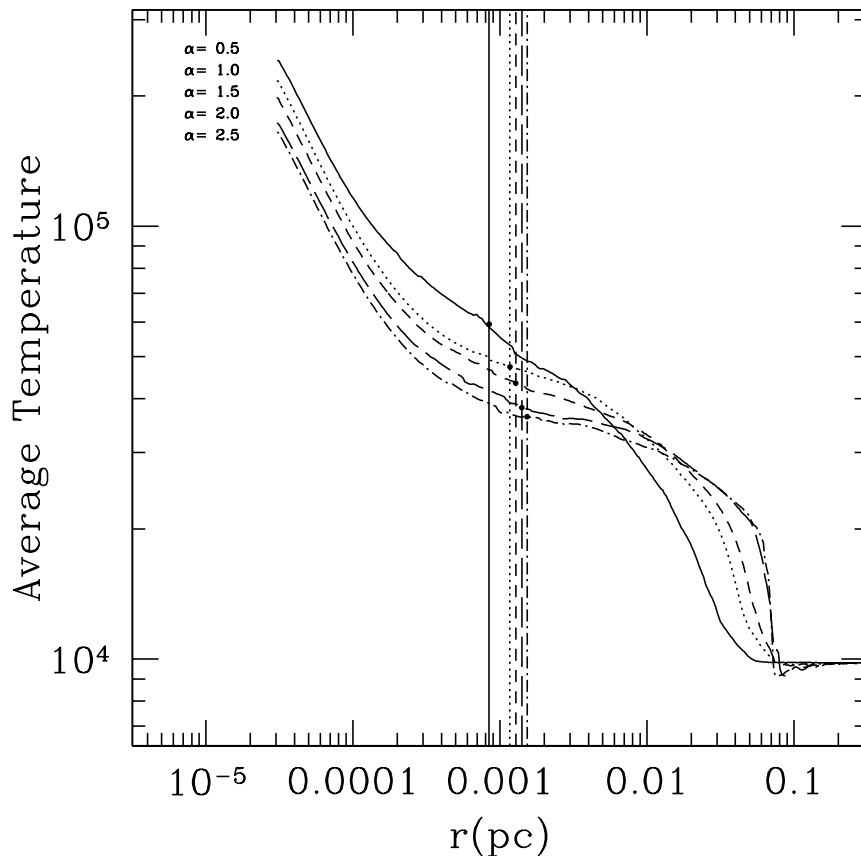
Figure 3.10: Average temperature profiles of the H II region as a function of spectral index α. Smaller α results in smaller r_{acc} and higher T_{in}.

The dependence on $c_{\mathrm{s,in}}$ differs from equation (3.9). However this is not surprising because in these simulations the values of r_{acc} and $c_{\mathrm{s,in}}$ do not remain constant while we vary the value of the spectral index α. This is due to a change of the temperature and pressure gradients within the H II region. The accretion radius, r_{acc}, can be expressed as a function of the Bondi radius inside the hot bubble, $r_{\mathrm{b,in}} = GM_{\mathrm{bh}}c_{\mathrm{s,in}}^{-2}$. From the simulations we obtain the following relationship between these two radii:

$$f = \frac{r_{\mathrm{acc}}}{r_{\mathrm{b,in}}} \simeq 1.8 \left(\frac{T_{\mathrm{in}}}{4 \times 10^4 \ \mathrm{K}} \right)^{-0.7 \pm 0.2}. \tag{3.11}$$

Thus, if our model for the accretion rate summarized by equation (3.7) is valid,
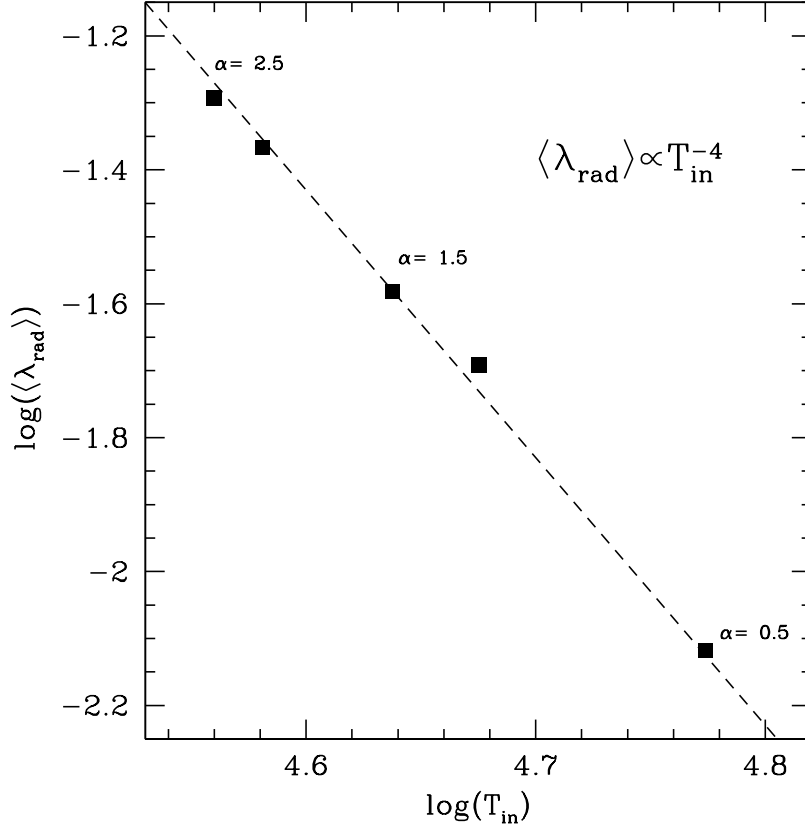
Figure 3.11: Relation between temperature at $r_{\rm acc}$ and average accretion rate $\langle \lambda_{\rm rad} \rangle$. We find $\langle \lambda_{\rm rad} \rangle \propto T_{\rm in}^{-4}$.

we should have:

$$
\begin{aligned}
\langle \lambda_{\rm rad} \rangle \quad &\simeq \quad \frac{1}{4} \frac{r_{\rm acc}^2 \rho_{\rm in} c_{\rm s,in}}{r_{\rm b,\infty}^2 \rho_\infty c_{\rm s,\infty}} \simeq \frac{(1.8)^2}{4} \left(\frac{\rho_{\rm in}}{\rho_\infty} \right) c_{\rm s,in}^{-5.9} c_{\rm s,\infty}^3 \\
&\simeq \quad 3\% \, T_{\infty,4}^{2.5} \left(\frac{T_{\rm in}}{4 \times 10^4 \ {\rm K}} \right)^{-4},
\end{aligned}
\tag{3.12}
$$

in agreement with the simulation results $\langle \lambda_{\rm rad} \rangle \propto T_\infty^{2.5} T_{\rm in}^{-4}$ where the dependence on $T_{\rm in}$ was not explored initially. Thus, Bondi-like accretion on the scale of $r_{\rm acc}$ is indeed a good explanation of our results. Given the steep dependence of the value of accretion rate $\langle \lambda_{\rm rad} \rangle$ on $T_{\rm in}$ it is clear that it is very sensitive on the details of the thermal structure inside the H II region. This means that $\langle \lambda_{\rm rad} \rangle$ depends on the spectrum of radiation and gas metallicity.

3.7 Accretion rate at peaks and duty cycle: $\lambda_{\rm rad,max}$, $f_{\rm duty}$

We estimate $f_{\rm duty}$ by comparing $\lambda_{\rm rad,max}$ and $\langle\lambda_{\rm rad}\rangle$ using Equation (3.2). This quantity gives an estimate of what fraction of BHs are accreting gas at the rate close to the maximum. Within the fitting errors, the log slopes of $\lambda_{\rm rad,max}$ and $\langle\lambda_{\rm rad}\rangle$ as a function of the parameters $M_{\rm bh}$, T_∞ are zero. Thus, we assume that the dimensionless accretion rates are independent of these parameters.

For $n_{\rm H,\infty} \geq 10^5\,{\rm cm}^{-3}$, $\lambda_{\rm rad,max}$ can be expressed as $\lambda_{\rm rad,max} \sim 0.55\,\eta_{-1}^{0.13}\,n_{\rm H,5}^{-0.18}\,T_{\infty,4}^{2.0}$ and the dependence of $f_{\rm duty}$ on these parameters can be expressed using equation (3.3) as

$$f_{\rm duty} \quad \sim \quad 6\%\,\eta_{-1}^{-0.13}\,n_{\rm H,5}^{0.14}\,T_{\infty,4}^{0.5} \tag{3.13}$$

where we include the mild dependence of $\langle\lambda_{\rm rad}\rangle$ on the density. For $n_{\rm H,\infty} \leq 10^5\,{\rm cm}^{-3}$, $\lambda_{\rm rad,max} \sim 0.55\,\eta_{-1}^{0.13}\,n_{\rm H,5}^{0.37}\,T_{\infty,4}^{2.0}$ has a different power law dependence on the density and we get $f_{\rm duty}$ as

$$f_{\rm duty} \quad \sim \quad 6\%\,\eta_{-1}^{-0.13}\,n_{\rm H,5}^{0.07}\,T_{\infty,4}^{0.5} \tag{3.14}$$

where $f_{\rm duty}$ shows a milder dependence on the gas density. Thus, we expect about 6% of IMBHs to be accreting near the maximum rate at any given time. This value depends weakly on η, $n_{\rm H,\infty}$ and T_∞.

3.8   Average period between bursts : τ_{cycle}

In this section we derive an analytical expression for the period of the luminosity bursts as a function of all the parameters we tested. Although τ_{cycle} shows a seemingly complicated power law dependencies on the free parameters, we find that τ_{cycle} is proportional to the time-averaged size of the Strömgren sphere. This is shown in Figure 3.12. The linear relation between τ_{cycle} and the average Strömgren radius $\langle R_s \rangle$ explains the dependence of τ_{cycle} on every parameter considered in this work.

The number of ionizing photons created by accretion onto a BH is determined by the average accretion rate and the radiative efficiency η. The average accretion rate itself can be expressed as a fraction of the Bondi accretion rate $\langle \lambda_{\mathrm{rad}} \rangle$. Therefore, the average number of ionizing photons emitted near the BH can be expressed as

$$
\begin{aligned}
N_{\mathrm{ion}} \quad &\propto \quad \eta \langle \lambda_{\mathrm{rad}} \rangle \dot{M}_B \\
&\propto \quad \eta \langle \lambda_{\mathrm{rad}} \rangle \frac{G^2 M_{\mathrm{bh}}^2}{c_{\mathrm{s},\infty}^3} \rho_\infty.
\end{aligned}
\tag{3.15}
$$

It follows that:

$$
\begin{aligned}
\tau_{\mathrm{cycle}} \quad = \quad t_{\mathrm{out}} &\approx \frac{\langle R_s \rangle}{v_{\mathrm{out}}} \propto \left(\frac{3 N_{\mathrm{ion}}}{4\pi \alpha_{\mathrm{rec}} n_H^2} \right)^{\frac{1}{3}} \\
&\propto \quad \left(\frac{1}{n_H^2} \right)^{\frac{1}{3}} \left(\eta \langle \lambda_{\mathrm{rad}} \rangle \frac{G^2 M_{\mathrm{bh}}^2}{c_{\mathrm{s},\infty}^3} \rho_\infty \right)^{\frac{1}{3}},
\end{aligned}
\tag{3.16}
$$

where we find $v_{\mathrm{out}} \sim \frac{1}{3} c_{\mathrm{s,in}}$. Ignoring constant coefficients and using equation (3.3) for $n_{\mathrm{H},\infty} \geq 10^5$ cm^{-3}, we find :

$$
\tau_{\mathrm{cycle}} \quad \propto \quad \eta^{\frac{1}{3}} M_{\mathrm{bh}}^{\frac{2}{3}} n_{\mathrm{H},\infty}^{-\frac{1}{3}} T_\infty^{-\frac{1}{2}},
\tag{3.17}
$$

or using equation (3.4) for $n_{\mathrm{H},\infty} \leq 10^5$ cm^{-3}, we find :

$$
\tau_{\mathrm{cycle}} \quad \propto \quad \eta^{\frac{1}{3}} M_{\mathrm{bh}}^{\frac{2}{3}} n_{\mathrm{H},\infty}^{-\frac{1}{6}} T_\infty^{-\frac{1}{2}}
\tag{3.18}
$$

which are exactly as in the empirical fitting formulas in both density regimes and also in good agreement with the analytical work by MBCO09. This explains the dependence of τ_{cycle} on any tested parameter η, M_{bh}, $n_{\text{H},\infty}$ and T_∞. In Figure 3.12 we also show simulation results assuming $\eta \propto \dot{m}$. All simulations show the same relationship between τ_{cycle} and $\langle R_s \rangle$. However, the simulation with the highest ambient density ($n_{\text{H},\infty} = 10^7$ cm^{-3}) deviates from the linear relationship, but is in agreement with the numerical simulation by MCB09. It appears that in the high density regime τ_{cycle} decreases steeply with decreasing $\langle R_s \rangle$.

We can interpret τ_{cycle} as the time scale at which the gas inside H II region gets depleted. If the gas depletion inside the Strömgren sphere is dominated by the outward gas flow, then $\tau_{\text{cycle}} \propto \langle R_s \rangle / c_{\text{s,in}}$ in agreement with the empirical linear relation in Figure 3.12. However, the depletion time scale may be different if the accretion by the BH dominates gas consumption inside the Strömgren sphere. We can derive this time scale as

$$t_{\text{in}} = \frac{M_{\text{H II}}}{\dot{M}} = \left(\frac{\langle R_s \rangle}{r_{\text{acc}}} \right)^2 \frac{\langle R_s \rangle}{3 \, c_{\text{s,in}}} \sim \left(\frac{\langle R_s \rangle}{r_{\text{acc}}} \right)^2 \frac{t_{\text{out}}}{9}. \tag{3.19}$$

Roughly, we expect $\tau_{\text{cycle}} = \min(t_{\text{out}}, t_{\text{in}})$. So, for $\langle R_s \rangle / r_{\text{acc}} \leq 3$, the period of the cycle scales as $\langle R_s \rangle^3$. This may explain the deviation of the period for $n_{\text{H},\infty} = 10^7$ cm^{-3} from the linear relation. We see in Figure 3.9 that the ratio $\langle R_s \rangle / r_{\text{acc}} \sim 5$ for $n_{\text{H},\infty} = 10^7$ cm^{-3} which is much smaller than the ratio found for other densities.

3.9 Rayleigh-Taylor instability

In 2D simulations we find that RT instability develops across the Strömgren radius especially when I-front is accelerated outward in the radial direction, thus the net effective acceleration on the shell increases momentarily. The shell is RT unstable, but because the gravitational acceleration at the shell location is weak,
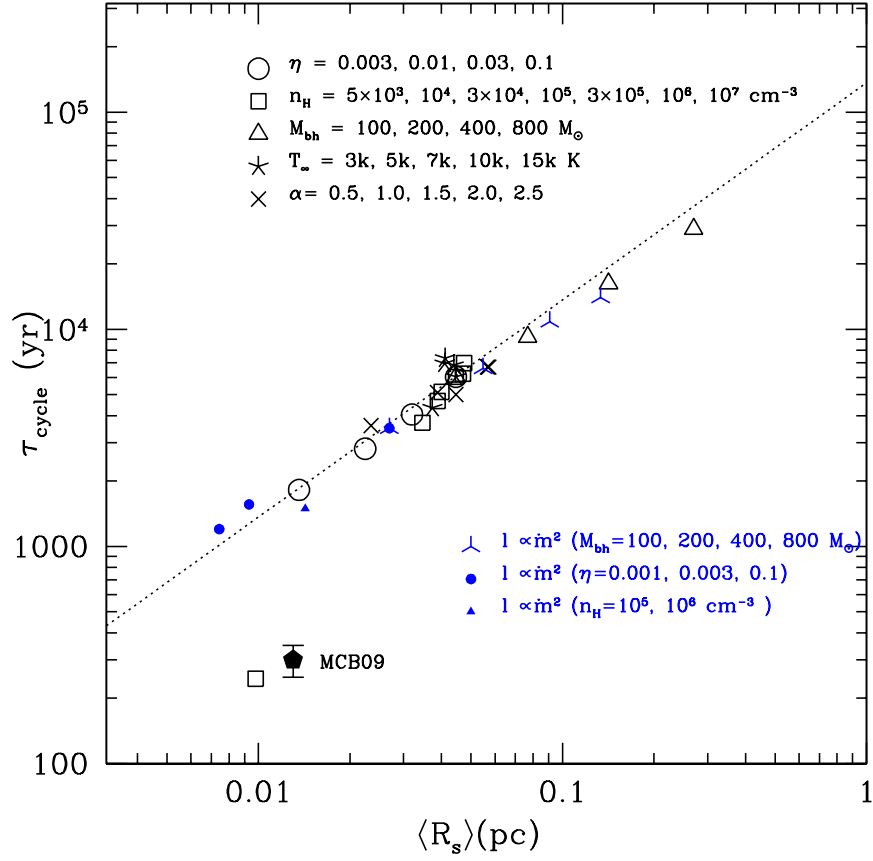
Figure 3.12: Period of accretion bursts as a function of the average Strömgren radius. All simulation results from all the parameters are plotted together. The average size of the Strömgren sphere shows a linear relation with the period τ_{cycle}. The only exception happens at the highest density ($n_{\text{H},\infty} = 10^7$ cm^{-3}), but this result is in agreement with the work by MCB09 (symbol with error bar)

only perturbations with wavelength $\lambda_{\text{RT}} < \langle R_s \rangle/(2\pi\alpha)$ can grow during a cycle. Here, $\alpha = \langle R_s \rangle/r_{\text{b,in}} \sim 10 - 50$ is the ratio of the shell radius and the inner Bondi radius. However, the linear growth of small wavelength perturbations that are not self-shielding to ionizing radiation is inhibited by photo-ionization/heating. Indeed in the simulation movies we observe that when finger-like dense features from the dense shell develop into the H II region, they experience stronger photo-ionization/heating when get closer to the BHs. Only the densest clumps can survive the photo-ionization for extended time due to self-shielding from the ionization as

observed in some simulation movies.

In the linear regime the growth time scale of the RT instability of wavelength λ_{RT} is

$$\tau_{\mathrm{RT}} \simeq \sqrt{\frac{\rho_{\mathrm{sh}} + \rho_{\mathrm{in}}}{\rho_{\mathrm{sh}} - \rho_{\mathrm{in}}} \frac{2\pi\lambda_{\mathrm{RT}}}{g}} \simeq \sqrt{\frac{2\pi\lambda_{\mathrm{RT}}}{g}}$$

where ρ_{sh} is the density of the shell and $g \simeq GM_{\mathrm{bh}}\langle R_s\rangle^{-2}$ is the gravitational acceleration at the shell radius. Thus, RT timescale can be expressed as

$$\tau_{\mathrm{RT}} \simeq \frac{\langle R_s\rangle}{c_{\mathrm{s,in}}} \sqrt{\frac{2\pi\lambda_{\mathrm{RT}}}{r_{\mathrm{b,in}}}}. \tag{3.20}$$

So during one cycle perturbations grow on scales:

$$\lambda_{\mathrm{RT}} < \left(\frac{\tau_{\mathrm{RT}}}{\tau_{\mathrm{cycle}}}\right)^2 \frac{r_{\mathrm{b,in}}}{2\pi} < \frac{r_{\mathrm{b,in}}}{2\pi}$$

where $r_{\mathrm{b,in}}$ is the inner Bondi radius. Thus only instability on angular scales $\theta \sim \lambda_{\mathrm{RT}}/2\pi\langle R_s\rangle \leq r_{\mathrm{b,in}}/(2\pi)^2\langle R_s\rangle$ grow in our simulation.

Chapter 4

Growth Rate and Duty Cycle

Abstract : This chapter focuses on the effects of radiation pressure and angular momentum of the accreting gas. We simulate accretion onto intermediate-mass black holes, but we derive general scaling relationships that are solutions of the Bondi problem with radiation feedback valid for any mass of the BH $M_{\rm bh}$. Thermal pressure of the ionized sphere around the BH regulates the accretion rate producing periodic and short-lived luminosity bursts. We find that for ambient gas densities exceeding $n_{\rm H,\infty}^{\rm cr} \propto M_{\rm bh}^{-1}$, the period of the oscillations decreases rapidly and the duty cycle increases from 6%, in agreement with observations of the fraction of active galactic nuclei at $z \sim 3$, to 50%. The mean accretion rate becomes Eddington limited for $n_{\rm H,\infty} > n_{\rm H,\infty}^{\rm Edd} \simeq n_{\rm H,\infty}^{\rm cr} T_{\infty,4}^{-1}$. In the sub-Eddington regime, the mean accretion rate onto BHs is about $1\% T_{\infty,4}^{5/2}$ of the Bondi rate, thus is proportional to the thermal pressure of the ambient medium. The period of the oscillations coincides with depletion timescale of the gas inside the ionized bubble surrounding the BH. Gas depletion is dominated by a pressure gradient pushing the gas outward if $n_{\rm H,\infty} < n_{\rm H,\infty}^{\rm cr}$ and by accretion onto the BH otherwise. Generally, for $n_{\rm H,\infty} < n_{\rm H,\infty}^{\rm cr}$ angular momentum does not affect significantly the accretion rate and period of the oscillations.

Introduction : In this chapter, we show the results of simulations discussing the effects of helium heating/cooling, radiation pressures, and angular momentum on the BH accretion rate. All the simulations in this Chapter include helium heating/cooling but the gas is metal free. The simulations remain qualitatively the same as in Chapter 3 where we did not include helium; the only noticeable difference with respect to Chapter 3 is that the accretion rate at peak luminosity shows multiple minor peaks instead of a well-defined single peak. This is to be expected, as a larger opacity produces a stronger feedback with respect to the hydrogen only case, leading to multiple shocks in the gas. This complicate structure – i.e., a burst consisting of several sub-bursts – is commonly found (e.g., Ciotti and Ostriker 2007). In addition, the average accretion rate $\langle \lambda_{\mathrm{rad}} \rangle$ decreases from $\sim 3\%$ to $\sim 1\%$, but this can be understood by the increase of the mean temperature inside the Strömgren sphere to from $T_{\mathrm{in}} \sim 4 \times 10^4$ K to $\sim 6 \times 10^4$ K. The top panel of Figure 4.1 shows the accretion rate as a function of $\eta = 0.01\text{-}0.1$ with $M_{\mathrm{bh}} = 100\ M_{\odot}$, 10^6 cm^{-3}, and $T_{\infty} = 10^4$ K. Large symbols show $\langle \lambda_{\mathrm{rad}} \rangle$ while small symbols show $\lambda_{\mathrm{rad,max}}$. For the given set of parameters, the luminosity remains in the sub-Eddington regime, thus the effects of radiation pressures are minor. The bottom panel of Figure 4.1 shows the dependence of τ_{cycle} on $\eta^{1/3}$, the same as found in Chapter 3. However, τ_{cycle} for $\eta = 0.1$ is now ~ 2200 years which is $\sim 60\%$ of the value found in Chapter 3 for the given set of parameters. This is also well understood (see Equation (3.16) in Chapter 3) as our model predicts $\tau_{\mathrm{cycle}} \propto \langle \lambda_{\mathrm{rad}} \rangle^{1/3}$.

4.1 Effect of Radiation Pressures

In Chapter 3, we have focused on exploring the parameter space in which the mean accretion rate is dominated by thermal feedback, i.e., radiation pressure can be neglected. We found $\langle \lambda_{\mathrm{rad}} \rangle \sim 1\%$ for $n_{\mathrm{H},\infty} = 10^5$ cm^{-3}, assuming $M_{\mathrm{bh}} = 100\ M_\odot$, $T_\infty = 10^4$ K, $\alpha = 1.5$, and including helium cooling/heating. However, not surprisingly, including the effect of radiation pressure produces a reduction of the accretion rate when the BH luminosity approaches the Eddington limit. Figure 4.2 shows $\langle \lambda_{\mathrm{rad}} \rangle$ as a function of gas density for a 100 $M_\odot$ BH, comparing simulations that do not include radiation pressure (open triangles) to ones including pressure on H I only (open squares), on e^- only (open pentagons), and the total effect of radiation pressure (solid circles). Compton radiation pressure reduces the accretion rate below $\langle \lambda_{\mathrm{rad}} \rangle \sim 1\%$ for $n_{\mathrm{H},\infty} \gtrsim 10^7$ cm^{-3} while the radiation pressure on H I appears always negligible with respect to Compton scattering. Both $\langle \lambda_{\mathrm{rad}} \rangle$ and $\lambda_{\mathrm{rad,max}}$ change from a constant fraction of the Bondi accretion rate to the Eddington rate λ_{Edd}, shown by the dashed line for $M_{\mathrm{bh}} = 100\ M_\odot$ and radiative efficiency $\eta = 0.1$.

Figure 4.3 shows the dimensionless accretion rates $\langle \lambda_{\mathrm{rad}} \rangle$ and $\lambda_{\mathrm{rad,max}}$ as a function of the BH mass from $M_{\mathrm{bh}} = 10^2$ to $10^4\ M_\odot$, keeping the other parameters constant: $\eta = 0.1$, 10^5 cm^{-3}, and $T_\infty = 10^4$ K. The simulations include radiation pressures on H I and e^-, and show that the transition to Eddington-limited accretion happens for $M_{\mathrm{bh}} \simeq 5000\ M_\odot$.
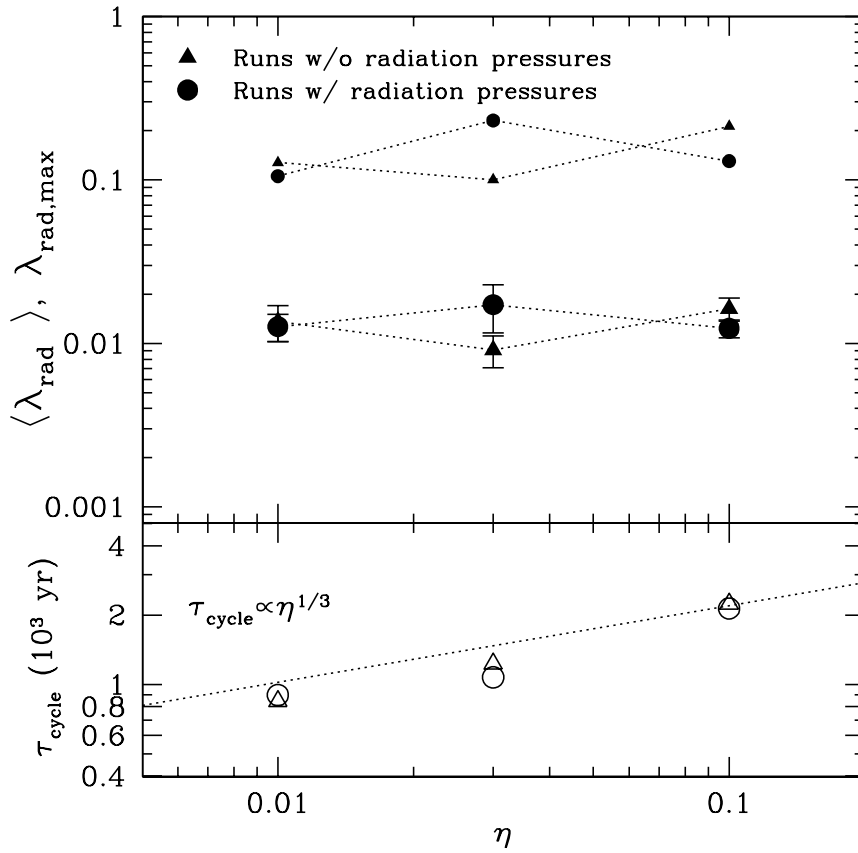
Figure 4.1: Top: accretion rate in units of the Bondi rate as a function of radiative efficiency η for simulations with $M_{\mathrm{bh}} = 100 \, M_\odot$, $10^6 \, \mathrm{cm}^{-3}$, and $T_\infty = 10^4$ K. Large symbols indicate mean accretion rate ($\langle \lambda_{\mathrm{rad}} \rangle \sim 1\%$), while small symbols show accretion rate at peaks ($\lambda_{\mathrm{rad,max}} \sim 20\%$). Bottom: period between bursts τ_{cycle} as a function η. The dotted line shows $\tau_{\mathrm{cycle}} \propto \eta^{1/3}$. In both panels, triangles represent simulations neglecting the effect of radiation pressures, while circles show simulations including radiation pressures. Radiation pressures introduce a minor difference in both the accretion rate and period of the bursts for this parameter set.

4.1.1 Transition from Bondi-like to Eddington-limited Accretion

So far the simulation results have shown that Compton scattering on electrons is the dominant radiation pressure effect, thus the Eddington-limit applies. Figure 4.4 summarizes the results of a large set of simulations that include radiation pressure.
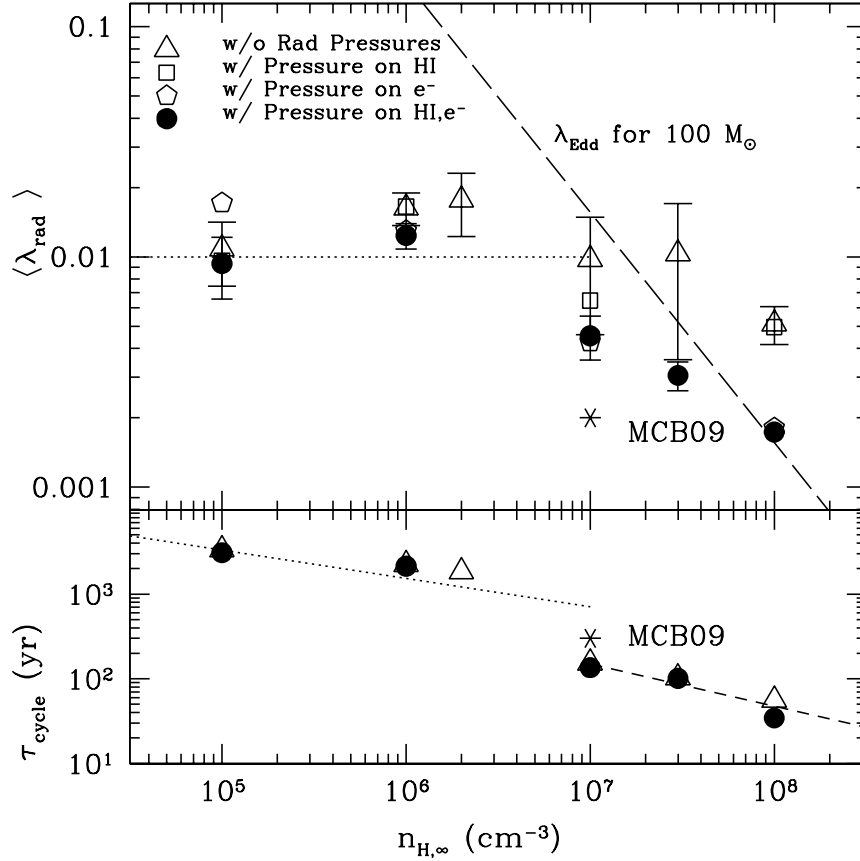
Figure 4.2: Comparison of relative importance of radiation pressures in regulating mean accretion rate (top panel) and the period of bursts (bottom panel) as a function of the ambient gas density $n_{H,\infty}$. Symbols are explained in the legend of the figure. Top: long dashed line shows the Eddington limit for a 100 $M_\odot$ BH with $\eta = 0.1$. When the accretion rate is sub-Eddington ($n_{H,\infty} \leq 10^6$ cm^{-3}) radiation pressures both on electrons and H I do not play an important role and the thermal structure of the Strömgren sphere regulates the accretion. Radiation pressure is important in reducing the accretion rate at $n_{H,\infty} = 10^7$ cm^{-3} where the accretion rate approaches the Eddington rate. The transition of accretion rate from $\langle \lambda_{rad} \rangle \sim$ 1% to the Eddington-limited regime happens at $n_{H,\infty}^{Edd} \sim 4 \times 10^6$ cm^{-3} for a 100 $M_\odot$ BH with $\eta = 0.1$ and $T_\infty = 10^4$ K. Bottom: radiation pressures do not produce significant differences in τ_{cycle}. Transition of τ_{cycle} from mode-I (dotted line) to mode-II (short dashed line) happens at the critical density $n_{H,\infty}^{cr} \sim n_{H,\infty}^{Edd}$ (see Section 4.2). The result shows a good agreement with the work of MCB09.

The top three panels in Figure 4.4(a) shows $\langle \lambda_{rad} \rangle$ as a function of gas density for $M_{bh} = 10^2, 10^3,$ and 10^4 $M_\odot$, respectively. For each BH mass, corresponding Eddington limits are shown by the dashed lines. The panels show the mean accretion

Figure 4.3: Same as Figure 4.1, but showing $\langle\lambda_{\rm rad}\rangle$, $\lambda_{\rm rad,max}$, and $\tau_{\rm cycle}$ as a function of $M_{\rm bh}$ with $\eta = 0.1$, 10^5 cm^{-3}, and $T_\infty = 10^4$ K. A similar pattern which we observe as a function of density is also seen as a function of $M_{\rm bh}$. With increasing $M_{\rm bh}$, the transition from $\langle\lambda_{\rm rad}\rangle \sim 1\%$ to the Eddington-limited regime and the transition of $\tau_{\rm cycle}$ from mode-I to mode-II happen at $M_{\rm bh} \sim 4\times 10^3$ $M_\odot$.

rate $\langle\lambda_{\rm rad}\rangle$ (large triangles) and $\lambda_{\rm rad,max}$ (small triangles) transitioning from being a constant fraction of the Bondi rate at low densities to being Eddington-limited at higher densities. The period of the accretion $\tau_{\rm cycle}$, in the bottom panels, also shows different dependencies in Bondi-like and Eddington-limited regimes. We will come back to this in Section 4.2.

Figure 4.4(b) shows the mean accretion luminosity in units of $L_{\rm Edd}$ for $M_{\rm bh} = 10^2, 10^3,$ and 10^4 $M_\odot$ as a function of gas density. The dotted lines show 1% of the Bondi accretion rate for each BH mass. Thus, from Figure 4.4 approximately we
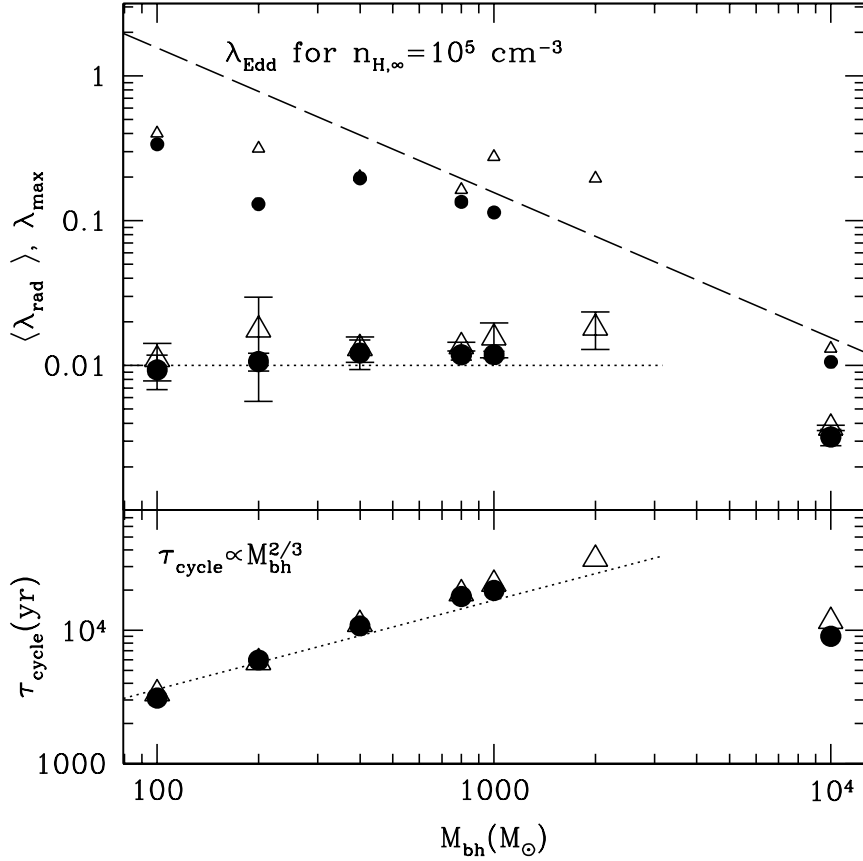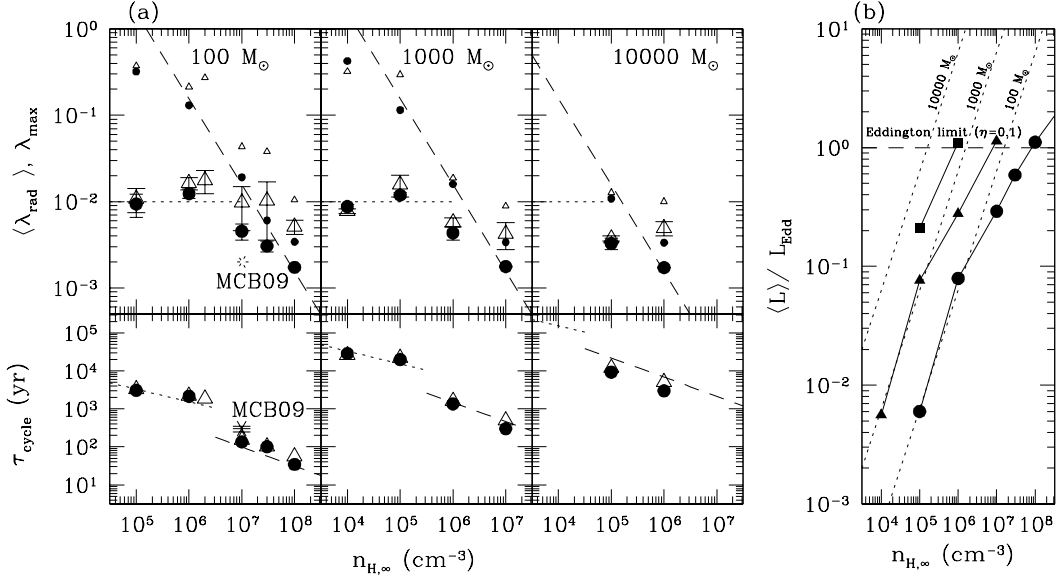
Figure 4.4: Left: same as Figure 4.2, but showing $\langle\lambda_{rad}\rangle$, $\lambda_{rad,max}$, and τ_{cycle} as a function of gas density for $M_{bh} = 10^2\ M_\odot$ (left panel), $10^3\ M_\odot$ (middle panel), and $10^4\ M_\odot$ (right panel). Long dashed lines in each panel show the Eddington accretion rate for $\eta = 0.1$ and the given BH mass. With increasing gas density, the accretion rate eventually becomes Eddington limited, but the transition to the Eddington-limited regime occurs at densities $n_{H,\infty}^{Edd} \sim 4 \times 10^6\ cm^3 M_{bh}^{-1}$ decreasing linearly with increasing BH mass. Right: accretion luminosities normalized by Eddington luminosities for the same simulations in the left figure. Symbols (circles: $10^2\ M_\odot$, triangles: $10^3\ M_\odot$, squares: $10^4\ M_\odot$) show the simulations including radiation pressures for each BH mass. With increasing gas density, the accretion rate becomes regulated primarily by Compton radiation pressure.

have

$$\langle \dot{M} \rangle = \min(1\% T_{\infty,4}^{5/2} \dot{M}_B, \eta^{-1} \dot{M}_{Edd}), \tag{4.1}$$

where $T_{\infty,4} \equiv T_\infty/(10^4\ K)$, valid for density $n_{H,\infty} \gtrsim 10^5\ cm^{-3}$, and $\alpha = 1.5$.

It is thus apparent that IMBHs can grow at a rate near the Eddington limit if the gas density of the environment is larger than the critical density

$$n_{H,\infty}^{Edd} \sim 4 \times 10^6\ cm^{-3} \left(\frac{M_{bh}}{10^2\ M_\odot} \right)^{-1} \left(\frac{T_\infty}{10^4\ K} \right)^{-1} \left(\frac{\eta}{0.1} \right)^{-1}. \tag{4.2}$$

4.1.2 Why is Continuum Radiation Pressure Negligible?

As shown in Figure 4.2-4.4, the simulations show that radiation pressure on H I does not play an important role when the accretion rate is sub-Eddington. In this section, we focus on understanding why this is. Figure 4.5 shows the evolution of relative magnitude of acceleration due to radiation pressures normalized by the gravitational acceleration at a given radius. Each panel refers to a different density $n_{\mathrm{H},\infty} = 10^5, 10^6, 10^7,$ and 10^8 cm^{-3}. Within the Strömgren sphere, the relative effect of Compton radiation pressure remains constant as a function of the radius since the electron fraction x_{e^-} is close to unity and the gas is nearly transparent to ionizing radiation. Outside of the Strömgren sphere, the rapid decrease of the electron fraction reduces the effect of Compton scattering. Radiation pressure on H I (thick lines in Figure 4.5) increases as a function of radius and has its peak value just inside the Strömgren sphere. This is due to the increase of the H I fraction as a function of radius. Outside the Strömgren sphere the relative effect of H I radiation pressure drops quickly because the ionizing luminosity decreases rapidly due to the increase of the H I opacity.

Continuum radiation pressure on H I is comparable to Compton electron scattering only in a shell just inside the Strömgren sphere, where the H I abundance starts to increase rapidly as a function of radius and the ionizing radiation is not fully shielded by H I. With increasing gas density, the peak and mean luminosities increase, hence the relative effect of Compton pressure on average increases and eventually becomes comparable to the effect of gravity (i.e., Eddington limit). Whereas Figure 4.5 shows that the relative effect of continuum radiation pressure does not increase much with increasing gas density. In addition, the range of variation of radiation pressures during a period of oscillation decreases with increasing
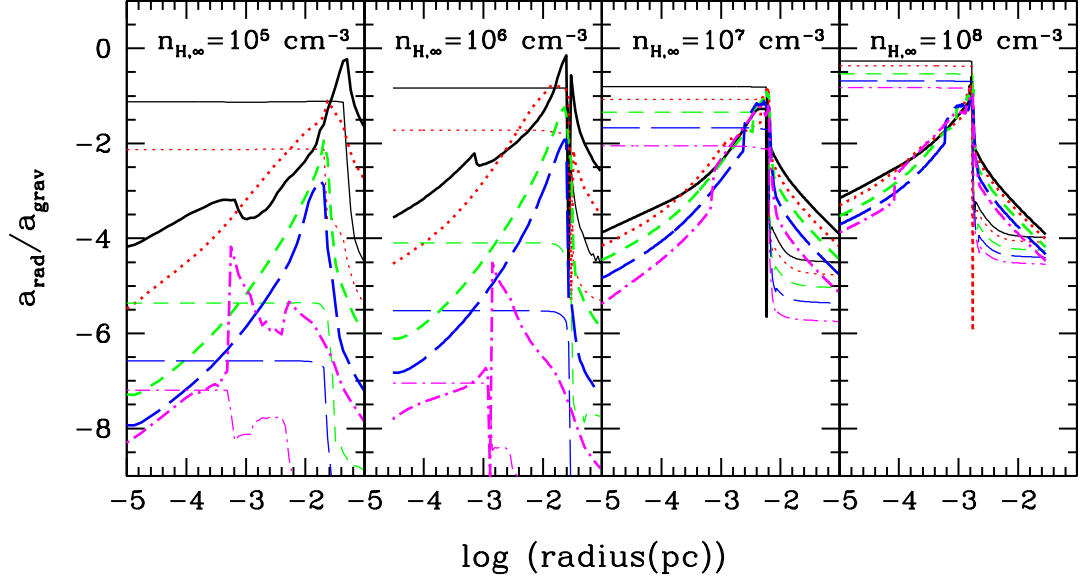
Figure 4.5: Radial profiles of the gas acceleration due to radiation pressures on H I and e^- normalized to the gravitational acceleration of simulations for $n_{H,\infty} = 10^5, 10^6, 10^7,$ and 10^8 cm^{-3} with BH mass $M_{bh} = 100\ M_\odot$, $\eta = 0.1$, and $T_\infty = 10^4$ K. Thick lines refer to radiation pressure on H I, while thin lines show Compton scattering radiation pressure. Different line types show the profiles at different time during the oscillation cycle (e.g., solid lines at the accretion bursts and dot-dashed just before the bursts). Radiation pressure on H I peaks just inside the Strömgren sphere with weak dependence on density. While Compton radiation pressure inside the Strömgren sphere increases on average as a function of density. At 10^7 cm^{-3} the peak values of H I radiation pressure and Compton radiation pressure become comparable and about 10% of gravity. However, at higher densities ($\geq 10^8$ cm^{-3}) radiation pressure on electrons becomes dominant everywhere inside the Strömgren sphere.

density. In other words, at low densities radiation pressures display several magnitudes of variation which are not seen in the high-density regime. As a result, at low densities ($n_{H,\infty} \lesssim 10^6$ cm^{-3}) radiation pressure is significant only near the peaks of luminosity and generally is negligible compared to gravity; whereas at high densities ($n_{H,\infty} \gtrsim 10^7$ cm^{-3}) Compton scattering dominates throughout a period of oscillation reducing the accretion rate to Eddington-limited values. Only at intermediate densities $n_{H,\infty} \simeq 10^7$ cm^{-3}, the magnitude of H I radiation pressure just behind the

Strömgren radius becomes comparable to that by Compton scattering.

The weak dependence of the H I radiation pressure on density and its magnitude with respect to the Compton pressure can be understood analytically. The key point is that the H I radiation pressure is proportional to the value of the neutral fraction $x_{\text{H I}}$ just behind the Strömgren radius R_s and, assuming ionization equilibrium, it is easy to show that $x_{\text{H I}}(R_s) \propto n_{\text{H}}^{-2/3}$. It follows that the pressure on H I is relatively insensitive to variations of n_{H}:

$$P_{\text{Rad}}^{\text{cont}} \propto S_0 x_{\text{H I}}(R_s) \exp\left[-\tau(R_s)\right] \propto n_{\text{H}}^{1/3}, \tag{4.3}$$

where $S_0 \propto n_{\text{H}}$ is the ionizing luminosity, and $\exp\left[-\tau(R_s)\right] = \text{const.}$ The derivation of $x_{\text{H I}}(R_s)$ is as follows. At $R_s = S_0^{1/3} n_{\text{H}}^{-2/3} \alpha_{\text{rec}}^{-1/3}$ the photoionization rate is $\Gamma(R_s) = S_0 \sigma_{\text{H I}}^{\text{eff}}/4\pi R_s^2 \propto n_{\text{H}}^{5/3}$. Assuming photoionization equilibrium $x_{\text{H I}}(R_s)\Gamma(R_s) = n_{\text{H}}\alpha_{\text{rec}}$, we demonstrate that

$$x_{\text{H I}}(R_s) = \frac{n_{\text{H}}\alpha_{\text{rec}}}{\Gamma(R_s)} \propto n_{\text{H}}^{-2/3}. \tag{4.4}$$

4.2   Two Self-regulated Modes of Accretion : Collapsing versus Quasi-steady I-front

One of the most interesting aspects of the radiation-regulated accretion onto BHs is the qualitative change of the period and duty cycle of the luminosity bursts observed in the high-density regime. As argued in Chapter 3 and confirmed by further simulations in this Chapter, the physical reason for this transition is a change of the dominant mechanism depleting the gas inside the Strömgren sphere between two consecutive bursts. In the low-density regime, gas is pushed outward toward the ionization front by a pressure gradient (hereafter, mode-I accretion). At higher-densities gas accretion onto the BH becomes the dominant gas depletion mechanism

(hereafter, mode-II accretion). Incidentally, as discussed below, simulations show that radiation pressure becomes important near the transition from mode-I to mode-II, at least for most of the initial conditions we have simulated. In Chapter 3, we have observed mode-II accretion only for our highest density simulation (for 10^7 cm^{-3} and $M_{\rm bh} = 100\ M_\odot$). In this Chapter, to better understand this regime, we have extended the parameter space to higher densities and higher BH masses. Figure 4.6 shows snapshots of the density (top halves in each panel) and ionization fraction (bottom halves in each panel) for 2D simulations including radiation pressure, for 10^6 cm^{-3} (top panels) and 10^7 cm^{-3} (bottom panels). The snapshots are taken for each simulation at the moment of a burst of the accretion rate (left panels), in-between two bursts (middle panels), and just before a burst (right panels). For ambient density 10^6 cm^{-3}, the Strömgren sphere collapses onto the BH which leads to a strong luminosity burst. On the contrary, the size of Strömgren sphere does not change much during the oscillation period for ambient density 10^7 cm^{-3}. In this latter case, the oscillation of the accretion luminosity is driven by density and pressure waves originating at the I-front, while in the former case, the collapse of the I-front onto the BH leads to a much more intense accretion burst. In Figure 4.7, we compare the accretion rate onto the BH as a function of time for 10^6 cm^{-3} (top panel) and 10^7 cm^{-3} (bottom panel). For 10^6 cm^{-3}, the collapse of I-front leads to strong burst of gas accretion, with $\lambda_{\rm rad,max}$ about $\times 20 \langle \lambda_{\rm rad} \rangle$. Hence, the duty cycle $f_{\rm duty}^{\rm I} \equiv \langle \lambda_{\rm rad} \rangle / \lambda_{\rm rad,max}$ is about 6%. The pressure gradient inside Strömgren sphere supports the gas shell accumulating at the I-front from collapsing until the accretion rate drops 4-5 orders of magnitude compared to the accretion during the burst. However, the Strömgren radius remains remarkably constant before its collapse due to the decline of gas density inside the H II region. In contrast, in the 10^7 cm^{-3} simulation the accretion rate peaks at a few times $\langle \lambda_{\rm rad} \rangle$ before decreasing
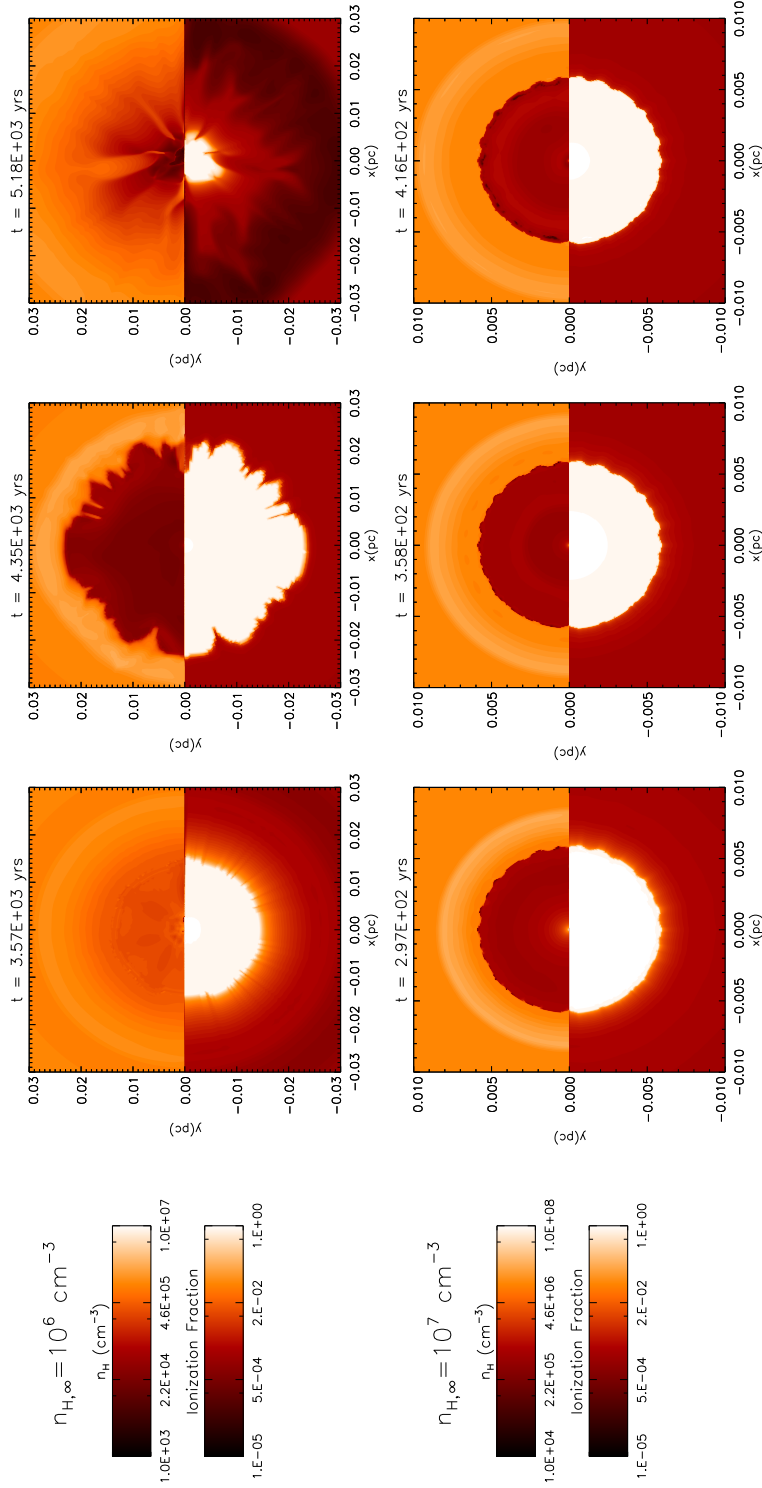
Figure 4.6: Illustration of the two different modes of oscillations found at different ambient densities. The panels show the time evolution of gas density and ionization fraction in 2D simulation for a BH of mass $M_{\rm bh} = 100\ M_{\odot}$, gas density 10^6 cm^{-3} (top panels), and 10^7 cm^{-3} (bottom panels). In each panel, top halves show the density and the bottom halves show the ionization fraction, $x_{\rm H\,II} = n_{\rm H\,II}/n_{\rm H}$. When the density is $n_{\rm H,\infty} \leq n_{\rm H,\infty}^{\rm cr} \simeq 5 \times 10^6$ cm^3, the collapse of ionization front onto the BH leads to a burst of accretion luminosity (mode-I). For densities $n_{\rm H,\infty} > n_{\rm H,\infty}^{\rm cr}$ the size of Strömgren sphere does not change much with time (mode-II). Note the different oscillation modes of the accretion rate and luminosity are driven by the collapse of dense shell (mode-I) and by a density wave (mode-II).

by about 2 orders of magnitude. The duty cycle approaches $f_{\text{duty}}^{\text{II}} \sim 50\%$ for this mode of accretion. As shown in Figures 4.3 and 4.4, simulations that do not include radiation pressure also show a rapid decrease of the period τ_{cycle} and $\lambda_{\text{rad,max}}$ with increasing gas density and BH mass, but the mean accretion rate $\langle \lambda_{\text{rad}} \rangle$ does not. Thus, the reduced value of $\lambda_{\text{rad,max}}/\langle \lambda_{\text{rad}} \rangle \equiv 1/f_{\text{duty}}^{\text{II}}$ explains the longer duty cycle observed for mode-II accretion. A more detailed illustration of the qualitative difference between mode-I and mode-II accretion is shown in Figure 4.8. The figure shows the time evolution of the gas density profile (top panels), the temperature profile (middle panels) and the hydrogen ionization fraction (bottom panels) for the 10^6 cm^{-3} and 10^7 cm^{-3} simulations. Small variations of the density, temperature, and ionization fraction profiles are observed for 10^7 cm^{-3}, while clear collapses of I-front are observed in the evolution of the profiles for 10^6 cm^{-3}. Note that this quasi-stationary profile is not produced by the effects of radiation pressures. The same effect is found for 10^7 cm^{-3} without including radiation pressure effects.

Interestingly, for our fiducial case simulations ($M_{\text{bh}} = 100 \ M_{\odot}$, $T_{\infty} = 10^4$ K, $\eta = 0.1$, and $\alpha = 1.5$), the critical density at which the mean accretion rate becomes Eddington-limited nearly coincides with the critical density for transition from mode-I to mode-II accretion. This explains why the mean accretion rate and the peak accretion rate become Eddington-limited at nearly the same density. Indeed, if while increasing $n_{\text{H},\infty}$, the duty cycle remained at about 6% as in mode-I accretion, the mean accretion rate would not be able to approach the Eddington limit, even though the peak accretion can be mildly super-Eddington. We will show below that the transition to mode-II accretion depends on the free parameters in the problem and may take place at much lower densities than the critical density for Eddington-limited accretion.

The quasi-stationary I-front observed for the 10^7 cm^{-3} simulation is also im-

portant to understand why there exists a clear transition to the Eddington-limited regime with increasing density or BH mass. For mode-I accretion, radiation pressure may become comparable to the gravity near the Strömgren radius, but this effect dominates only for a short time, during the peaks of luminosity. The peak accretion can indeed become moderately super-Eddington for a short time, also because of the broken spherical symmetry of the collapsing shell due to Rayleigh–Taylor instability of the accreting gas. However, for mode-II accretion, the geometry of accretion from large scales is quasi-spherical and radiation pressure effects are significant during the most of the duration of oscillations, hence the accretion rate is Eddington limited.

Figure 4.9 shows the relationship between the period of accretion bursts and the average size of the Strömgren sphere produced by the accreting BH. When the gas depletion inside the H II region is dominated by the outward flow of gas toward the I-front, $\tau_{\text{cycle}}^{\text{I}}$ shows a linear relation with $\langle R_s \rangle$ (solid line). This linear relation is almost identical to the results in Chapter 3, where helium cooling/heating was not included. By increasing the ambient gas density, eventually the gas depletion becomes dominated by accretion onto the BH. In this latter case, assuming that the dimensionless accretion rate $\langle \lambda_{\text{rad}} \rangle$ is constant (a valid assumption in the sub-Eddington regime), τ_{cycle} scales as $\langle R_s \rangle^3$ (dotted line). However, the simulation results at high ambient gas density shown in Figure 4.9 are not well fitted by $\tau_{\text{cycle}} \propto \langle R_s \rangle^3$, and indeed seem to follow a linear relationship $\tau_{\text{cycle}} \propto \langle R_s \rangle$, similar to the low-density one but with an offset. This can be explained because at high densities the accretion rate becomes Eddington-limited soon after the transition to mode-II accretion for which $\tau_{\text{cycle}} \propto \langle R_s \rangle^3$. It follows that the assumption $\langle \lambda_{\text{rad}} \rangle \approx \text{const}$ becomes invalid and instead $\tau_{\text{cycle}}^{\text{II}} \equiv t_{\text{in}} \propto \rho \langle R_s \rangle^3 / \dot{M}_{\text{Edd}}$. In this regime, since the Strömgren radius is $\langle R_s \rangle^3 \propto \eta \dot{M}_{\text{Edd}} / \rho^2$, we get $\rho \propto \dot{M}_{\text{Edd}}^{1/2} \langle R_s \rangle^{-3/2}$ and

$$\tau_{\text{cycle}}^{\text{II}} \propto M_{\text{bh}}^{-1/2} \langle R_s \rangle^{3/2}. \tag{4.5}$$
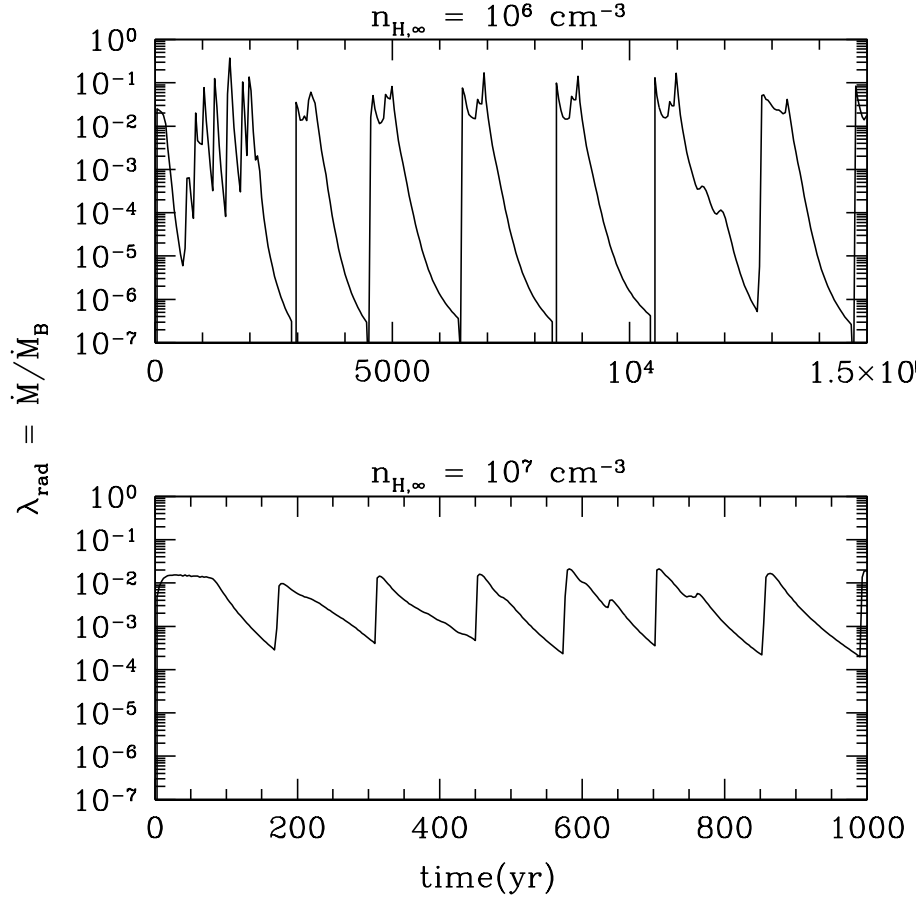
Figure 4.7: Accretion rates as a function of time for 10^6 cm^{-3} and 10^7 cm^{-3} assuming $\eta = 0.1$, $M_{\rm bh} = 100\ M_\odot$, and $T_\infty = 10^4$ K. Different modes of oscillations occur at different density regimes. Mode-I oscillation at 10^6 cm^{-3} shows about 5 orders of magnitude range between peak and the minimum accretion rate, while mode-II oscillation at 10^7 cm^{-3} shows only 2 orders of magnitude range.

As shown by the dashed lines in Figure 4.9, this model is in good agreement with the results of the simulations for different values of $M_{\rm bh}$.

Thus, the small offset in $\tau_{\rm cycle}$ observed in Figure 4.9 when the density is increased, can be understood because $n_{\rm H,\infty}^{\rm cr}$, at which the transition from mode-I to mode-II accretion takes place, is nearly equal to $n_{\rm H,\infty}^{\rm Edd}$, the critical density at which the mean accretion rate becomes Eddington limited. But, in general, the ratio of these critical densities may depend on all the free parameters of the model.

Our analytical model of feedback-regulated feeding of the BH, can help under-
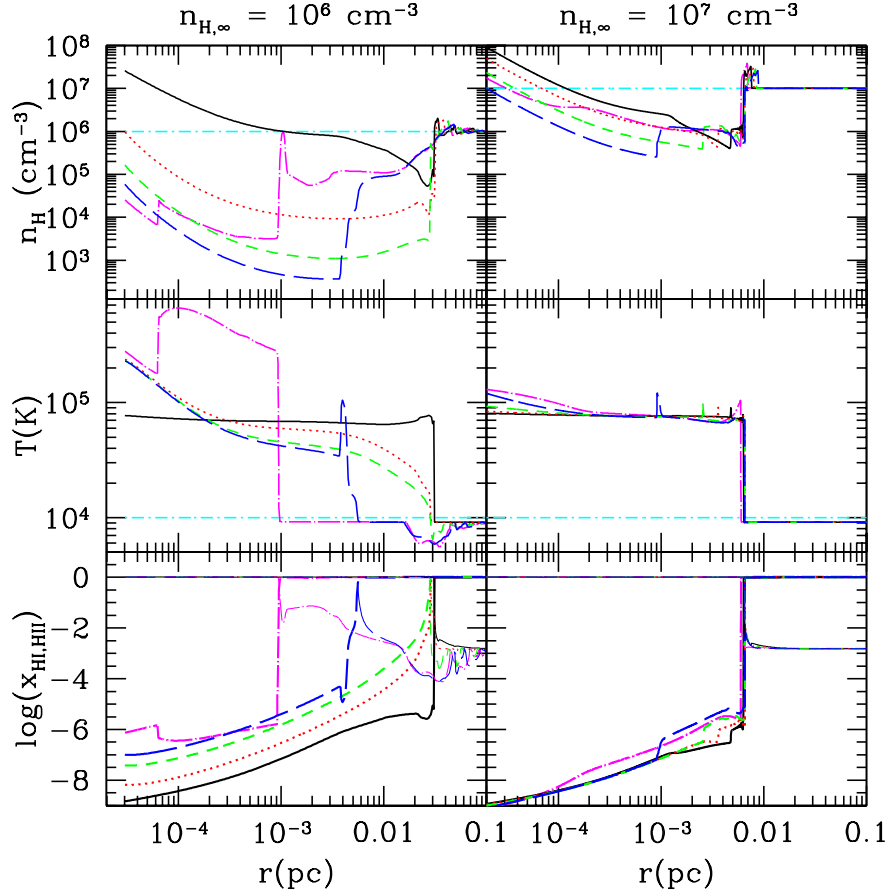
Figure 4.8: Evolution of radial profiles for density (top panel), temperature (middle panel), and neutral/ionization fractions (bottom panel) of the same simulations in the left figure. Note the change of physical properties inside Strömgren sphere during a period of mode-I oscillation (10^6 cm^{-3}), while mild changes are observed for mode-II oscillation (10^7 cm^{-3}).

stand the dependence of the critical density on all the parameter space, not fully covered by the simulations. We found that the cycle period τ_{cycle} is the shortest time between the gas depletion timescales $t_{\mathrm{in}} = M_{\mathrm{H\,II}}/\dot{M}$, where $M_{\mathrm{H\,II}} \sim \rho_{\mathrm{in}}\langle R_s\rangle^3$ is the mass inside the H II region, and $t_{\mathrm{out}} \approx 3\langle R_s\rangle/c_{\mathrm{s,in}}$ (see Chapter 3). Thus, by definition, when the density approaches the critical density we have $t_{\mathrm{in}} \simeq t_{\mathrm{out}}$, but this condition also implies that the mean Strömgren radius approaches the effective accretion radius:

$$\langle R_s\rangle^{\mathrm{cr}} \approx 10 \times r_{\mathrm{acc}}. \tag{4.6}$$
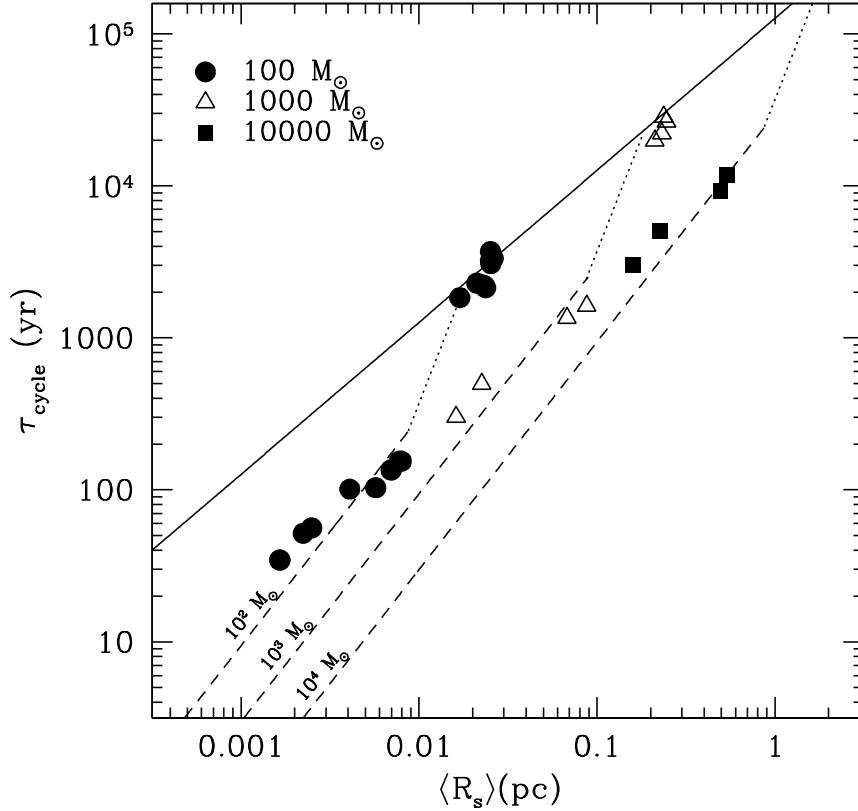
Figure 4.9: Relationship between the period of the accretion bursts, τ_{cycle}, and the time-averaged size of Strömgren radius $\langle R_s \rangle$. τ_{cycle} shows a linear relation with $\langle R_s \rangle$ when the gas depletion inside the Strömgren sphere is dominated by a pressure gradient inside the H II region that push the gas toward the I-front. Instead, $\tau_{\text{cycle}} \propto \langle R_s \rangle^3$ (dotted lines for each M_{bh}) when the gas depletion is dominated by accretion onto the BH. With increasing density of the ambient gas, for each M_{bh}, the transition to mode-II oscillation and the transition to Eddington-limited regime happen at similar densities $n_{\text{H},\infty} = n_{\text{H},\infty}^{\text{cr}} \sim n_{\text{H},\infty}^{\text{Edd}}$. In the Eddington-limited regime τ_{cycle} becomes proportional to $\langle R_s \rangle^{3/2}$ for each BH mass (dashed lines).

Equation (4.6), is derived setting $\dot{M} = \langle \dot{M} \rangle \equiv 4\pi \rho_{\text{in}} c_{\text{s,in}} r_{\text{acc}}^2 \equiv \langle \lambda_{\text{rad}} \rangle \dot{M}_B$ in the relationship for t_{in}. Since in our model we have $\rho_{\text{in}} T_{\text{in}} \simeq \rho_\infty T_\infty$, it follows that $r_{\text{acc}} \approx (T_{\text{in}}/T_\infty)^{1/4} \langle \lambda_{\text{rad}} \rangle^{1/2} r_{\text{b}}$, and $\langle R_s \rangle^{\text{cr}} \simeq 2 T_{\infty,4} T_{\text{in},*}^{-7/4} r_{\text{b}}$, where $T_{\text{in},*} \equiv T_{\text{in}}/6 \times 10^4 \text{ K}$ is the mean temperature at the accretion radius inside the H II region (normalized

61

to the value found for $\alpha = 1.5$). Thus, $\langle R_s \rangle^{\mathrm{cr}}$ and period of the bursts are

$$\langle R_s \rangle^{\mathrm{cr}} \approx (0.01 \text{ pc}) M_{\mathrm{bh},2} T_{\mathrm{in},*}^{-7/4}, \tag{4.7}$$

$$\tau_{\mathrm{cycle}}^{\mathrm{cr}} \approx (1000 \text{ yr}) M_{\mathrm{bh},2} T_{\mathrm{in},*}^{-9/4}. \tag{4.8}$$

Applying naively the analytical expression for $\langle R_s \rangle$ produced by a source of luminosity $L \equiv \eta c^2 \langle \dot{M} \rangle$ in a gas of density ρ_∞ gives $\langle R_s \rangle \propto M^{2/3} n_{\mathrm{H},\infty}^{-1/3} T_\infty^{1/3} \eta^{1/3}$. However, using the simulation data, we find that the mean radius of the Strömgren sphere in the sub-Eddington regime is nearly independent of T_∞, and if $\langle R_s \rangle \sim \langle R_s \rangle^{\mathrm{cr}}$, is also independent of η:

$$\langle R_s \rangle \approx (0.015 \text{ pc}) M_{\mathrm{bh},2}^{2/3} \left(\frac{n_{\mathrm{H},\infty}}{10^6 \text{ cm}^{-3}} \right)^{-1/3} \left(\frac{\bar{E}}{41 \text{ eV}} \right)^{-5/8}, \tag{4.9}$$

where $\bar{E} \equiv L_0/S_0$ is the mean energy of ionizing photons, and we have assumed hydrogen recombination coefficient $\alpha_{\mathrm{rec}} = (4 \times 10^{13} \text{ cm}^3/\text{s}) T_{\mathrm{in},*}^{-1/2}$. In addition, we find that, $\langle R_s \rangle \propto \eta^{1/3}$ as expected for $\langle R_s \rangle \gg \langle R_s \rangle^{\mathrm{cr}}$. The deviation from the naive expectation is not surprising, as the BH luminosity and the density inside the Strömgren sphere are not constant with time. Indeed, although both the maximum and mean luminosities of the BH are $\propto \eta$, the simulations show that the luminosity at the minimum of the cycle, L^{min}, is nearly independent of η. Typically $L^{\mathrm{min}} \ll L$, but when $n_{\mathrm{H},\infty}$ approaches the critical value $L^{\mathrm{min}} \sim L$. Similarly, assuming an effective mean density $(\rho_{\mathrm{in}} \rho_\infty)^{1/2}$ in the Strömgren radius expression would explain the temperature dependence in Equation (4.9).

Finally, setting $\langle R_s \rangle = \langle R_s \rangle^{\mathrm{cr}}$ we derive the critical density

$$n_{\mathrm{H},\infty}^{\mathrm{cr}} \sim (5 \times 10^6 \text{ cm}^{-3}) M_{\mathrm{bh},2}^{-1} T_{\mathrm{in},*}^{7/4} \left(\frac{\bar{E}}{41 \text{ eV}} \right)^{-1}. \tag{4.10}$$

The critical density $n_{\mathrm{H},\infty}^{\mathrm{cr}}$ as well as other scaling relationships in our model depends on $\bar{E} \equiv L/S_0$ and T_{in}, but for a gas of zero metallicity (including helium),
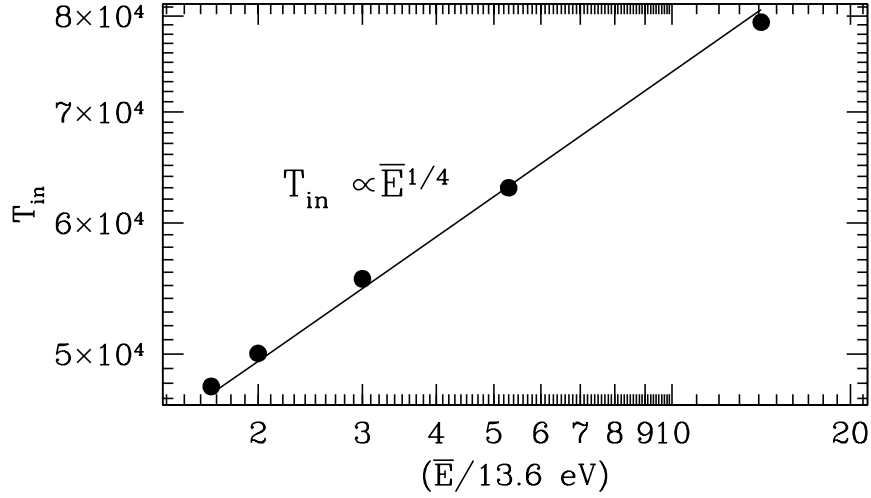
Figure 4.10: Temperature $T_{\rm in}$ at the effective inner Bondi radius, located inside the H II region produced by the accreting BH, as a function of the mean energy of ionizing photons $\bar{E}$ of the spectrum of radiation emitted near the BH by the accretion disk. We have assumed a gas of nearly zero-metallicity and a power-law spectrum $F_\nu \propto \nu^{-\alpha}$.

these quantities are determined only by the spectrum of the radiation. Assuming a power law spectrum with index α is easy to show that

$$
\bar{E} = 13.6 \text{ eV}
\begin{cases}
\alpha/(\alpha - 1) & \text{if } \alpha > 1, \\[2mm]
\ln(h\nu_{\rm max}/13.6 \text{ eV}) & \text{if } \alpha = 1 \\[2mm]
\alpha/(1 - \alpha)(h\nu_{\rm max}/13.6 \text{ eV})^\alpha & \text{if } \alpha < 1.
\end{cases}
\tag{4.11}
$$

We have estimated $h\nu_{\rm max} = 0.2$ keV as the frequency at which the mean free path of the photons equals $\langle R_s \rangle$. The points in Figure 4.10 show $T_{\rm in}$ as a function of $\bar{E}$ for simulations with $\alpha = 0.5, 1, 1.5, 2, 2.5$ taken from Figure 3.10 in Chapter 3. The line shows the fit to the points:

$$
T_{\rm in,*} \approx \left(\frac{\bar{E}}{41 \text{ eV}} \right)^{1/4}.
\tag{4.12}
$$

For our fiducial model, for which $\bar{E} \sim 41$ eV, the value of the critical density is

63

very close to $n_{\mathrm{H},\infty}^{\mathrm{Edd}}$ given in Equation (4.2):

$$\frac{n_{\mathrm{H},\infty}^{\mathrm{cr}}}{n_{\mathrm{H},\infty}^{\mathrm{Edd}}} \approx \eta_{-1} T_{\infty,4} \left(\frac{\bar{E}}{41 \text{ eV}}\right)^{-9/16}. \tag{4.13}$$

From an inspection of Equation (4.13) is evident that the only cases in which $n_{\mathrm{H},\infty}^{\mathrm{cr}}$ can be larger than $n_{\mathrm{H},\infty}^{\mathrm{Edd}}$ are assuming the largest realistic values of unity for $T_{\infty,4}$ and η_{-1}, and assuming a spectrum of radiation from the BH softer than $\alpha = 1.5$ that would reduce $\bar{E}$ with respect to the fiducial value. Vice versa a hard spectrum, low radiative efficiency and accretion from a gas colder than 10^4 K would decrease the ratio $n_{\mathrm{H},\infty}^{\mathrm{cr}}/n_{\mathrm{H},\infty}^{\mathrm{Edd}}$ below unity, making mode-II accretion sub-Eddington for a wider range of densities. For these cases the period of the cycle could become very short with increasing density as $\tau_{\mathrm{cycle}} \propto \langle R_s \rangle^3 \propto n_{\mathrm{H},\infty}^{-1}$.

4.3 Effect of Non-zero Angular Momentum of Gas

As discussed in Chapter 3, the introduction of small angular momentum in the flow, which is realistic in most astrophysical problems, can modify the time-dependent behavior of accretion rate presented in this work. Angular momentum of gas leads to the formation of an accretion disk near the Schwartzshild radius of a BH. This disk is not resolved in our simulations. Thus, the accreted gas may experience a time delay before it is converted to radiation. Here, we test how the introduction of time delay would affect the feedback loops of accretion.

As mentioned in Section 2, it is important to estimate physically motivated time delays. Here, we explore the time delay of 1–300 times $t_{\mathrm{ff}}(r_{\mathrm{min}})$ which is large enough with an assumption of α-disk model. On the other hand, no matter how long is the time delay, what really matters is how the time delay compares to the oscillation period, which depends mainly on the gas density for a fixed mass of BH. We investigate this issue in the low (10^5 cm^{-3}) and high density (10^7 cm^{-3}) regimes
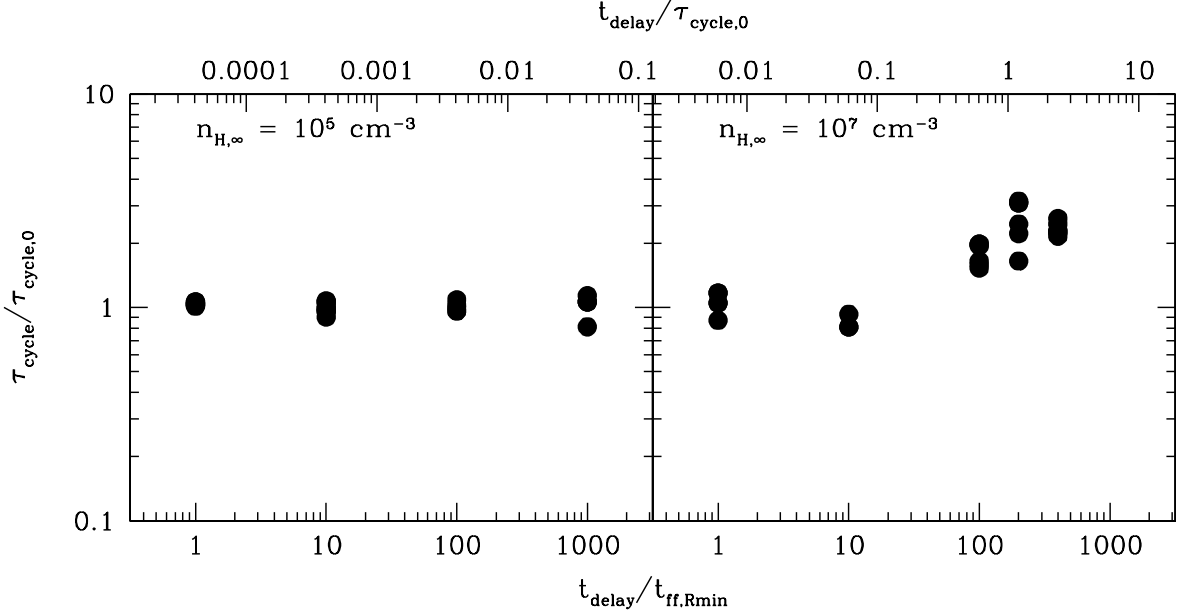
Figure 4.11: Dependence of the period between bursts τ_{cycle} on the time delay between the accretion rate at r_{min} and the BH output luminosity. The time delay is produced by the presence of the accretion disk that is unresolved in our simulations. The two panels show τ_{cycle} in units of $\tau_{\text{cycle},0} \equiv \tau_{\text{cycle}}(t_{\text{delay}} = 0)$ as a function of t_{delay} for 10^5 cm^{-3} (left panel) and 10^7 cm^{-3} (right panel). The bottom axis shows t_{delay} in units of the free-fall time at r_{min} and the top axis in units of $\tau_{\text{cycle},0}$. The introduction of a time delay does not change τ_{cycle} when the gas density is 10^5 cm^{-3}, while τ_{cycle} increases by approximately the amount of time delay introduced for 10^7 cm^{-3}. In this density regime, the largest time delays introduced are comparable to the oscillation period $\tau_{\text{cycle},0}$. In both cases, the oscillatory behavior of the accretion luminosity does not disappear.

where the oscillation pattern and the periods are different. At low densities a time delay of a few hundred free-fall times is much smaller compared to the oscillation period, whereas at high densities the maximum time delay that we have tested is comparable to the oscillation period. In the left panel of Figure 4.11 which shows the result for 10^5 cm^{-3}, τ_{cycle} does not increase at all as a function of time delay since the introduced time delay is much smaller than the original oscillation period. In the right panel of Figure 4.11 for 10^7 cm^{-3}, the maximum time delay that we introduce is comparable to the original oscillation period, and we see that τ_{cycle}

increase approximately by the amount of time delay. In both cases, we still observe oscillations. Thus, only in the case of accretion from a high-density gas which produces shorter oscillation period, and for an accretion disk with $R_{\rm disk} \sim r_{\rm min}$, the time delay may have an important effect on the accretion rate.

Indeed, the accretion disk may not only introduce a time delay but also smooth out the accretion rate on a timescale of the order of the viscous timescale. In this case for cases in which the disk is large ($R_{\rm disk} \sim r_{\rm min}$) and $\tau_{\rm cycle}$ is short (i.e., for mode-II accretion), the disk may further smooth out or completely erase the periodic low-amplitude oscillations in the accretion rate from large scales.

Chapter 5

Bondi-Hoyle-Lyttleton Accretion with Radiative Feedback

Abstract: In this chapter, we study the growth rate and luminosity of BHs in motion with respect to their surrounding medium. We run a large set of two-dimensional axis-symmetric simulations to explore a large parameter space of initial conditions and formulate an analytical model for the accretion. Contrary to the case without radiation feedback, we find that the accretion rate increases with increasing BH velocity v reaching a maximum value at $v = 2c_{\mathrm{s,in}}$, where $c_{\mathrm{s,in}}$ is the sound speed of the photo-ionized gas, before decreasing as v^{-3}. The increase of the accretion rate with v is produced by the formation of a D-type (density) ionization front (I-front) preceded by a standing bow-shock that reduces the downstream gas velocity to nearly sub-sonic values. Since the ionization front is beyond the classical Bondi radius for the hot ionized gas, in the BH frame of reference the accretion flow is similar to the stationary case. Interestingly, there is a range of densities and velocities in which the dense shell downstream of the bow-shock is unstable; its central part is destroyed and reformed intermittingly, producing a periodic accretion

rate with peak values about 10 times the mean. This effect can significantly increase the detectability of accreting intermediate mass BHs from the interstellar medium (ISM) in nearby galaxies. For $v > 2c_{\rm s,in}$ the central part of the bow-shock is not able to regenerate, the I-front becomes R-type and the accretion rate approaches the classical Bondi-Hoyle-Lyttleton solution. We find that the maximum accretion rate for a moving BH is larger than that of a stationary BH of the same mass, accreting from the same medium if the medium temperature is $T < 10^4$ K. This result could have an important impact on our understanding of the growth of seed BHs in the multi-phase medium of the first galaxies and for building and early X-ray background that may affect the formation of the first galaxies and the reionization process.

5.1 Accretion Rate as a Function of Mach Number

Classical Bondi-Hoyle-Lyttleton accretion predicts monotonic decrease of accretion rate with increasing velocity of ambient gas as in Equation (1.1), however our simulations of moving BHs with radiative feedback show totally different dependence of accretion rate on Mach number.

Figure 5.1 shows time evolution of accretion rate for different Mach numbers $\mathcal{M} = 1, 2, 4, 8,$ and 10 for gas density $n_{\rm H,\infty} = 10^3$ cm^{-3}. Most simulations except the one with $\mathcal{M} = 4$ show steady accretion rates after an initial transient phase. The time duration of the transient phase is proportional to the crossing time scale $\tau_{\rm cr}$, and thus inversely proportional to the Mach number.

The mean dimensionless accretion rate $\langle \lambda_{\rm rad} \rangle$ is measured when the accretion reaches a steady state, while the time-averaged accretion rate is taken for the non-

steady cases such as the $\mathcal{M} = 4$ case. As found in Chapter 3, at low gas densities, i.e. $n_{\mathrm{H},\infty} \lesssim 10^5$ cm^{-3} for simulations with $M_{\mathrm{bh}} = 100\ M_{\odot}$, $\langle \lambda_{\mathrm{rad}} \rangle$ is proportional to square-root of density ($\langle \lambda_{\mathrm{rad}} \rangle \propto n_{\mathrm{H},\infty}^{1/2}$). Figure 5.2 shows that after correcting $\langle \lambda_{\mathrm{rad}} \rangle$ for the aforementioned density dependence found for stationary BH, most simulations with different gas densities (large symbols for $\eta = 0.1$ and gas densities $n_{\mathrm{H},\infty} = 10^2$–$10^6$ cm^{-3}) and radiative efficiency (small pentagons for a simulation with $\eta = 0.03$ and $n_{\mathrm{H},\infty} = 10^5$ cm^{-3}) show the same functional form for the accretion rate.

The quasi-periodic oscillation of the accretion rate for stationary BHs found in Chapter 3 and 4, is still observed for low Mach number simulations ($\mathcal{M} \lesssim 0.5$), which maintain the characters of spherically symmetric accretion. This implies that introducing small systematic subsonic velocity to spherically symmetric accretion does not significantly alter the qualitative description of the accretion discussed in Chapters 3 and 4. However, we find that average accretion rate $\langle \lambda_{\mathrm{rad}} \rangle$ decreases steeply as a function of Mach number, and $\langle \lambda_{\mathrm{rad}} \rangle$ at $\mathcal{M} \sim 1$ is roughly an order of magnitude smaller than for the non-moving BH when all the other parameters are held fixed. This is qualitatively consistent with the prediction of Bondi-Hoyle-Lyttleton accretion, in which the accretion cross section decreases as v increases.

The spherically symmetric accretion model fails with increasing Mach number ($\mathcal{M} \gtrsim 1$), and the shape of the H II region makes a transition to a well-defined axis-symmetric geometry. The shape of the H II region becomes elongated along the direction of the gas flow in the downstream direction, while a bow-shaped dense shell develops in front of the H II region in the upstream direction, and significantly affects the velocity field of gas inflow. Steady state accretion can be achieved in this range of Mach numbers since gas can be continuously supplied to the BH without interruption. Surprisingly, for $\mathcal{M} > 1$, $\langle \lambda_{\mathrm{rad}} \rangle$ increases as a function of Mach num-

ber which is opposite to the classical Bondi-Hoyle-Lyttleton description. A Mach number of $\mathcal{M} \sim 1$ is roughly the turning point where $\langle \lambda_{\mathrm{rad}} \rangle$ has a minimum, while at $\mathcal{M} \sim \mathcal{M}_{\mathrm{cr}}$, $\langle \lambda_{\mathrm{rad}} \rangle$ reaches peak values for all simulations with different parameters. An instability of the dense shell that leads to bursts of accretion rate is observed in some simulations for this Mach number range. This result will be discussed in Section 5.3. At higher Mach numbers ($\mathcal{M} > \mathcal{M}_{\mathrm{cr}}$), a steady state solution is achieved once again since the dense shell does not form due to the high velocity of the gas inflow (the I-front becomes R-type). For $\mathcal{M} > \mathcal{M}_{\mathrm{cr}}$, $\langle \lambda_{\mathrm{rad}} \rangle$ monotonically decreases as a function of Mach number and converges to the Bondi-Hoyle-Lyttleton solution shown as a dashed line in Figure 5.2.

5.2 Isothermal Shock and D-type I-Front

5.2.1 Structure of Elongated Strömgren sphere

For Mach numbers $1 < \mathcal{M} < \mathcal{M}_{\mathrm{cr}}$, a dense bow shock forms in front of the H II region in the upstream direction, followed by the I-front (see Figure 5.3). Most of the gas inflow propagates through the bow shock without changing direction, while a small fraction of the gas inflow in the outer parts of the bow-shock is re-directed farther from the axis of symmetry. The formation of a bow shock in the upstream direction changes the gas density and velocity behind the shock, while the gas temperature remains relatively unaffected (isothermal shock). Note that the H II region has a cometary shape, with overall length increasing linearly with increasing Mach number. The size of the H II region in the upstream direction is not sensitive to the Mach number, while in the downstream direction shows a linear relationship to the Mach number as shown in Figure 5.3. The upper panels in Figure 5.3 show the changes in the density structure and the H II region shape for $\mathcal{M} = 1, 2,$ and 4
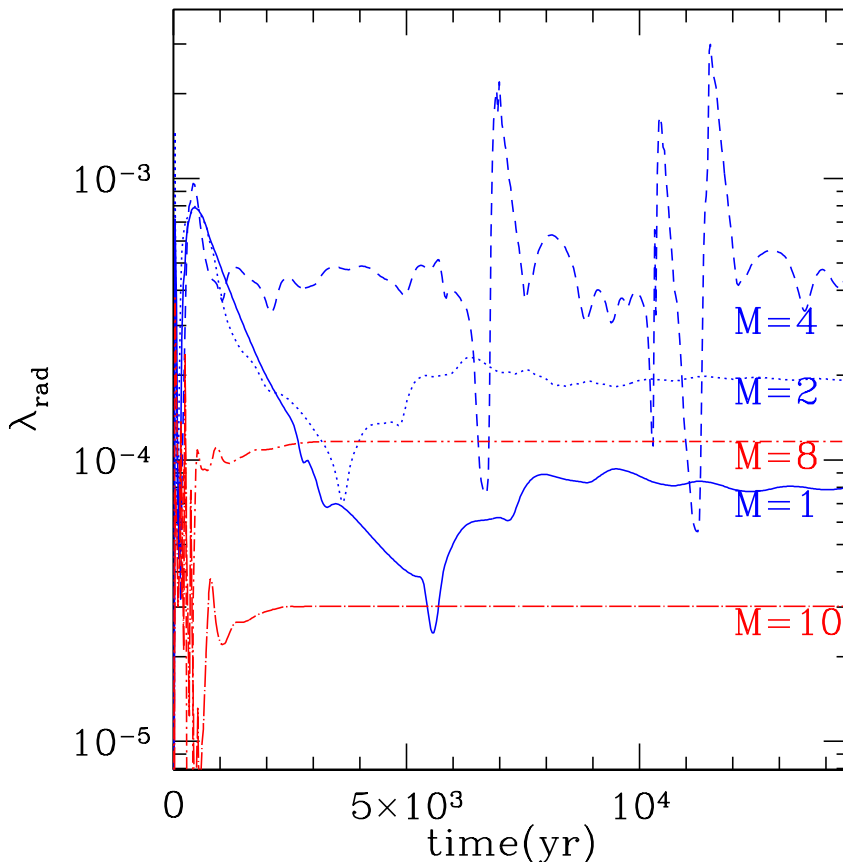
Figure 5.1: Accretion rate as a function of time for a BH with $M_{\rm bh} = 100\ M_\odot$, $n_{\rm H,\infty} = 10^3$ cm^{-3}, and $T_{\rm in} = 10^4$ K. Different lines show simulations for BH moving at Mach number 1,2,4,8 and 10 (see labels under each line). Early phase of the simulations shows oscillatory behavior which becomes steady later being dominated by the motion of the gas as the simulations evolve. Simulations with bigger Mach number show smaller effect of early phase oscillation which is extremely weak in simulation with $\mathcal{M} = 8, 10$. Average accretion rate as a function of Mach number increases for Mach number from 1 to 4 and decreases for higher Mach numbers. Quasi-periodic burst of accretion is seen for the simulation with $\mathcal{M} = 4$.

respectively. The lower panels show the vector fields over the gas density for each simulation. In the bottom panels, we use a logarithmic scale for the radial direction to better show the motion of gas in the vicinity of the BH.

For $\mathcal{M} = 1$ the size of the H II region in the downstream direction is roughly ~ 4 times its length in the upstream direction. The density structure in the downstream
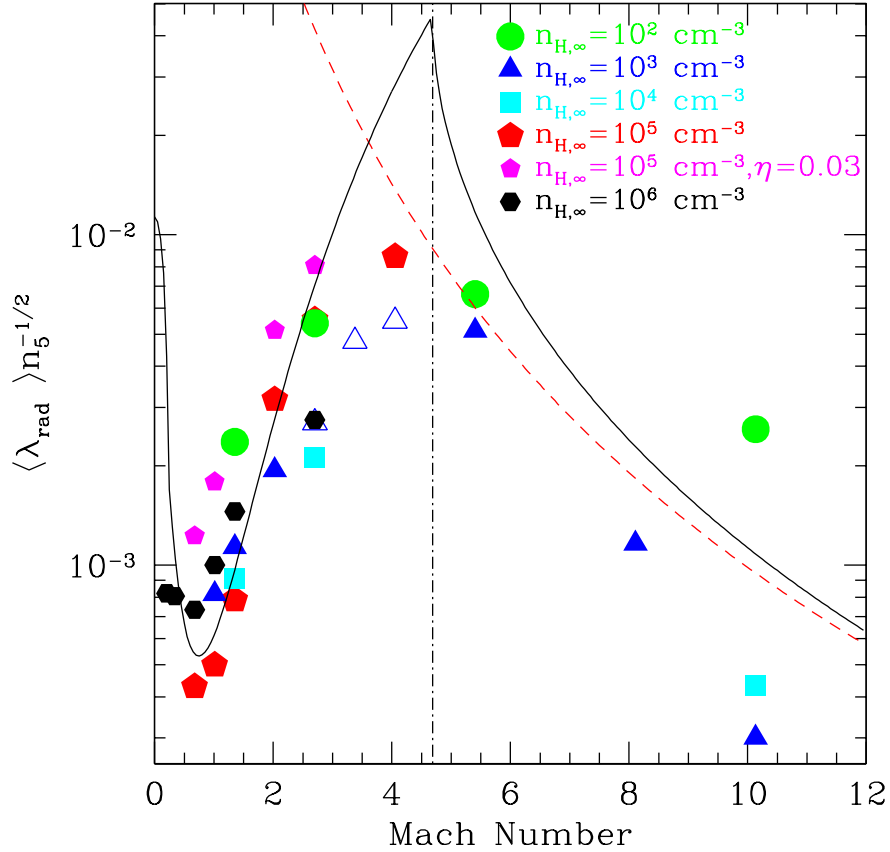
Figure 5.2: Accretion rate as a function of Mach number. Classical Bondi-Hoyle accretion predicts monotonic decrease of accretion rate as $\langle \lambda_{\rm rad} \rangle \propto (1 + \mathcal{M}^2)^{-1.5}$ (dashed line). However, our simulations show that $\langle \lambda_{\rm rad} \rangle$ decreases with $\mathcal{M}$ for low Mach number $\mathcal{M} < 1$ with minimum $\langle \lambda_{\rm rad} \rangle$ at $\mathcal{M} \sim 1$, increases for $1 < \mathcal{M} \lesssim \mathcal{M}_{\rm cr}$, and decreases again for $\mathcal{M} > \mathcal{M}_{\rm cr}$. Solid line shows our model using isothermal ($\gamma = 1$) shock and D-type I-front jump condition for the dense shell in the upstream direction. Density dependence of the mean accretion rate ($\langle \lambda_{\rm rad} \rangle \propto n_{\rm H,\infty}^{1/2}$ from Paper I) is applied for comparison between simulations with various densities ($n_{\rm H,\infty} = 10^2 - 10^6$ cm^{-3}). Dot-dashed line indicates the critical Mach number $\mathcal{M}_{\rm cr}$ where the $\langle \lambda_{\rm rad} \rangle$ peaks.

direction is very complex as shown in Figure 5.3. The re-directed gas streams form high density regions and shocks. However, since most of the gas downstream of the BH is not accreted onto the BH, we will focus on understanding the upstream structures. The shape of the H II region will be discussed in greater detail in Section 5.2.3.
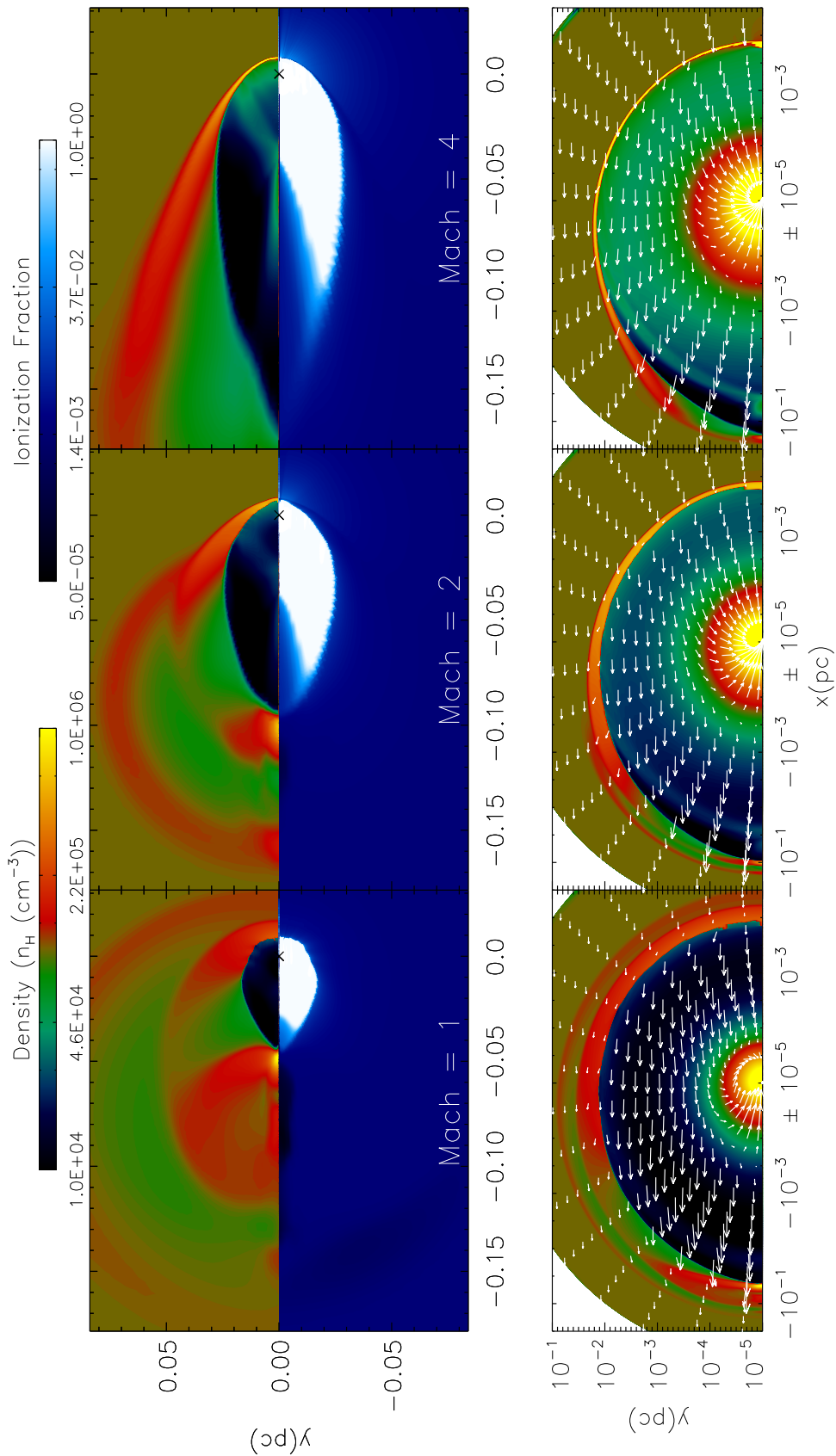
Figure 5.3: Density and ionization fraction for simulations of a BH of mass $M_{\rm bh} = 100~M_\odot$, gas density $n_{\rm H,\infty} = 10^5~{\rm cm}^{-3}$, and temperature $T_\infty = 10^4$ K moving at $\mathcal{M} = 1, 2, and 4$ (from left to right). Each panel shows large scale view of the Strömgren sphere in cometary shape and the dense shell in the upstream direction for each simulation with different Mach numbers. The size of the Strömgren sphere in the downstream increases roughly linearly with increasing Mach number. However, the size of the Strömgren in the upstream direction remains constant as a function of Mach number. With increasing Mach number, the density of the shell in the upstream direction increases $((n_{\rm H,shell}/n_{\rm H,\infty}) \propto \mathcal{M}^2)$ and the density behind the dense shell also increases $n_{\rm H,in}/n_{\rm H,\infty} \propto (1 + \mathcal{M})^2$ for $1 < \mathcal{M} < \mathcal{M}_{\rm cr}$.

73
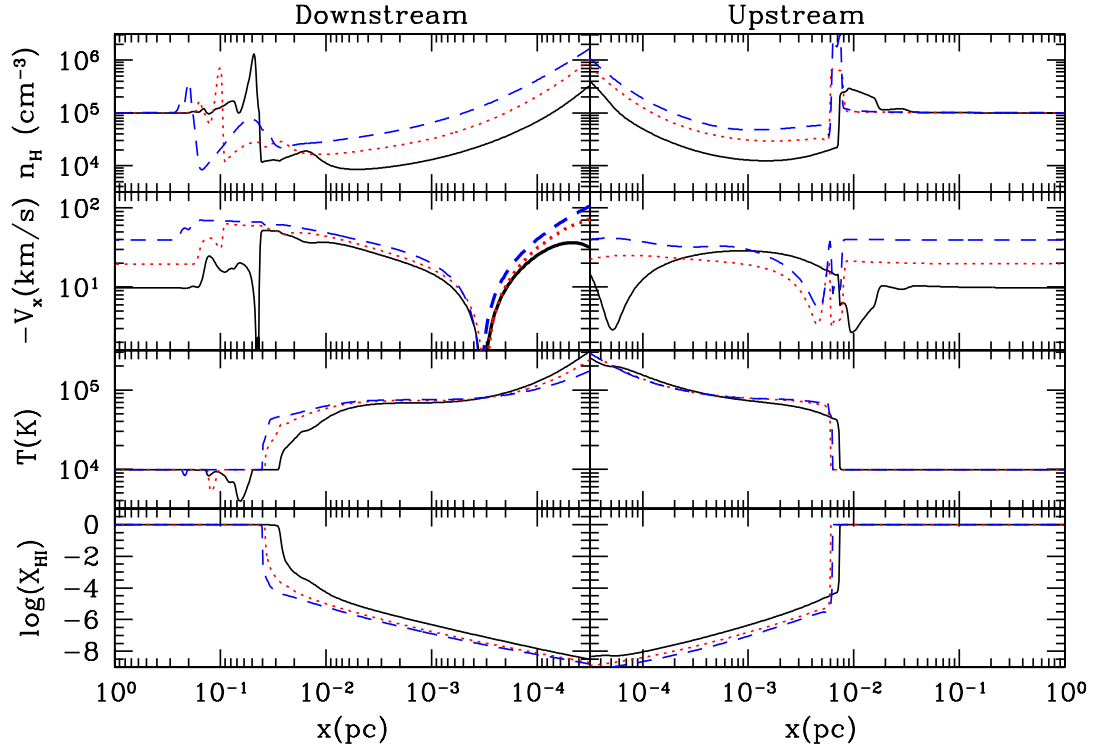
Figure 5.4: Density, velocity, temperature, and H I abundance (from top to bottom) profiles along X-axis for simulations in Figure 5.3 for $\mathcal{M} = 1$ (solid lines), 2 (dotted), and 4 (dashed). Left panels (note that small scale is located on the right side) show profiles of downstream while right panels show upstream profiles.

5.2.2 Isothermal Density Shock and D-type I-front

In our simulations, we observe that the post-shock density and velocity of the gas changes as a function of Mach number, while the temperature remains constant (see density and temperature profiles in Figure 3.2). This allows us to model the shock using isothermal ($\gamma = 1$) shock jump condition. The ratio between the densities at infinity and behind the isothermal shock is,

$$\frac{\rho_{\mathrm{sh}}}{\rho_\infty} = \frac{v_\infty}{v_{\mathrm{sh}}} = \mathcal{M}^2. \tag{5.1}$$
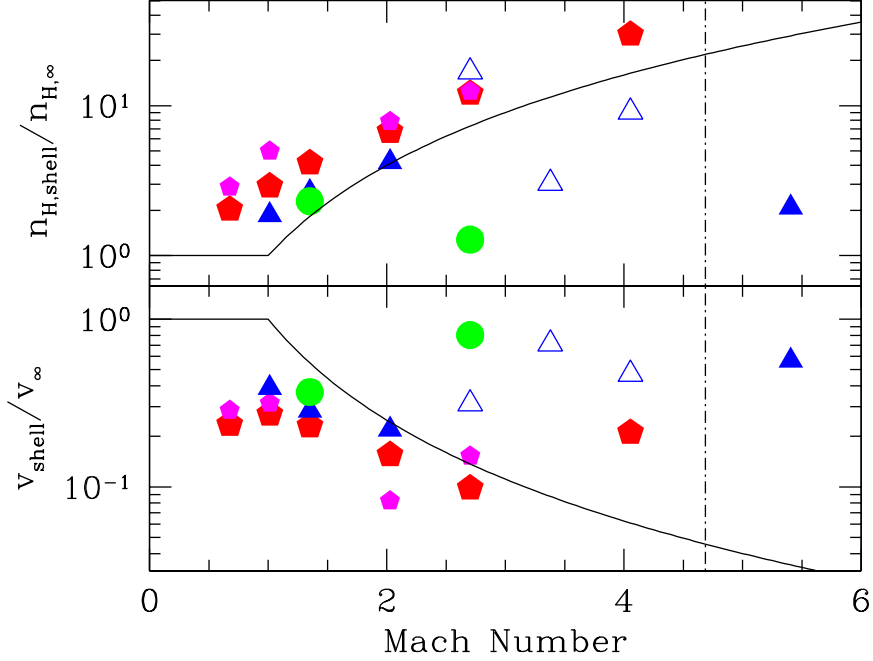
Figure 5.5: Density and velocity of gas in the dense shell in the upstream direction. Isothermal shock jump condition ($n_{H,shell} \propto \mathcal{M}^2$) explains the density in the shell.

Since the density of the shell is approximately proportional to square of Mach number, the post-shock velocity in the dense shell is inversely proportional to the square of the Mach number, assuming that the mass flux ρv is conserved. The left panels in Figure 5.6 show the ratios between density/velocity of gas at infinity and inside the dense shell. The lines show the model for an isothermal shock. Applying the isothermal jump conditions, the Mach number in the shell, $\mathcal{M}_{sh}$, can be expressed as

$$\mathcal{M}_{sh} \equiv \frac{v_{sh}}{c_{s,sh}} = \frac{v_\infty}{c_{s,\infty}\mathcal{M}^2} = \mathcal{M}^{-1} < 1. \tag{5.2}$$

Across the I-front, the density ratio between the gas in the shell and in the H II region can be estimated by solving the mass and momentum conservation conditions ($\rho_{in}v_{in} = \rho_{sh}v_{sh} = J\mu$ with $\mu = 1.27m_H$):

$$\frac{\rho_{in}}{\rho_{sh}} = \frac{(1 + \mathcal{M}_{sh}^2) \pm \sqrt{(1 + \mathcal{M}_{sh}^2)^2 - 4\mathcal{M}_{sh}^2\Delta_T}}{2\Delta_T}, \tag{5.3}$$

where $\Delta_T \equiv T_{in}/T_\infty$. Due to the condition for the density ratio in Equation (5.3)

75
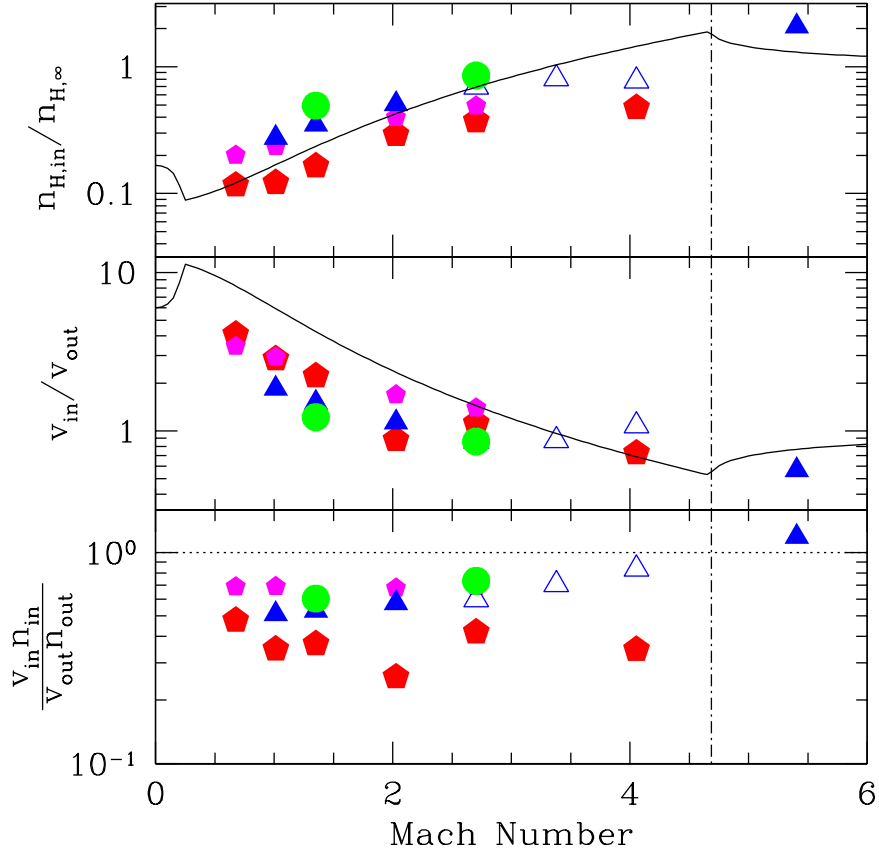
Figure 5.6: Density and velocity of gas inside the Strömgren sphere. D-type I-front explains the change of the density inside the Strömgren sphere.

to have real positive values, the Mach number must be less than $\mathcal{M}_{\mathrm{D,sh}}$ where D stands for *dense* gas, or greater than $\mathcal{M}_{\mathrm{R,sh}}$ where R refers to *rarefied* gas. D- and R-critical Mach numbers of the shell are respectively:

$$\mathcal{M}_{\mathrm{D,sh}} = \sqrt{\Delta_T} \left(1 - \sqrt{1 - 1/\Delta_T}\right) \xrightarrow[\Delta_T \gg 1]{} \frac{1}{2\sqrt{\Delta_T}} \tag{5.4}$$

$$\mathcal{M}_{\mathrm{R,sh}} = \sqrt{\Delta_T} \left(1 + \sqrt{1 - 1/\Delta_T}\right) \xrightarrow[\Delta_T \gg 1]{} 2\sqrt{\Delta_T}. \tag{5.5}$$

Also, $\mathcal{M}_{\mathrm{D,sh}}\mathcal{M}_{\mathrm{R,sh}} = 1$, thus $\mathcal{M}_{\mathrm{D}} \equiv \mathcal{M}_{\mathrm{D,sh}}^{-1} = \mathcal{M}_{\mathrm{R,sh}}$.

By combining Equation (5.1) and (5.3) we get

$$\Delta_\rho \quad \equiv \quad \frac{\rho_{\mathrm{in}}}{\rho_\infty} = \frac{\rho_{\mathrm{in}}}{\rho_{\mathrm{sh}}} \frac{\rho_{\mathrm{sh}}}{\rho_\infty} \tag{5.6}$$

$$= \quad \frac{(\mathcal{M}^2 + 1) \pm \sqrt{(\mathcal{M}^2 + 1)^2 - 4\mathcal{M}^2 \Delta_T}}{2\Delta_T}, \tag{5.7}$$

76

that is identical to Equation (5.3) after replacing $\mathcal{M}_{\text{sh}}$ with $\mathcal{M}$. Similarly, the velocity ratio between H I and H II region is expressed as $v_{\text{in}}/v_\infty = \Delta_\rho^{-1}$. The R-critical Mach numbers $\mathcal{M}_{\text{R,sh}}$ in Equation (5.5) and $\mathcal{M}_{\text{R}}$ the corresponding critical value for $\mathcal{M}$ in Equation (5.7) are identical since they do not form isothermal shock at this Mach number. Note that D- and R-critical Mach numbers, $\mathcal{M}_{\text{D}}$ and $\mathcal{M}_{\text{R}}$, are exactly the same:

$$\mathcal{M}_{\text{cr}} = \sqrt{\Delta_T} + \sqrt{\Delta_T - 1} \sim 2\sqrt{\Delta_T}, \tag{5.8}$$

where $\mathcal{M}_{\text{cr}} \sim 4.7$ for $\Delta_T \simeq 6$ (i.e. $T_{\text{in}} = 6 \times 10^4$ K). Thus, we get D-type I-fronts for $\mathcal{M} < \mathcal{M}_{\text{cr}}$ while a transition to R-type occurs at $\mathcal{M} \gtrsim \mathcal{M}_{\text{cr}}$.

Right panels of Figure 5.6 show the density and velocity ratios between the gas at infinity and inside the H II region for simulations with different gas density and radiative efficiency as a function of Mach number. We select densities within the H II region where the density profiles has a minimum behind the I-front, while velocities are read at the same radius. Simulations show a good match with our model shown as solid lines which is a combination of isothermal shock and D-type I-fronts jump condition. For a plane parallel I-front and shock, the mass flux of the gas is conserved: $\rho_{\text{in}} v_{\text{in}} = \rho_\infty v_\infty$. However, due to the velocity component of the gas perpendicular to the direction of the BH motion, values of $\rho_{\text{in}} v_{\text{in}}/(\rho_\infty v_\infty) < 1$ are observed in the right bottom panel of Figure 5.6. The mean dimensionless accretion rate $\langle \lambda_{\text{rad}} \rangle$ can be estimated using the Bondi formula inside the H II region, and the density and velocity inside the Strömgren sphere can be modeled combining isothermal shock and D-type I-front jump condition. Since the accretion rate inside the H II region is $\dot{M} \propto M_{\text{bh}}^2 \rho_{\text{in}} c_{\text{s,in}}^{-3} (1 + \mathcal{M}_{\text{in}}^2)^{3/2}$, we can normalize the accretion rate
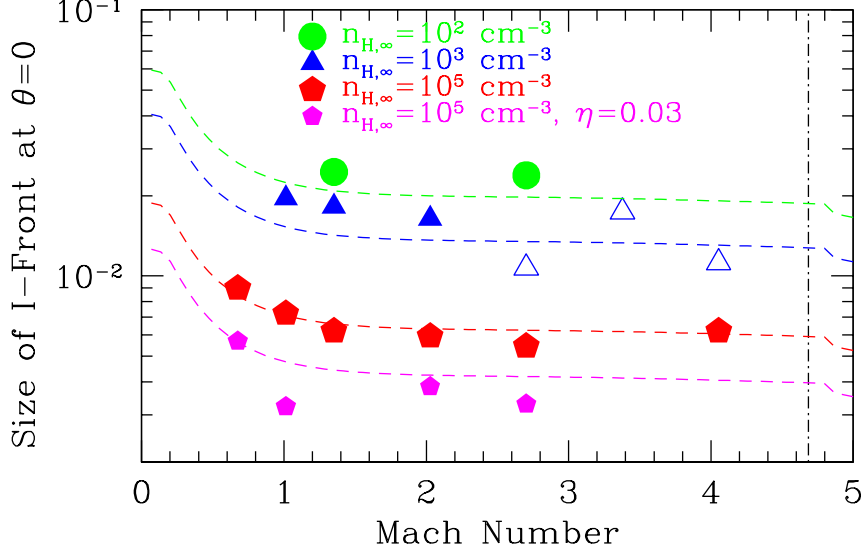
Figure 5.7: Size of Strömgren sphere in the upstream direction ($\theta = 0$) $R_{\mathrm{s},0}$ as a function of $\mathcal{M}$. Since the recombination time scale τ_{rec}, $R_{\mathrm{s},0}$ is not sensitive to the velocity of the flow. Also, it is not sensitive to the density of the ambient medium $R_{\mathrm{s},0} \propto n_{\mathrm{H},\infty}^{-1/6}$. Simulation results show a good match with the model.

by $\dot{M}_{\mathrm{B}} \propto M_{\mathrm{bh}}^2 \rho_\infty c_{\mathrm{s},\infty}^{-3}$ such that

$$\langle \lambda_{\mathrm{rad}} \rangle \equiv \frac{\dot{M}}{\dot{M}_{\mathrm{B}}} \;=\; \frac{\rho_{\mathrm{in}}}{\rho_\infty} \left(\frac{c_{\mathrm{s},\infty}}{c_{\mathrm{s,in}}} \right)^3 \frac{1}{(1 + \mathcal{M}_{\mathrm{in}}^2)^{3/2}} \tag{5.9}$$

$$\;=\; \Delta_\rho \Delta_T^{-3/2} \frac{1}{(1 + \Delta_\rho^{-2} \Delta_T^{-1} \mathcal{M}^2)^{3/2}}, \tag{5.10}$$

where $\mathcal{M}_{\mathrm{in}} = v_{\mathrm{in}}/c_{\mathrm{in}} = \Delta_\rho^{-1} \Delta_T^{-1/2} \mathcal{M} \simeq 1$. The solid line in Figure 5.2 shows the model which displays a good agreement with simulations except simulations exhibit a lower accretion rates around the critical Mach number $\mathcal{M}_{\mathrm{cr}}$.

5.2.3 Size of Strömgren Sphere in the Up/Downstream Direction

The gas inflow in the direction of the polar axis $\theta = 0$ (upstream) can be approximated by 1D flow with the H II region being supplied with neutral gas with constant velocity v_∞. This enables us to predict the size of the I-front at $\theta = 0$. Suppose

that the total number of ionizing photons from BHs equals the number of H recombinations inside a radius $\langle R_s \rangle$, where neutral gas flow with density n and velocity v_∞ is supplied from a neutral gas reservoir:

$$N_{\rm ion} = \frac{4\pi}{3} \langle R_s \rangle_{\theta=0}^3 \alpha_{\rm rec} n_e^2 + 4\pi \langle R_s \rangle_{\theta=0}^2 n v_\infty, \tag{5.11}$$

where $N_{\rm ion}$ is the number of emitted ionizing photons, being directly related to the luminosity of the BHs (which is a function of Mach number). When the magnitudes of the two terms on the right side of the Equation (5.11) are compared, at $\theta = 0$ the first term is dominant over the second term due to the motion of the BH. Inside the Strömgren sphere, most of the H/He is ionized ($x_e \sim 1$), we express the gas number density inside the H II region in terms of $n_{\rm H,\infty}$ such as

$$n_e \sim x_e n_{\rm H,in} = \frac{1 + \mathcal{M}^2}{2\Delta_T} n_{\rm H,\infty}, \tag{5.12}$$

which is valid for $1 < \mathcal{M} < \mathcal{M}_{\rm cr}$ and can be plugged into Equation (5.11). Since $\langle \lambda_{\rm rad} \rangle \propto n_{\rm H,\infty}^{0.5}$ for $n_{\rm H,\infty} \lesssim 10^5$ cm^{-3} and $M_{\rm bh} = 100\ M_\odot$, we derive the dependence of the average size of H II region in the upstream direction as

$$\langle R_s \rangle_{\theta=0} \propto \eta^{1/3} n_{\rm H,\infty}^{-1/6}. \tag{5.13}$$

Figure 5.7 shows the size of Strömgren sphere at $\theta = 0$ as a function of Mach number for various densities ($n_{\rm H,\infty} = 10^2 - 10^6$ cm^{-3}) and radiative efficiency ($\eta = 0.1, 0.03$). Simulations show a good agreement with the model.

We can model the size of the H II region in the downstream direction in a similar manner. The radius of the H II region in the downstream direction $\theta = \pi$ is determined by the second term of the Equation (5.11):

$$N_{\rm ion} \simeq 4\pi \langle R_s \rangle_{\theta=\pi}^2 n v_\infty, \tag{5.14}$$

where n can be calculated simply using pressure equilibrium condition $n_{\rm H,in} = $
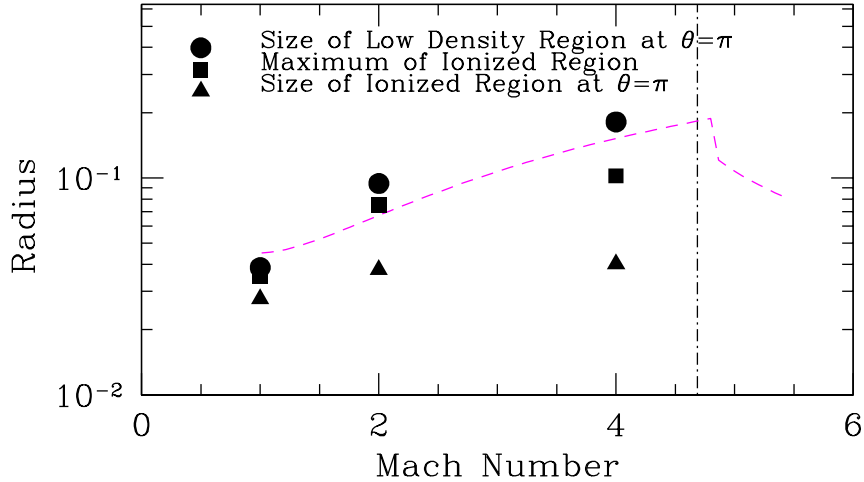
Figure 5.8: Size of low density region ($\theta = \pi$) and $\langle R_s \rangle_{\theta=\pi}$ in the downstream direction as a function of $\mathcal{M}$. Low density region is bigger than the size of ionized region due to the concentrated gas along the line of $\theta = \pi$.

$n_{\mathrm{H},\infty}\Delta_T^{-1}$. The size of the H II region in the downstream direction is

$$\langle R_s \rangle_{\theta=\pi} \propto \eta^{1/2} n_{\mathrm{H},\infty}^{1/4}(1 + \mathcal{M}^2)^{1/2}, \tag{5.15}$$

where $\langle R_s \rangle_{\theta=\pi}$ is approximately proportional to the Mach number for the range $1 < \mathcal{M} < \mathcal{M}_{\mathrm{cr}}$. Figure 5.8 shows that the model is in a good agreement with the simulations for $n_{\mathrm{H},\infty} = 10^5$ cm^{-3}.

5.3 Stability and Oscillation

As discussed in the previous section, the average accretion rate $\langle \lambda_{\mathrm{rad}} \rangle$ increases as a function of Mach number in the range $1 < \mathcal{M} < \mathcal{M}_{\mathrm{cr}}$. For the lower values in this Mach number range, all simulations approach a steady state accretion rate. Interestingly, as the Mach number approaches $\mathcal{M}_{\mathrm{cr}}$, simulations at intermediate densities($n_{\mathrm{H},\infty} = 10^3$–$10^4$ cm^{-3}), become unstable developing intermittent bursts of accretion rate due to formation/destruction of the dense shell in the upstream direction (see Whalen and Norman 2011). Figure 5.10 shows time evolution of
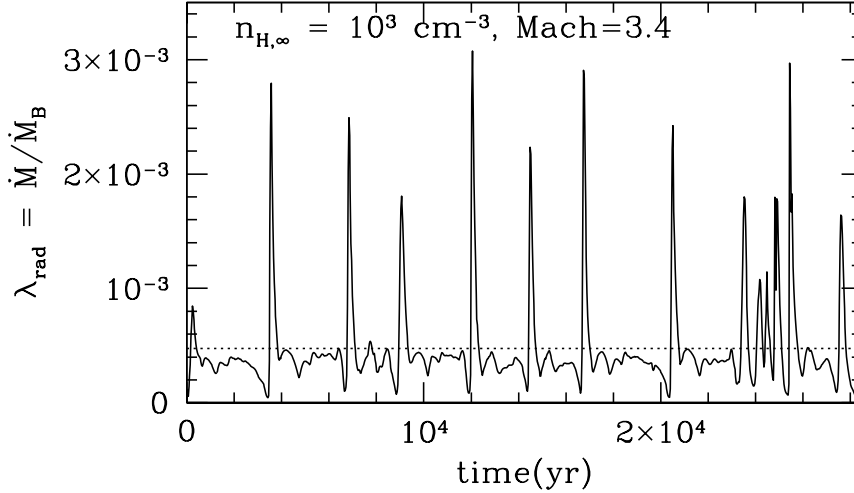
Figure 5.9: Simulation of a BH with mass $M_{bh} = 100 \ M_\odot$, gas density $10^3 \ cm^{-3}$, and temperature $T_\infty = 10^4 K$ moving at $\mathcal{M} = 3.4$. As the $\mathcal{M}$ approaches the $\mathcal{M}_{cr}$, the dense shell in the upstream direction becomes unstable since the recombination time scale τ_{rec} becomes comparable to the crossing time scale τ_{cr}. The shell forms and gets destroyed in the quasi-oscillatory behavior. When the dense shell break and fall onto the BH, accretion rate show peak luminosities which is an order of magnitude higher than the average (shown as dotted line).

a simulation with BH mass $M_{bh} = 100 \ M_\odot$, gas density $n_{H,\infty} = 10^4 \ cm^{-3}$, and temperature $T_\infty = 10^4$ K and Mach number $\mathcal{M} = 2.7$. As seen in Figure 5.3, ionizing photons create axis-symmetric H II region around the BH. In the early phase, the structure of dense shell remains relatively steady, however, instabilities develop as time evolves. When dense shell destruction happens, accretion rate increases due to the accretion of dense gas which was originally located in the dense shell. Thus, the increased accretion rate creates more ionizing photons blowing out the thinner parts of the shell. Irregularly shaped dense shells reform and break in a repetitive manner creating intermittent bursts of accretion luminosity. In case of a simulation with $n_{H,\infty} = 10^3 \ cm^{-3}$, the interval between the bursts of accretion rate is ~ 3000 years, which is very regular as seen in Figure 5.9.

In Chapters 3 and 4 we found a linear relationship between the average size of the Strömgren spheres $\langle R_s \rangle$ and the period between oscillations for stationary BHs,

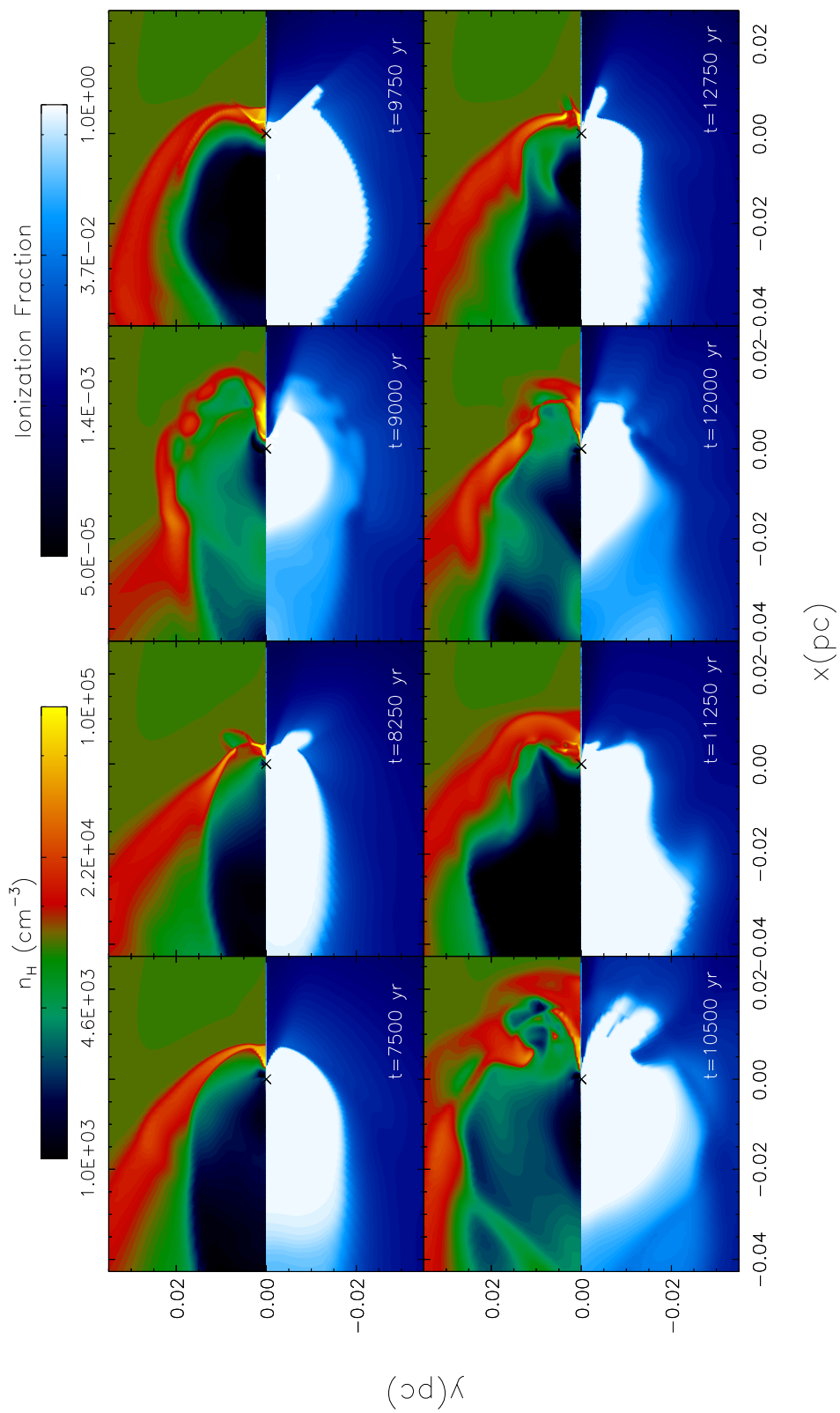Figure 5.10: Density and ionization fraction for a simulation of a BH of mass $M_{\rm bh} = 100$ $M_\odot$, gas density 10^4 cm^{-3}, and temperature $T_\infty = 10^4$ K moving at $\mathcal{M} = 2.7$. The shell forms and gets destroyed in a quasi-oscillatory behavior. When the dense shell breaks and falls onto the BH, accretion rate show peak luminosities which is a factor of 5-6 higher than the average.

which is of a few 1000 years for $M_{\rm bh} = 100~M_{\odot}$ and $\eta = 0.1$. This time scale is proportional to the sound crossing time of the H II region. The same argument can be applied for interpreting the period between intermittent bursts for moving BHs since the dense shell breaks due to the nature of instabilities of propagating I-fronts, but the following burst of luminosity reconstruct the dense shell structures by forming an expanding low density H II in the upstream direction.

5.4   Critical Velocity and Peak Luminosity

Our simple 1D model consisting of an isothermal shock and D-type I-front, predicts that accretion rate peaks at the critical Mach number $\mathcal{M}_{\rm cr}$, in a good agreement with simulations. However, the accretion rate does not reach the highest peak luminosity expected in the model. Our model assumes plane parallel gas inflow to estimate the density and velocity of the gas behind the dense shell. However, the simulations show that this assumption holds only for low Mach numbers ($\mathcal{M} \sim 1$), when the shape of the dense shock is better approximated with a plane parallel geometry, but this assumption becomes poorer with increasing $\mathcal{M}$. We run a complementary set of simulations to study more precisely the changes of the physical properties as a function of Mach number, since the simulations with constant velocities have a coarse sampling in velocity space and show an intrinsic scatter which is probably the result of out of equilibrium initial conditions. We start the simulation from $\mathcal{M} \sim 1$ and increase gradually the velocity of the gas inflow at the boundary. This type of "*wind tunnel*" numerical experiments is useful to focus on the changes of physical properties as a function of velocity, while holding the other parameters fixed. The critical Mach number $\mathcal{M}_{\rm cr}$ and the peak luminosity depend on the temperature ratio Δ_T as in Equation (5.8). Figure 5.11 shows the accretion rate as a function

of Mach number for different gas temperatures at infinity $T_\infty = 7000$, 10000, and 13000 K for $M_{\rm bh} = 100\ M_\odot$, $n_{\rm H,\infty} = 10^5$ cm^{-3}, and $\eta = 0.1$. Our model is in good agreement with simulations with different temperature T_∞ as shown in Figure 5.11. The peak accretion rates in these cases are very close to the model and the critical Mach number for each Δ_T agrees with the model. However, the caveat is that the dense shell which initially forms at the beginning of the simulations does not change its location as the velocity of gas increases as observed in the simulations in which v was held constant.

It is convenient to express the critical Mach number $\mathcal{M}_{\rm cr} \sim 2\sqrt{\Delta_T}$ as a critical velocity because $v_{\rm cr}$ is independent of T_∞:

$$v_{\rm cr} = \mathcal{M}_{\rm cr} c_{\rm s,\infty} \simeq 2 c_{\rm s,in}. \tag{5.16}$$

The velocity for peak accretion depends only on the sound speed inside the H II region and is $v_{\rm cr} = 50$ km s^{-1} for $T_{\rm in} = 6 \times 10^4$ K ($c_{\rm s,in} = 25$ km s^{-1}). As explored in Paper I, $T_{\rm in}$ depends on the hardness of the spectrum emitted by the BHs and the gas metallicity.
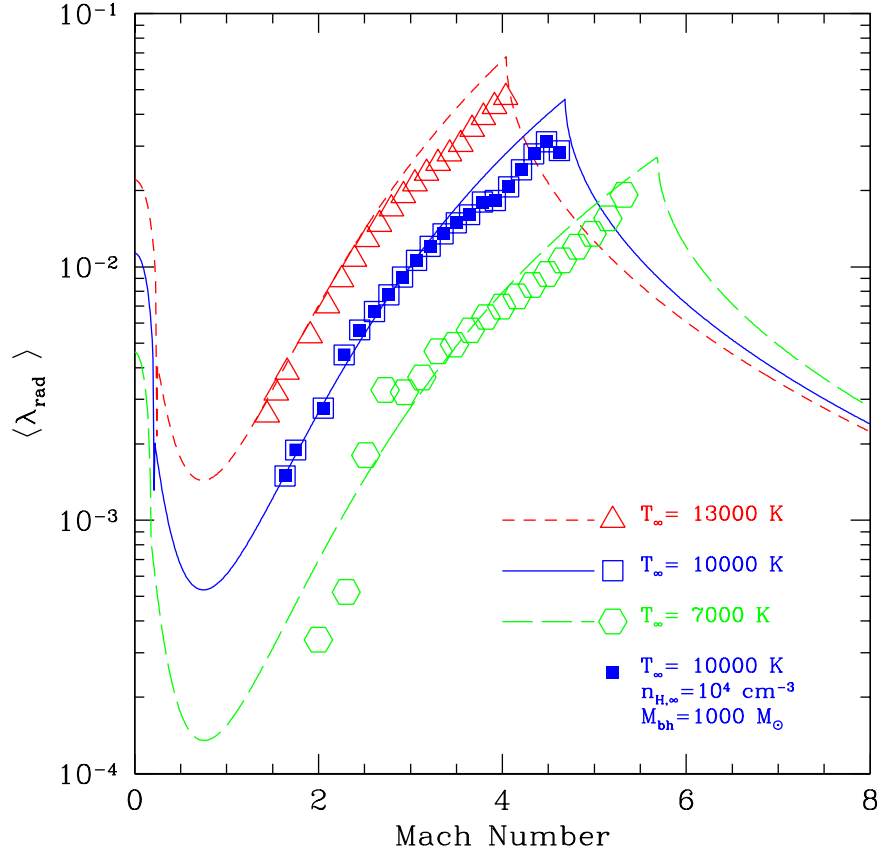
Figure 5.11: Accretion rates as a function of Mach number for simulations with $M_{\rm bh} = 100\ M_\odot$, $n_{\rm H,\infty} = 10^5\ {\rm cm}^{-3}$, and $\eta = 0.1$. Different lines and symbols show the models and simulations respectively for temperatures at infinity $T_\infty = 7000$ K (long-dashed line, open hexagon), 10000 K (solid line, open/solid squares), and 13000 K (short-dashed line, triangles). Solid squares show the simulation with higher BH mass $M_{\rm bh} = 1000\ M_\odot$ and lower ambient gas density $n_{\rm H,\infty} = 10^4\ {\rm cm}^{-3}$ which shows the identical results with the simulation with the same ambient gas temperature $T_\infty = 10000$ K.

Chapter 6

Summary and Discussion

6.1 Stationary Black Holes with Radiative Feedback

We have presented a systematic study on how the classic Bondi problem of spherical accretion onto a compact object is modified by the effects of radiation feedback. We solve radiative transfer equations in the radial direction for the hydrogen and helium ionizing radiation emitted by the BH. Gas is optically thin inside Strömgren radius while it becomes optically thick for gas outside the ionized gas. We study accretion rates and feedback loop periods while varying radiative efficiency, mass of BH, density and temperature of the medium, and spectrum of radiation. The aim of this work is to simulate feedback-regulated accretion in a wide range of the parameter space to formulate an analytical description of processes that dominate the self-regulation mechanism.

Thus, in this first part (Chapter 3) we keep the physics as simple as possible, neglecting the effect of angular momentum of the gas, radiation pressure and assuming a gas of primordial composition (i.e. metal and dust free). We find an oscillatory

behavior of the accretion rate that can be explained by the effect of UV and X-ray photo-heating. The ionizing photons produced by the BH near the gravitational radius increase gas pressure around the BH. This pressure prevents the surrounding gas from being accreted. An over-dense shell starts to form just outside the Strömgren sphere. Due to the decreased accretion rate, the number of emitted ionizing photons decreases and the density inside the Strömgren sphere also decreases with time. Gas accretion onto the BH is dominant in decreasing the density inside the H II region only for ambient gas density $n_{\mathrm{H},\infty} \gtrsim 10^7$ cm^{-3}; for lower values of the ambient gas density the gas inside the H II region is pushed outward toward the dense shell by a pressure gradient that develops behind the ionization front. Eventually, the pressure gradient inside the Strömgren sphere is not able to support the weight of the over-dense shell that starts to fall toward the BH. The accretion rate rapidly increases and the Strömgren sphere starts to expand again.

We find that the average accretion rate is sensitive to the temperature of the ambient medium and to the temperature profile inside the ionized bubble, and so depends on the gas cooling function and spectral energy distribution of the radiation. The period of the accretion bursts is insensitive to the temperature structure of the H II region, but is proportional to its radius. Our simulations show that 1D results adequately reproduce 2D results in which instabilities often develop. The dependencies of $\langle \lambda_{\mathrm{rad}} \rangle$ and τ_{cycle} on our free parameters can be explained analytically. Assuming pressure equilibrium across the Strömgren sphere is a key ingredient to derive the dependence of $\langle \lambda_{\mathrm{rad}} \rangle$ on T_{∞}, whereas the linear relation between the average size of the Strömgren sphere and τ_{cycle} is used to derive the dependence of τ_{cycle} on all the parameters we varied.

The qualitative picture of the feedback loop agrees with the description of X-ray bursters in Cowie et al. (1978). After extrapolating our analytical formulas to BHs of

a few solar masses studied by Cowie et al. (1978), we find that the average accretion rate is in good agreement ($L \sim 2 \times 10^{35}$ erg/s). However, the details of the accretion rate as a function of time, the burst period and peak accretion rates show qualitative differences. Cowie et al. (1978) simulations do not show periodic oscillation while our simulations have well-defined fast rise and exponential decay of accretion followed by quiescent phases of the accretion rate. This regular pattern of accretion bursts is possible only when spherical symmetry is maintained on relatively large scales during oscillations. An axisymmetric radiation source (Proga 2007; Proga et al. 2008; Kurosawa et al. 2009; Kurosawa and Proga 2009a,b) or inhomogeneous initial condition on scale of the Bondi radius can break the symmetry.

In Chapter 4, we have focused on the effects that radiation pressure and angular momentum have on the gas supply and accretion rate onto the BH. The simulations focused on accretion onto IMBHs but the analytical scaling relationships we have derived are rather general, and although the initial conditions are somewhat idealized, should describe reality more accurately than the classical Bondi formulae.

In our models we have assumed that the BH accretes from a uniform density and temperature reservoir, significantly larger than the Bondi radius and $\langle R_s \rangle$. This assumption is well motivated for accretion onto stellar and IMBH, but for SMBH there could be supply of gas to the BH from stars within $\langle R_s \rangle$ (stellar winds) or other astrophysical object (merger-driven accretion, etc). The scaling relationships can be applied to problems involving a wide range of masses of the accretor, from stellar mass objects (e.g., Wheeler and Johnson 2011) to supermassive BHs. One caveat is that we are neglecting the effects of self-gravity of the gas (see Li 2011) and the gravitational potential due to the dark matter halo of the host galaxy, which may play an important role for the case of accretion onto supermassive BHs. Indeed, a simple calculation shows that at the I-front gravity due to the mass of the gas

inside the Strömgren sphere exceeds the BH's gravity if $M_{\rm bh} \gtrsim 10^6\ M_\odot/(\eta_{-1}T_{\infty,4})$. Our model predicts scaling relationships for the period, duty cycle, peak and mean accretion onto the BH, as well as relevant critical densities and size of the Strömgren sphere around the BH. In the following summary of the scaling relationships, we express $T_{\rm in}$ in the equations in terms of $\bar{E}$ given by Equation (4.12) that is valid for a gas of low-metallicity. $\bar{E}$ is related to the spectral index α by Equation (4.11). For higher values of the gas metallicity, the coefficients in the equations can be different due to changes in the relationship between $T_{\rm in}$ and the spectrum of the radiation. A caveat is that our simulations have explored a large but limited parameter space for the masses of the BHs, temperature and density of the ambient gas, etc. So, the proposed scaling relationships, although they are based on a physically motivated model we inferred from the simulations, should be used with caution for sets of parameters that are significantly different from the range confirmed by simulations.

The main qualitative result of our study is that radiation feedback produces periodic oscillations of the accretion rate from large scales onto the BH, and thus periodic short-lived bursts of the BH luminosity. We found two modes of self-regulated accretion, determined by

$$n_{\rm H,\infty}^{\rm cr} \sim \frac{5 \times 10^6\ {\rm cm}^{-3}}{M_{\rm bh,2}} \left(\frac{\bar{E}}{41\ {\rm eV}} \right)^{-9/16}. \tag{6.1}$$

If $n_{\rm H,\infty} < n_{\rm H,\infty}^{\rm cr}$ (mode-I), the accretion luminosity of the BH has regular bursts with period $\tau_{\rm cycle}^{\rm I}$ during which the BH increases its brightness by about 5 orders of magnitude but only for a short fraction of the cycle period: the duty cycle is $f_{\rm duty}^{\rm I} \equiv \tau_{\rm on}/\tau_{\rm cycle} \sim 6\%\ T_{\infty,4}^{1/2}$. During the quiescent phase in the accretion cycle the gas accumulates in a dense shell in front of the H II region rather than accreting directly onto the BH. As the luminosity decreases after the burst, the density inside the H II region also decreases because is pushed outward by a pressure gradient, thus maintaining the I-front radius nearly constant. Eventually the density and pressure

inside the H II region cannot sustain the weight of the dense shell that collapses producing a burst of accretion. The cycle repeats regularly. If $n_{\mathrm{H},\infty} > n_{\mathrm{H},\infty}^{\mathrm{cr}}$ (mode-II) the cycle is qualitatively different: the duty cycle is about $f_{\mathrm{duty}}^{\mathrm{II}} \gtrsim 50\%$ and the peak accretion rate is only a few times the mean. There is no collapse phase of the dense shell and the H II region remains roughly stationary while the accretion rate oscillates. The physical motivation for mode-II accretion is that the timescale for the depletion of the gas inside the H II region becomes dominated by accretion onto the BH. Only for mode-II accretion the BH growth rate can approach the Eddington limit, given that the density exceeds the critical density

$$n_{\mathrm{H},\infty}^{\mathrm{Edd}} \sim \frac{4 \times 10^6 \ \mathrm{cm}^{-3}}{M_{\mathrm{bh},2}} T_{\infty,4}^{-1} \eta_{-1}^{-1}. \tag{6.2}$$

For nearly all realistic cases $n_{\mathrm{H},\infty}^{\mathrm{Edd}} \gtrsim n_{\mathrm{H},\infty}^{\mathrm{cr}}$.

For $M_{\mathrm{bh}} = 100 \ M_\odot$, at densities $10^5 \ \mathrm{cm}^{-3} \leq n_{\mathrm{H},\infty} \leq n_{\mathrm{H},\infty}^{\mathrm{Edd}}$ the *mean accretion rate* onto the BH, in units of the Bondi rate is $\langle \lambda_{\mathrm{rad}} \rangle \sim 1\% T_{\infty,4}^{2.5} (\bar{E}/41 \ \mathrm{eV})^{-1}$, independent of all the other parameters. For $n_{\mathrm{H},\infty} < 10^5 \ \mathrm{cm}^{-3}$ instead, $\langle \lambda_{\mathrm{rad}} \rangle \sim 1\% (n_{\mathrm{H},\infty}/10^5 \ \mathrm{cm}^{-3})^{1/2} T_{\infty,4}^{2.5} (\bar{E}/41 \ \mathrm{eV})^{-1}$, depends weakly on the gas density. One caveat is that in Paper I the dependence on the free parameters of the transition density $10^5 \ \mathrm{cm}^{-3}$ has been only partially explored. As shown in Figure 4.4, the simulation results are consistent with a transition density inversely proportional to the BH mass. Hence, if $10^5 M_{\mathrm{bh},2}^{-1} \ \mathrm{cm}^{-3} \leq n_{\mathrm{H},\infty} \leq n_{\mathrm{H},\infty}^{\mathrm{Edd}}$ the mean accretion rate is proportional to the thermal pressure $n_{\mathrm{H},\infty} T_\infty$ of the ambient gas:

$$\langle \dot{M} \rangle \approx (4 \times 10^{18} \ \mathrm{g \ s}^{-1}) M_{\mathrm{bh},2}^2 \left(\frac{n_{\mathrm{H},\infty}}{10^5 \ \mathrm{cm}^{-3}} \right) T_{\infty,4} \left(\frac{\bar{E}}{41 \ \mathrm{eV}} \right)^{-1}. \tag{6.3}$$

If $n_{\mathrm{H},\infty} > n_{\mathrm{H},\infty}^{\mathrm{Edd}}$ then $\langle \dot{M} \rangle = L_{\mathrm{Edd}} (\eta c^2)^{-1}$. The duty cycle is

$$f_{\mathrm{duty}} = \begin{cases} f_{\mathrm{duty}}^{\mathrm{I}} \approx 6\% T_{\infty,4}^{1/2} & \text{if } n_{\mathrm{H},\infty} \leq n_{\mathrm{H},\infty}^{\mathrm{cr}} \\[2mm] f_{\mathrm{duty}}^{\mathrm{II}} \gtrsim 50\% & \text{if } n_{\mathrm{H},\infty} > n_{\mathrm{H},\infty}^{\mathrm{cr}}, \end{cases} \tag{6.4}$$

90

and the maximum accretion luminosity which depends on the duty cycle thus is,

$$\frac{L^{\mathrm{max}}}{L_{\mathrm{Edd}}} \approx \min\left[1, \mathcal{A}\eta_{-1}M_{\mathrm{bh},2}\left(\frac{n_{\mathrm{H},\infty}}{10^5 \ \mathrm{cm}^{-3}}\right)T_{\infty,4}\left(\frac{\bar{E}}{41 \ \mathrm{eV}}\right)^{-1}\right], \tag{6.5}$$

where $L_{\mathrm{Edd}} = 1.3 \times 10^{40} M_{\mathrm{bh},2}$ erg s^{-1}, and

$$\mathcal{A} = \begin{cases} \mathcal{A}^{\mathrm{I}} \approx 0.5 \ T_{\infty,4}^{-1/2} & \text{if } n_{\mathrm{H},\infty} \leq n_{\mathrm{H},\infty}^{\mathrm{cr}} \\[2mm] \mathcal{A}^{\mathrm{II}} \approx 0.06 & \text{if } n_{\mathrm{H},\infty} > n_{\mathrm{H},\infty}^{\mathrm{cr}} \end{cases} \tag{6.6}$$

The cycle of the oscillations also falls into two regimes:

$$\tau_{\mathrm{cycle}} = \begin{cases} \tau_{\mathrm{cycle}}^{\mathrm{I}} \approx (0.1 \ \mathrm{Myr}) \ M_{\mathrm{bh},2}^{2/3}\eta_{-1}^{1/3}(\frac{n_{\mathrm{H},\infty}}{1 \ \mathrm{cm}^{-3}})^{-1/3}(\frac{\bar{E}}{41 \ \mathrm{eV}})^{-3/4}, & \text{if } n_{\mathrm{H},\infty} \leq n_{\mathrm{H},\infty}^{\mathrm{cr}} \\[2mm] \tau_{\mathrm{cycle}}^{\mathrm{II}} \approx (1 \ \mathrm{Gyr}) \ \eta_{-1}(\frac{n_{\mathrm{H},\infty}}{1 \ \mathrm{cm}^{-3}})^{-1}(\frac{\bar{E}}{41 \ \mathrm{eV}})^{-7/8}, & \text{if } n_{\mathrm{H},\infty} > n_{\mathrm{H},\infty}^{\mathrm{cr}}. \end{cases} \tag{6.7}$$

6.2 Radiation-regulated accretion onto Black Holes in Motion

In Chapter 5, we have focused on the effect of motion of BHs relative to surrounding gas. The followings are the key findings.

- The quasi-periodic oscillation of the accretion rate and size of the Strömgren sphere observed for stationary BHs are only observed for subsonic motions, and we find a distinct axis-symmetric hydrodynamic structure in the supersonic regime. A dense shell develops in front of the H II region in the upstream direction and the size of the H II region in the downstream direction becomes elongated, being proportional to the velocity, v_∞, of the gas outside the H II region.

- We find that the accretion rate decreases as a function of Mach number for subsonic motion, and surprisingly increases with increasing $\mathcal{M}$ in the range

of Mach numbers $1 < \mathcal{M} < \mathcal{M}_{\mathrm{cr}}$. The accretion rate peaks at the critical Mach number $\mathcal{M}_{\mathrm{cr}}$ and start decreasing for $\mathcal{M} > \mathcal{M}_{\mathrm{cr}}$ converging to the Bondi-Hoyle-Lyttleton solution, which does not consider the effect of radiative feedback. We show that the accretion rate as a function of Mach number and other parameters can be understood well due to the formation of dense shell in the upstream direction which changes the density and velocity of the gas behind the I-front. An isothermal shock and a D-type I-front are the key elements to model the accretion.

- The time dependence of the accretion rate as a function of Mach number shows a strong dependence on the ambient gas densities. We find steady solutions for simulations with high density ($n_{\mathrm{H},\infty} = 10^5 - 10^6$ cm^{-3}) for all Mach numbers. For intermediate densities ($n_{\mathrm{H},\infty} = 10^3 - 10^4$ cm^{-3}), we find intermittent bursts of accretion rate in the Mach number range $2.5 \lesssim \mathcal{M} \lesssim \mathcal{M}_{\mathrm{cr}}$. The oscillatory behavior of accretion rate is due to formation/destruction of the dense shell in the upstream direction that becomes unstable. We observe the formation of a shell with lower overdensity than in the isothermal case in lower density regime, $n_{\mathrm{H},\infty} \lesssim 10^2$ cm^{-3}. For $\mathcal{M} > \mathcal{M}_{\mathrm{cr}}$ at all densities, the dense shell does not form, providing steady accretion rates.

- The critical Mach number $\mathcal{M}_{\mathrm{cr}}$ where the accretion rate peaks can be translated to the corresponding critical velocity which is approximately twice of the sound speed inside the H II region. We find that the critical velocity is $v_{\mathrm{cr}} \sim 50$ km s^{-1} for $T_{\mathrm{in}} = 6 \times 10^4$ K.

As mentioned in Chapter 1, the axis-symmetric flows and a moving BH are not stable. Interestingly, most of the instabilities developing in the downstream direction discussed in the literature do not affect much the accretion rate onto BHs

because the effective Bondi radius inside the ionized region is smaller than the typical distance at which these features develop. Also Rayleigh-Taylor or Kelvin-Helmholtz instabilities or radiation hydrodynamical instabilities of the shell in front of the I-front do not grow for low Mach numbers, due to the stabilizing effect of a pressure gradient inside the H II region. However, when the dense shell breaks down due to instabilities in the I-fronts (see Whalen and Norman 2011) as shown in some simulations (for $n_{H,\infty} = 10^3$–10^4 cm^{-3}), clumpy structures develop rapidly as shown in Figure 5.10 and is amplified by a fraction of ionizing photons escaping the shell. Some of this clumpy structure is accreted onto the BHs boosting the luminosity which produces an accelerating I-front helping to reform a dense shell. The luminosity at the moment of the bursts can be $\sim$ 5–10 times larger than the average luminosity, depending on the density of the shell, and thus the Mach number. The stability of dense shell in the upstream direction depends strongly on the gas density at infinity. BHs moving through a higher density gas form a thicker post-shock shell with a sharper jump of density, and thus a stiffer pressure gradient which more efficiently suppresses the development of instabilities inside the I-fronts. The column density of the shell can also affect the instability since the column density of the thinner parts of the shell at higher densities is large enough to trap the photons inside the shell, avoiding the disrupting effect of ionizing photons leaking out of the shell region.

6.3 Future Works

The astrophysical applications of this thesis are innumerable since we have revisited one of the most fundamental problems in astrophysics, that of gravitational gas accretion onto compact objects. The following is a list of future works in which we

can apply our improved accretion recipes.

- **Black Hole Growth and Luminosity** : One of the most obvious results of this thesis is that the luminosity of an accreting BH should be significantly smaller than the value inferred applying the Bondi formula, which is still used in many cosmological simulations. The effect of overestimated accretion rate in the sub-Eddington regime can now be addressed properly. Not only do we find the mean accretion rate to always be $\leq 1\%$ of the Bondi rate, but also if $n_{\mathrm{H},\infty} < n_{\mathrm{H},\infty}^{\mathrm{cr}}$, for 94% of the time the BH luminosity is about five orders of magnitude lower than the rate found using the Bondi formulae. Thus, our model could have interesting consequences to our interpretation of the observed quiescence of SMBHs in ellipticals and Sgr A^*. Also, the duty cycle of $\sim 6\%$ we found is interestingly close to the fraction of galaxies with AGNs, $\sim 3\%$ found in deep field surveys (e.g., Steidel et al. 2002; Luo et al. 2011).

- **Primordial Black Holes** : We also found that IMBHs can grow at near the Eddington limit under special conditions if $n_{\mathrm{H},\infty} > n_{\mathrm{H},\infty}^{\mathrm{Edd}}$. This has potentially important consequences on the ability of seed IMBH from Pop III stars to grow by accretion into SMBH during the first Gyrs of the Universe age. This possibility seemed precluded if the duty cycle of the burst was 6% as found in previous works, but the existence of massive quasars at $z \sim 7$ can be tested applying our models to cosmological simulations.

- **IMBHs in DM minihalo** : The first stars (Pop III) are thought be massive (~ 100 $\mathrm{M}_\odot$) and form at the center of primordial minihalos of mass 10^6–10^7 $\mathrm{M}_\odot$, possibly one in each minihalo. If the Pop III stars collapse directly into primordial BHs or they explode as normal SNe, then IMBHs should still be sitting at the centers of minihalos even in the current universe. Although

gas in primordial minihalos is lost completely due to radiative and SN feedback and new gas accretion is prevented after reionization, they may accrete gas again at redshift $z < 1$, in the context of *secondary infall* onto dark minihalos (Ricotti 2009). We expect to apply our results to this problem and estimate the luminosity of IMBHs at the centers of dark matter minihalos at $z = 0$ and their expected number around the Milky Way.

- **ULXs** : Although the nature of ULXs is unknown, there are indications that they may host an IMBH (e.g., Strohmayer and Mushotzky 2009). Our model predicts that an IMBH accreting from an ISM with high pressure such as dense molecular cloud ($n_{\mathrm{H},\infty} T_\infty \sim 10^5$–$10^7$ cm^{-3} K) would be $L^{\mathrm{max}} \sim 10^{37}$–$10^{39}$ erg/s for $M_{\mathrm{bh}} = 1000$ M$_\odot$, that is comparable to the luminosity of ULXs. However, this assumes that the IMBH is at rest with respect to the ISM. The motion of BHs is expected to reduce accretion rate dramatically, however we find that the maximum accretion rate for a moving BH can be larger than that of a stationary BH of the same mass, accreting from the same medium if the medium temperature is $T < 10^4$ K. Thus, we can make a better model the accretion luminosity from BHs in motion and this can be applied to understand the observed population of ULXs in nearby galaxies.

Clearly, a significant amount of new research is needed to address each of the aforementioned topics in detail, but the basic ground work presented in the thesis may allow the re-visitation of a few longstanding problems still unsolved in astrophysics.

Appendix A

Glossary

A.1 Abbreviations

BH: Black Hole

IMBH: Intermediate-Mass Black Hole

SMBH: Super-Massive Black Hole

I-front: Ionization Front

AGN: Active Galactic Nuclei

ULX: Ultra-luminous X-ray Source

SED: Spectral Energy Distribution

RT: Rayleigh-Taylor

ISM: Interstellar medium

A.2 Definitions and Symbols

α: spectral index of power-law spectra

α–model: Shakura-Sunyaev standard thin disk model

$\alpha_{\rm disk}$: viscosity parameter

$\alpha_{\rm rec}$: recombination Coefficient

$c_{\rm s,in}$: sound speed of gas at $r_{\rm acc}$

$c_{\rm s,\infty}$: sound speed of gas at infinity

$\bar{E}$: mean energy of photons emitted from black hole

η: radiative efficiency

F_ν: flux of ionizing photons at frequency ν

$f_{\rm duty}$: duty cycle

γ: polytropic index

H I: neutral hydrogen

H II: ionized hydrogen

He I: neutral helium

He II: singly ionized helium

He III: doubly ionized helium

$L_{\rm Edd}$: Eddington luminosity

$\lambda_{\rm rad}$: accretion rate normalized by Bondi accretion rate for isothermal gas

$\langle \lambda_{\rm rad} \rangle$: time-averaged $\lambda_{\rm rad}$

$\lambda_{\rm rad,max}$: $\lambda_{\rm rad}$ at peak luminosity

$\lambda_{\rm RT}$: Rayleigh-Taylor instability wavelength

l: dimensionless luminosity normalized by $\dot{L}_{\rm Edd}$

$M_{\rm bh}$: black hole mass

$\dot{M}_{\rm B}$: Bondi accretion rate for isothermal gas

$\dot{M}_{\rm Edd}$: Eddington accretion rate assuming $\eta = 0.1$

$\dot{m}$: dimensionless accretion rate normalized by $\dot{M}_{\rm Edd}$

$\mathcal{M}$: Mach number

$\mathcal{M}_{\rm cr}$: critical Mach number

$M_\odot$: solar mass

$n_{\rm H,\infty}$: gas number density at infinity

$n_{\rm H,\infty}^{\rm cr}$: critical gas number density for the transition from mode-I to mode-II oscillation

$n_{\rm H,\infty}^{\rm Edd}$: gas number density where the accretion starts to become Eddington-limited

$R_{\rm Sch}$: Schwartzschild radius

$r_{\rm b}$: outer Bondi radius calculated using $c_{\rm s,\infty}$

r_s: sonic radius

$r_{\rm b,in}$: inner Bondi radius calculated using $c_{\rm s,in}$

$r_{\rm acc}$: accretion radius inside a Strömgren sphere

$\langle R_s \rangle$: time-averaged size of Strömgren sphere

ρ_∞: gas density at infinity from BH

$\rho_{\rm sh}$: gas density inside the dense shell for moving BH

$r_{\rm min}, r_{\rm max}$: minimum/maximum radius of simulation grid

Strömgren sphere: hot and ionized region due to high energy photons from massive stars or BHs

σ_T: Thomson cross section

T_∞: gas temperature at infinity

$T_{\rm in}$: gas temperature at $r_{\rm acc}$ in H II region

$t_{\rm ff}$: free-fall timescale

$t_{\rm visc}$: viscous timescale

$\tau_{\rm on}$: fraction of time the BH is active

τ_{cycle}: mean period between luminosity peaks

$x_{\mathrm{H\ I}}$, $x_{\mathrm{H\ II}}$: fraction of neutral/ionized hydrogen

x_e: fraction of electron

Appendix B

Code Evaluation

B.1 Basic Tests of the Code

We test the Bondi accretion formula using ZEUS-MP for the adiabatic indexes $\gamma = 1.2, 1.4$ and 1.6. Figure B.1 shows how the accretion rate changes as a function of radius. Bondi accretion expects same rate within Bondi radius ($r_{\rm b}$) and this matches well with the simulations. For a given equation of state, the sonic point where the gas inflow becomes supersonic must be resolved not to overestimate the accretion rate λ_B. Figure B.2 shows the steady accretion rate as a function of the radius at the inner boundary normalized by the Bondi radius. Different lines show results for $\gamma =$1.2, 1.4 and 1.6.

We also test whether our radiative transfer module produces radii of the Strömgren spheres in agreement with the analytical prediction: $(4\pi/3)R_s^3 n_e n_H \alpha_{rec} = N_{ion}$, where R_s is the Strömgren radius and N_{ion} is the number of ionizing photons emitted per unit time. Figure B.3 shows the test of the 1D radiative transfer module without hydrodynamics. Different symbols indicates the radii for the different ionization fractions: $x_e = 0.99$ (circle), 0.90 (square), 0.50 (triangle).
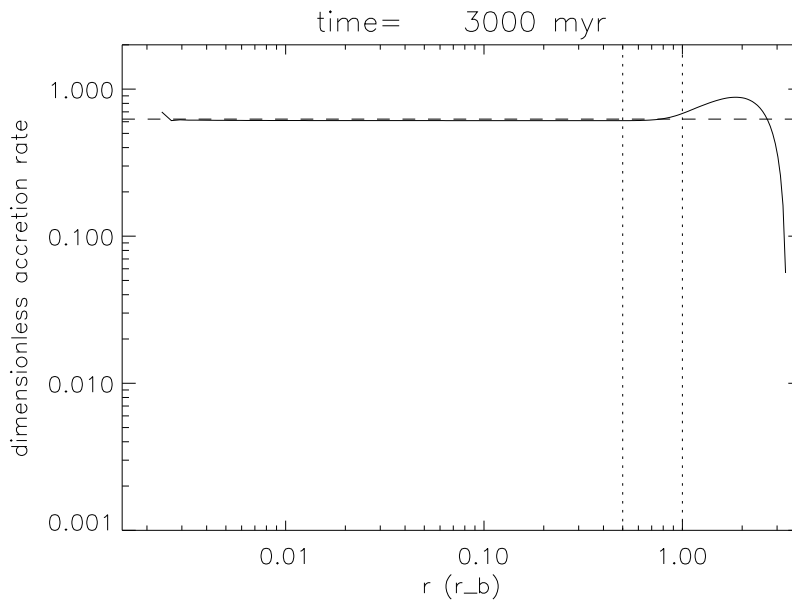
Figure B.1: Dimensionless accretion rate as a function of radius at 3 Gyr. The dashed line shows the expected dimensionless accretion rate ($\lambda_B = 0.625$) given $\gamma = 1.4$. Accretion rate as a function of radius is same for inside the Bondi radius.

B.2 Radiative Transfer Module and Time Stepping

Our hydrodynamic calculation is performed using ZEUS-MP, returning the density and gas energy at each time step to the radiative transfer module. The operator-splitting method is applied to mediate between hydrodynamics and radiative transfer with a photon-conserving method. For each line of sight radiative transfer equations are solved in the following order:

1. At the inner boundary, the average inflow mass flux $\dot{M}$ is calculated.

2. The mass flux is converted into accretion luminosity L, and thus into the
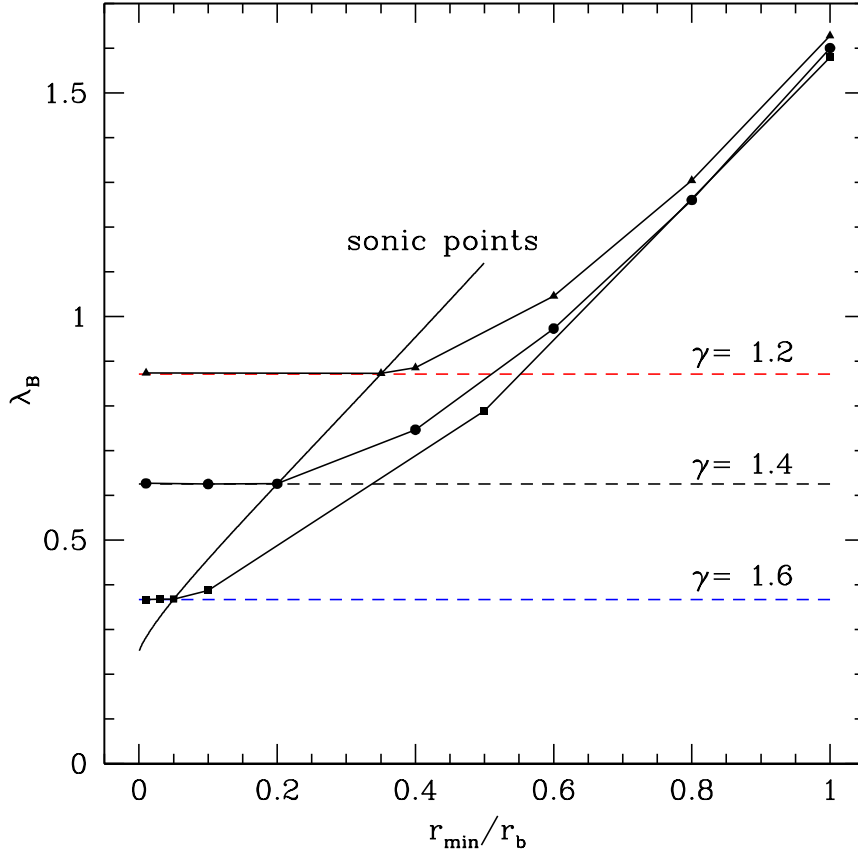
Figure B.2: Simulated Bondi accretion rate(λ_B) as a function of minimum radius with given adiabatic index γ without radiative feedback. Dashed lines are analytically estimated values for each γ =1.2, 1.4 and 1.6. In order not to overestimate accretion rate sonic point should be resolved where the velocity of the inflowing gas becomes supersonic.

    number of ionizing photons for a given radiative efficiency η.

3. The photon spectrum is determined using a power law spectral energy distribution with the spectral index α. We use up to 300 logarithmically spaced frequency bins for photons between 10 eV up to 100 keV.

4. The ordinary differential equation for time-dependent radiative transfer cooling/heating and chemistry of the gas are solved using a Runge-Kutta or Semi-Implicit solver for each line of sight with a maximum of 10% error. Photo-heating, cooling for a given cooling function and Compton cooling are calcu-
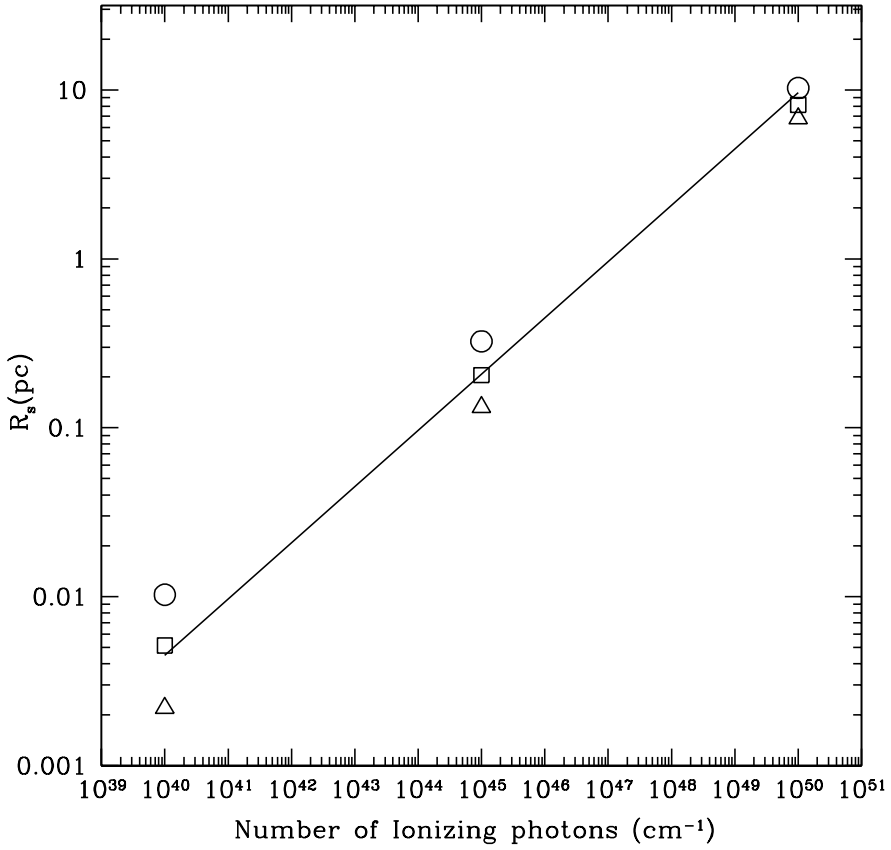
Figure B.3: Test of Strömgren radius with given number of ionizing photons. Solid line is the prediction for the given number of ionizing photons from 10^{40} to 10^{50} s^{-1}. Triangle symbols represent location where ionization fraction of n_{H} (x_{HI}) is 0.50. Squares are for $x_{\mathrm{HI}} = 0.90$ and circles are for $x_{\mathrm{HI}} = 0.99$.

lated.

5. The energy density and the abundances of neutral and ionized hydrogen are updated.

Parallelization is easily implemented in polar angle direction because radiative transfer calculations along each ray are independent of one another.

B.3 Resolution Studies

We perform a resolution study to confirm that the number of grid zones does not affect the results. Number of zones from 384 to 768 are tested and they all show the similar outputs in terms of accretion rate at peaks, average accretion rate, decaying shape and the period between peaks . Figure B.4 shows that the details of the accretion rate history from simulations are not identical but the physical quantities which we are interested in (average accretion rate, peak accretion rate and period of the bursts) do not show significant deviation from each other. In general, a Courant number of 0.5 is used for most simulations, but we try a Courant number which is one order of magnitude smaller to investigate how the results are affected by reducing the hydro-time step by an order of magnitude. The chemical/cooling time steps are calculated independently by the radiation transfer module.
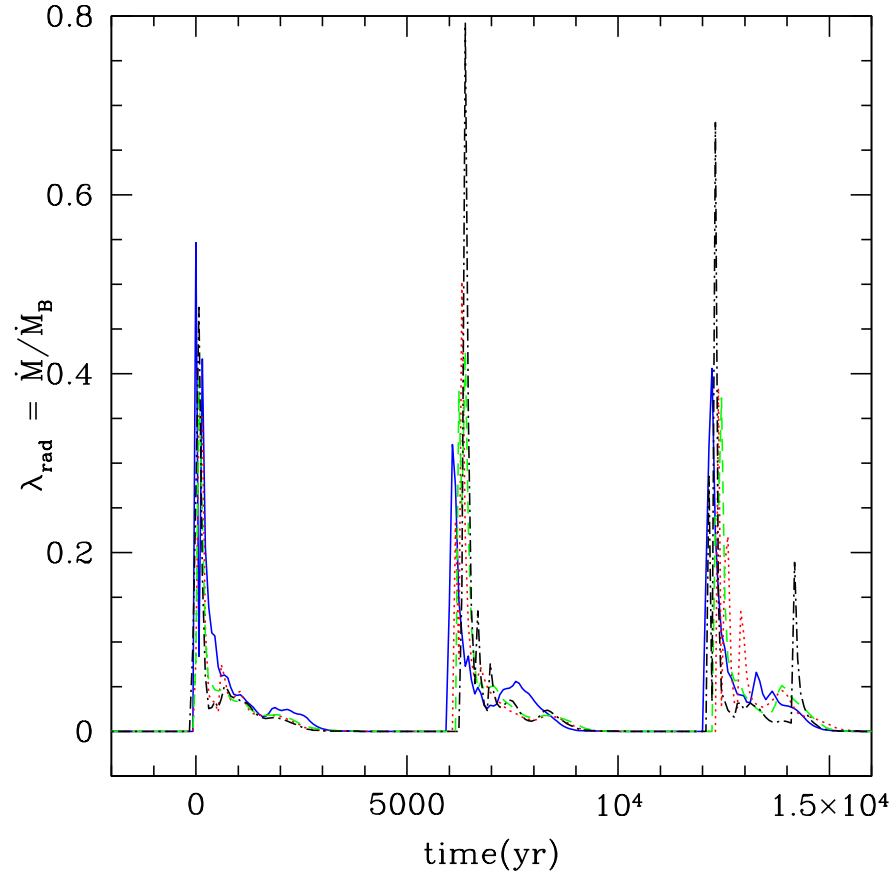
Figure B.4: Comparisons between simulations of $\eta = 0.1$, $M_{\rm bh} = 100\ {\rm M_\odot}$, $n_{\rm H,\infty} = 10^5\ {\rm cm^{-3}}$ and $T_\infty = 10^4$ K with various resolution. *Solid* : 384 grid run. *Dotted* : 512 grid run. *Long dashed* 768 grid run. *Short dashed* : 512 grid with Courant number of 0.05.

Bibliography

Abel, T., Anninos, P., Norman, M. L., and Zhang, Y. (1998). First structure formation. i. primordial star-forming regions in hierarchical models. *ApJ*, 508:518–529.

Abel, T., Bryan, G. L., and Norman, M. L. (2000). The Formation and Fragmentation of Primordial Molecular Clouds. *ApJ*, 540:39–44.

Alvarez, M. A., Wise, J. H., and Abel, T. (2009). Accretion onto the First Stellar-Mass Black Holes. *ApJ*, 701:L133–L137.

Begelman, M. C. (1985). The effects of X-rays from an active galactic nucleus on the interstellar medium of the host galaxy. *ApJ*, 297:492–506.

Begelman, M. C., Volonteri, M., and Rees, M. J. (2006). Formation of supermassive black holes by direct collapse in pre-galactic haloes. *MNRAS*, 370:289–298.

Bisnovatyi-Kogan, G. S. and Blinnikov, S. I. (1980). Spherical accretion on to compact X-ray sources with preheating - No thermal limit for the luminosity. *MNRAS*, 191:711–719.

Bondi, H. (1952). On spherically symmetrical accretion. *MNRAS*, 112:195–+.

Bondi, H. and Hoyle, F. (1944). On the mechanism of accretion by stars. *MNRAS*, 104:273–+.

Bromm, V., Coppi, P. S., and Larson, R. B. (1999). Forming the First Stars in the Universe: The Fragmentation of Primordial Gas. *ApJ*, 527:L5–L8.

Carr, B. J., Bond, J. R., and Arnett, W. D. (1984). Cosmological consequences of Population III stars. *ApJ*, 277:445–469.

Ciotti, L. and Ostriker, J. P. (2007). Radiative Feedback from Massive Black Holes in Elliptical Galaxies: AGN Flaring and Central Starburst Fueled by Recycled Gas. *ApJ*, 665:1038–1056.

Ciotti, L., Ostriker, J. P., and Proga, D. (2009). Feedback from Central Black Holes in Elliptical Galaxies. I. Models with Either Radiative or Mechanical Feedback but not Both. *ApJ*, 699:89–104.

Cowie, L. L., Ostriker, J. P., and Stark, A. A. (1978). Time-dependent spherically symmetric accretion onto compact X-ray sources. *ApJ*, 226:1041–1062.

Di Matteo, T., Colberg, J., Springel, V., Hernquist, L., and Sijacki, D. (2008). Direct Cosmological Simulations of the Growth of Black Holes and Galaxies. *ApJ*, 676:33–53.

Fan, X., Strauss, M. A., Schneider, D. P., Becker, R. H., White, R. L., Haiman, Z., Gregg, M., Pentericci, L., Grebel, E. K., Narayanan, V. K., Loh, Y., Richards, G. T., Gunn, J. E., Lupton, R. H., Knapp, G. R., Ivezić, Ž., Brandt, W. N., Collinge, M., Hao, L., Harbeck, D., Prada, F., Schaye, J., Strateva, I., Zakamska, N., Anderson, S., Brinkmann, J., Bahcall, N. A., Lamb, D. Q., Okamura, S., Szalay, A., and York, D. G. (2003). A Survey of z¿5.7 Quasars in the Sloan Digital Sky Survey. II. Discovery of Three Additional Quasars at z¿6. *AJ*, 125:1649–1659.

Fryer, C. L., Woosley, S. E., and Heger, A. (2001). Pair-Instability Supernovae, Gravity Waves, and Gamma-Ray Transients. *ApJ*, 550:372–382.

Greif, T. H., Johnson, J. L., Klessen, R. S., and Bromm, V. (2008). The first galaxies: assembly, cooling and the onset of turbulence. *MNRAS*, 387:1021–1036.

Haehnelt, M. G., Natarajan, P., and Rees, M. J. (1998). High-redshift galaxies, their active nuclei and central black holes. *MNRAS*, 300:817–827.

Hayes, J. C., Norman, M. L., Fiedler, R. A., Bordner, J. O., Li, P. S., Clark, S. E., ud-Doula, A., and Mac Low, M.-M. (2006). Simulating Radiating and Magnetized Flows in Multiple Dimensions with ZEUS-MP. *ApJS*, 165:188–228.

Hoyle, F. and Lyttleton, R. A. (1939). The effect of interstellar matter on climatic variation. In *Proceedings of the Cambridge Philosophical Society*, volume 35 of *Proceedings of the Cambridge Philosophical Society*, pages 405–+.

Johnson, J. L. and Bromm, V. (2007). The aftermath of the first stars: massive black holes. *MNRAS*, 374:1557–1568.

Johnson, J. L., Khochfar, S., Greif, T. H., and Durier, F. (2011). Accretion on to black holes formed by direct collapse. *MNRAS*, 410:919–933.

Kim, J.-h., Wise, J. H., Alvarez, M. A., and Abel, T. (2011). Galaxy Formation with Self-consistently Modeled Stars and Massive Black Holes. I. Feedback-regulated Star Formation and Black Hole Growth. *ApJ*, 738:54.

Krolik, J. H. and Kallman, T. R. (1984). Soft X-ray opacity in hot and photoionized gases. *ApJ*, 286:366–370.

Krolik, J. H. and London, R. A. (1983). Spherical accretion onto quasars. *ApJ*, 267:18–30.

Krolik, J. H., McKee, C. F., and Tarter, C. B. (1981). Two-phase models of quasar emission line regions. *ApJ*, 249:422–442.

Kurosawa, R. and Proga, D. (2009a). On the large-scale outflows in active galactic nuclei: consequences of coupling the mass supply rate and accretion luminosity. *MNRAS*, 397:1791–1803.

Kurosawa, R. and Proga, D. (2009b). Three-Dimensional Simulations of Dynamics of Accretion Flows Irradiated by a Quasar. *ApJ*, 693:1929–1945.

Kurosawa, R., Proga, D., and Nagamine, K. (2009). On the Feedback Efficiency of Active Galactic Nuclei. *ApJ*, 707:823–832.

Li, Y. (2011). Accretion onto Intermediate-mass Seed Black Holes in Primordial Galaxies. *ArXiv e-prints*.

Luo, B., Brandt, W. N., Xue, Y. Q., Alexander, D. M., Brusa, M., Bauer, F. E., Comastri, A., Fabian, A. C., Gilli, R., Lehmer, B. D., Rafferty, D. A., Schneider, D. P., and Vignali, C. (2011). Revealing a Population of Heavily Obscured Active Galactic Nuclei at z   0.5-1 in the Chandra Deep Field-South. *ApJ*, 740:37–+.

Lusso, E. and Ciotti, L. (2011). One-zone models for spheroidal galaxies with a central supermassive black-hole. Self-regulated Bondi accretion. *A&A*, 525:A115.

Mack, K. J., Ostriker, J. P., and Ricotti, M. (2007). Growth of Structure Seeded by Primordial Black Holes. *ApJ*, 665:1277–1287.

Madau, P. and Rees, M. J. (2001). Massive Black Holes as Population III Remnants. *ApJ*, 551:L27–L30.

Madau, P., Rees, M. J., Volonteri, M., Haardt, F., and Oh, S. P. (2004). Early Reionization by Miniquasars. *ApJ*, 604:484–494.

Mayer, L., Kazantzidis, S., Escala, A., and Callegari, S. (2010). Direct formation of supermassive black holes via multi-scale gas inflows in galaxy mergers. *Nature*, 466:1082–1084.

Miller, M. C. and Colbert, E. J. M. (2004). Intermediate-Mass Black Holes. *International Journal of Modern Physics D*, 13:1–64.

Milosavljević, M., Bromm, V., Couch, S. M., and Oh, S. P. (2009a). Accretion onto ”Seed” Black Holes in the First Galaxies. *ApJ*, 698:766–780.

Milosavljević, M., Couch, S. M., and Bromm, V. (2009b). Accretion Onto Intermediate-Mass Black Holes in Dense Protogalactic Clouds. *ApJ*, 696:L146–L149.

Novak, G. S., Ostriker, J. P., and Ciotti, L. (2011). Feedback from Central Black Holes in Elliptical Galaxies: Two-dimensional Models Compared to One-

dimensional Models. *ApJ*, 737:26–+.

Oh, S. P. and Haiman, Z. (2002). Second-Generation Objects in the Universe: Radiative Cooling and Collapse of Halos with Virial Temperatures above 10^4 K. *ApJ*, 569:558–572.

Omukai, K., Schneider, R., and Haiman, Z. (2008). Can Supermassive Black Holes Form in Metal-enriched High-Redshift Protogalaxies? *ApJ*, 686:801–814.

Ostriker, J. P., Choi, E., Ciotti, L., Novak, G. S., and Proga, D. (2010). Momentum Driving: Which Physical Processes Dominate Active Galactic Nucleus Feedback? *ApJ*, 722:642–652.

Ostriker, J. P., Weaver, R., Yahil, A., and McCray, R. (1976). A new luminosity limit for spherical accretion onto compact X-ray sources. *ApJ*, 208:L61–L65.

Park, K. and Ricotti, M. (2011). Accretion onto Intermediate-mass Black Holes Regulated by Radiative Feedback. I. Parametric Study for Spherically Symmetric Accretion. *ApJ*, 739:2–+.

Park, K. and Ricotti, M. (2012). Radiation-Regulated Accretion onto Black Holes in Motion. III. Bondi-Hoyle-Lyttleton Accretion with Radiative Feedback (in preparation).

Park, M. and Ostriker, J. P. (2001). Preheated Advection-dominated Accretion Flow. *ApJ*, 549:100–117.

Pelupessy, F. I., Di Matteo, T., and Ciardi, B. (2007). How Rapidly Do Supermassive Black Hole "Seeds" Grow at Early Times? *ApJ*, 665:107–119.

Proga, D. (2007). Dynamics of Accretion Flows Irradiated by a Quasar. *ApJ*, 661:693–702.

Proga, D., Ostriker, J. P., and Kurosawa, R. (2008). Dynamics of Rotating Accretion Flows Irradiated by a Quasar. *ApJ*, 676:101–112.

Regan, J. A. and Haehnelt, M. G. (2009). Pathways to massive black holes and

compact star clusters in pre-galactic dark matter haloes with virial temperatures > 10000 K. *MNRAS*, 396:343–353.

Ricotti, M. (2007). Bondi Accretion in the Early Universe. *ApJ*, 662:53–61.

Ricotti, M. (2009). Late gas accretion on to primordial minihaloes: a model for Leo T, dark galaxies and extragalactic high-velocity clouds. *MNRAS*, 392:L45–L49.

Ricotti, M., Gnedin, N. Y., and Shull, J. M. (2001). Feedback from Galaxy Formation: Production and Photodissociation of Primordial H_2. *ApJ*, 560:580–591.

Ricotti, M., Gnedin, N. Y., and Shull, J. M. (2002a). The Fate of the First Galaxies. I. Self-consistent Cosmological Simulations with Radiative Transfer. *ApJ*, 575:33–48.

Ricotti, M., Gnedin, N. Y., and Shull, J. M. (2002b). The Fate of the First Galaxies. II. Effects of Radiative Feedback. *ApJ*, 575:49–67.

Ricotti, M. and Ostriker, J. P. (2004). Reionization, chemical enrichment and seed black holes from the first stars: is Population III important? *MNRAS*, 350:539–551.

Ricotti, M., Ostriker, J. P., and Gnedin, N. Y. (2005). X-ray pre-ionization powered by accretion on the first black holes - II. Cosmological simulations and observational signatures. *MNRAS*, 357:207–219.

Ricotti, M., Ostriker, J. P., and Mack, K. J. (2008). Effect of Primordial Black Holes on the Cosmic Microwave Background and Cosmological Parameter Estimates. *ApJ*, 680:829–845.

Sazonov, S. Y., Ostriker, J. P., Ciotti, L., and Sunyaev, R. A. (2005). Radiative feedback from quasars and the growth of massive black holes in stellar spheroids. *MNRAS*, 358:168–180.

Schneider, R., Ferrara, A., Natarajan, P., and Omukai, K. (2002). First Stars, Very Massive Black Holes, and Metals. *ApJ*, 571:30–39.

Shakura, N. I. and Sunyaev, R. A. (1973). Black holes in binary systems. Observational appearance. *A&A*, 24:337–355.

Shapiro, P. R. and Kang, H. (1987). Hydrogen molecules and the radiative cooling of pregalactic shocks. *ApJ*, 318:32–65.

Shapiro, S. L. (1973). Accretion onto Black Holes: the Emergent Radiation Spectrum. *ApJ*, 180:531–546.

Sharma, P., Quataert, E., Hammett, G. W., and Stone, J. M. (2007). Electron Heating in Hot Accretion Flows. *ApJ*, 667:714–723.

Steidel, C. C., Hunt, M. P., Shapley, A. E., Adelberger, K. L., Pettini, M., Dickinson, M., and Giavalisco, M. (2002). The Population of Faint Optically Selected Active Galactic Nuclei at z ~ 3. *ApJ*, 576:653–659.

Stone, J. M. and Norman, M. L. (1992). ZEUS-2D: A radiation magnetohydrodynamics code for astrophysical flows in two space dimensions. I - The hydrodynamic algorithms and tests. *ApJS*, 80:753–790.

Strohmayer, T. E. and Mushotzky, R. F. (2009). Evidence for an Intermediate-mass Black Hole in NGC 5408 X-1. *ApJ*, 703:1386–1393.

van der Marel, R. P. (2004). Intermediate-mass Black Holes in the Universe: A Review of Formation Theories and Observational Constraints. *Coevolution of Black Holes and Galaxies*, pages 37–+.

Venkatesan, A., Giroux, M. L., and Shull, J. M. (2001). Heating and Ionization of the Intergalactic Medium by an Early X-Ray Background. *ApJ*, 563:1–8.

Vitello, P. (1984). Optically thick, time-dependent spherical accretion onto a black hole. I - Equations and numerical methods. *ApJ*, 284:394–406.

Volonteri, M., Haardt, F., and Madau, P. (2003). The Assembly and Merging History of Supermassive Black Holes in Hierarchical Models of Galaxy Formation. *ApJ*, 582:559–573.

Volonteri, M., Lodato, G., and Natarajan, P. (2008). The evolution of massive black hole seeds. *MNRAS*, 383:1079–1088.

Volonteri, M. and Rees, M. J. (2005). Rapid Growth of High-Redshift Black Holes. *ApJ*, 633:624–629.

Wandel, A., Yahil, A., and Milgrom, M. (1984). Nonadiabatic self-consistent spherical accretion as a model for quasars and active galactic nuclei. *ApJ*, 282:53–60.

Whalen, D. and Norman, M. L. (2008a). Ionization Front Instabilities in Primordial H II Regions. *ApJ*, 673:664–675.

Whalen, D. J. and Norman, M. L. (2008b). Three-Dimensional Dynamical Instabilities in Galactic Ionization Fronts. *ApJ*, 672:287–297.

Whalen, D. J. and Norman, M. L. (2011). Radiation hydrodynamical instabilities in cosmological and galactic ionization fronts. *Ap&SS*, 336:169–174.

Wheeler, J. C. and Johnson, V. (2011). Stellar-mass Black Holes in Young Galaxies. *ApJ*, 738:163.

Yoo, J. and Miralda-Escudé, J. (2004). Formation of the Black Holes in the Highest Redshift Quasars. *ApJ*, 614:L25–L28.